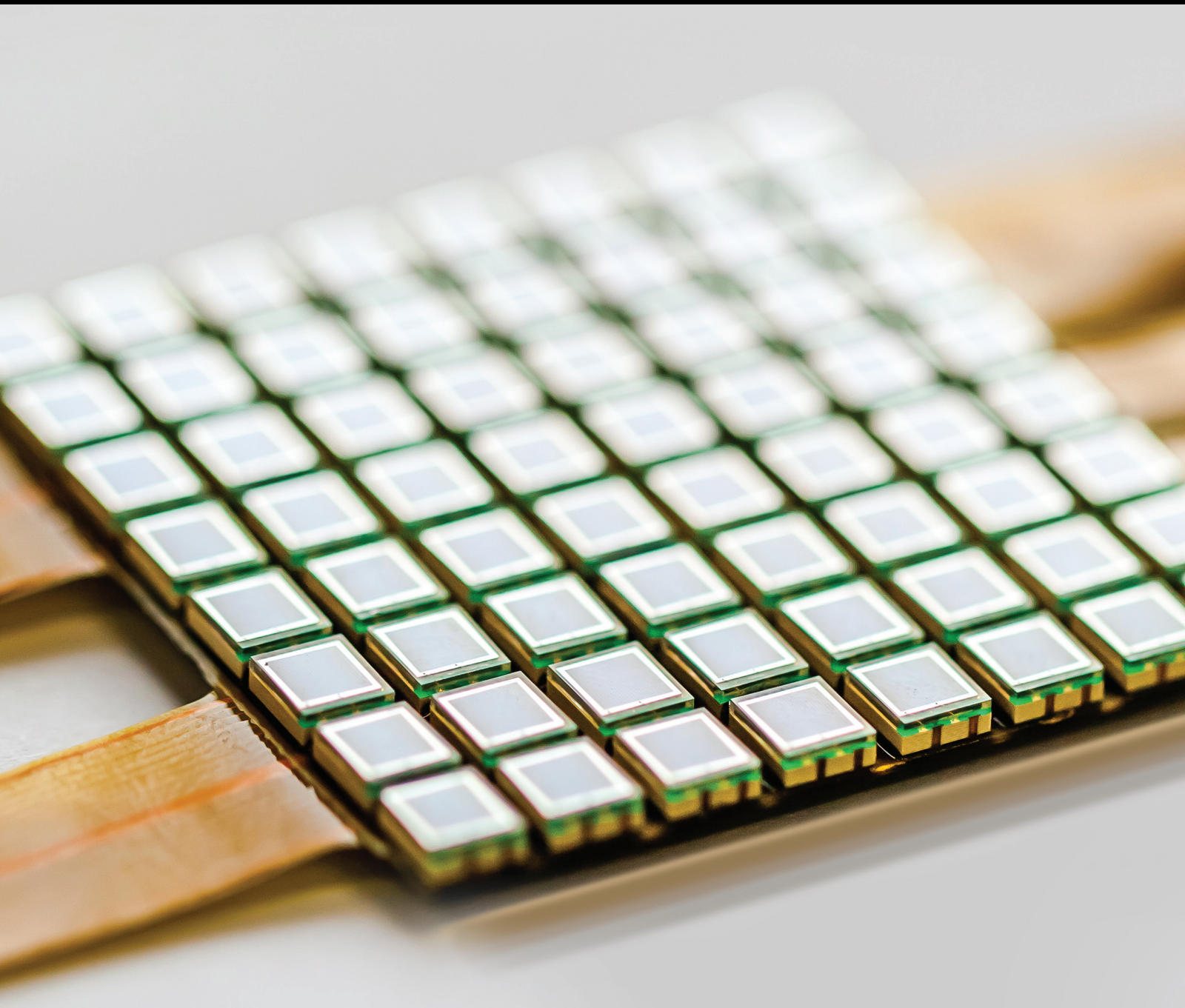# Flexible and/or Stretchable Sensor Systems

Lead Guest Editor: Aftab M. Hussain
Guest Editors: Mohamed T. Ghoneim, Jhonathan P. Rojas, and Hossain Fahad

Flexible and/or Stretchable Sensor Systems

Flexible and/or Stretchable Sensor Systems

Lead Guest Editor: Aftab M. Hussain
Guest Editors: Mohamed T. Ghoneim, Jhonathan P. Rojas, and Hossain Fahad

Editorial Board

Contents

Editorial
Flexible and/or Stretchable Sensor Systems

Aftab M. Hussain [iD],[1] **Mohamed T. Ghoneim** [iD],[2] **Jhonathan P. Rojas**,[3] and **Hossain Fahad**[4]

[1]*International Institute of Information Technology (IIIT), Center for VLSI and Embedded Systems Technology (CVEST), Hyderabad, India*
[2]*Massachusetts Institute of Technology (MIT) Media Lab, Cambridge, MA, USA*
[3]*King Fahd University of Petroleum and Minerals (KFUPM), Dhahran, Saudi Arabia*
[4]*University of California, Berkeley, CA, USA*

Correspondence should be addressed to Aftab M. Hussain; aftab.hussain@iiit.ac.in

With recent advancements in the field of wearable devices based on Internet of Things (IoT), the concept of flexible and stretchable electronic systems has become increasingly significant. Although decades of dimensional scaling have led to the miniaturization of the traditional complementary metal oxide semiconductor- (CMOS-) based electronic components, they still remain mechanically rigid and brittle. These rigid devices can be mounted on flexible PCB substrates to obtain a certain degree of flexibility; however, this technique cannot lead to truly body conformal electronic systems. Thus, research teams around the world have been looking at various ways of obtaining completely flexible electronic components at the device level itself. These efforts include various processes to thin down silicon chips to make them flexible or development and use of flexible and stretchable substrate materials to fabricate electronic devices.

The thinning down process for traditional silicon-based electronic chips can be performed before or after the complete transistor fabrication process [1]. These approaches are referred to as "device first" approach or "device last" approach. In case of the device last approach, thin films of single crystal silicon are transfer printed to a flexible substrate and processed further to fabricate CMOS circuitry [2, 3]. However, in this approach, many high-temperature steps have to be avoided due to the limited thermal stability of the flexible substrate, leading to a suboptimal circuit. In case of the device first approach, the circuits are made on the silicon substrate using state-of-the-art CMOS processes as

usual. After completion of the process, some additional process steps are employed to thin down the silicon chip to make it flexible. These include the controlled spalling process [4, 5], the trench-protect-etch-release (TPER) process [6, 7], and the soft-etch-back (SEB) process [8, 9].

Complementing the efforts to fabricate conformal silicon chips, efforts have been made to make other components of an electronic system flexible and stretchable. These include the use of novel processes to fabricate flexible and stretchable sensor systems [10, 11], actuator systems [12, 13], communication systems [14, 15], memory modules [16, 17], and batteries [18–20]. Having flexible and stretchable versions of these systems is particularly important because body conformal end gadgets generally have applications in the IoT segment where sensing, actuation, storage, and communication are key processes. The impact of successful fabrication of conformal systems ranges from advanced healthcare and wearable diagnostics to military and aerospace applications. Indeed, several key challenges such as material selection, scalable fabrication, reliability, and cost need to be solved to ascertain ubiquitous adoption of such systems.

The call for papers for this special issue focused on publishing high-quality, high-impact, and original research articles and review articles focusing on flexible and stretchable sensor devices, sensor drive circuitry, and overall systems. In response to the call, papers were submitted from research teams across the world. These papers were reviewed for novelty and quality of research. Because of the complexity of

real-life deployment of flexible and stretchable systems, special attention was given to the papers including experimental data and field data. After a rigorous peer-review process, 4 papers were accepted for publication in this special issue.

The paper by G. Prats-Boluda et al. presents a wearable textile ECG sensor electrode. Two sizes of textile concentric ring electrodes (TCREs) are fabricated and tested for monitoring cardiac activity. The electrodes are fabricated using multilayer thick film serigraphic technology. The devices are found to be low-cost and easy to implement, while having the advantages of textiles for being lightweight, stretchable, adjustable, washable, and long-lasting.

The paper by H. Nakamoto et al. presents a wearable lumbar-motion monitoring device using stretchable strain sensors. The strain sensors are fabricated using urethane elastomer and carbon nanotube membranes. Six of these strain sensors form a parallel-sensor mechanism that measures rotation angles of lumbar motion in three axes. The parallel-sensor mechanism calculates rotation angles from the lengths of the strain sensors iteratively.

The paper by M. Li et al. presents an underwater wireless sensor network (UWSN) routing algorithm based on simplified harmony search (SHS).

The paper by Y. C. Manie et al. presents a Fiber Bragg Grating (FBG) sensor using intensity and wavelength division multiplexing (IWDM), Raman amplifier, and extreme learning machine (ELM).

Conflicts of Interest

The editors declare that they have no conflicts of interest regarding the publication of this special issue.

Aftab M. Hussain
Mohamed T. Ghoneim
Jhonathan P. Rojas
Hossain Fahad

References

[1] A. M. Hussain and M. M. Hussain, "CMOS-technology-enabled flexible and stretchable electronics for internet of everything applications," *Advanced Materials*, vol. 28, no. 22, pp. 4219–4249, 2016.

[2] J.-H. Ahn, H. S. Kim, E. Menard et al., "Bendable integrated circuits on plastic substrates by use of printed ribbons of single-crystalline silicon," *Applied Physics Letters*, vol. 90, no. 21, article 213501, 2007.

[3] E. Menard, K. J. Lee, D.-Y. Khang, R. G. Nuzzo, and J. A. Rogers, "A printable form of silicon for high performance thin film transistors on plastic substrates," *Applied Physics Letters*, vol. 84, no. 26, pp. 5398–5400, 2004.

[4] F. Dross, J. Robbelein, B. Vandevelde et al., "Stress-induced large-area lift-off of crystalline Si films," *Applied Physics A*, vol. 89, no. 1, pp. 149–152, 2007.

[5] Y. Kwon, C. Yang, S.-H. Yoon, H.-D. Um, J.-H. Lee, and B. Yoo, "Spalling of a thin Si layer by electrodeposit-assisted stripping," *Applied Physics Express*, vol. 6, no. 11, 2013.

[6] G. T. Sevilla, J. P. Rojas, S. Ahmed, A. Hussain, S. B. Inayat, and M. M. Hussain, "Silicon fabric for multi-functional applications," in *2013 Transducers & Eurosensors XXVII: The 17th International Conference on Solid-State Sensors, Actuators and Microsystems (TRANSDUCERS & EUROSENSORS XXVII)*, pp. 2636–2639, Barcelona, Spain, 2013.

[7] J. P. Rojas, G. A. Torres Sevilla, M. T. Ghoneim et al., "Transformational silicon electronics," *ACS Nano*, vol. 8, no. 2, pp. 1468–1474, 2014.

[8] G. A. Torres Sevilla, M. T. Ghoneim, H. Fahad, J. P. Rojas, A. M. Hussain, and M. M. Hussain, "Flexible nanoscale high-performance FinFETs," *ACS Nano*, vol. 8, no. 10, pp. 9850–9856, 2014.

[9] G. A. Torres Sevilla, A. S. Almuslem, A. Gumus, A. M. Hussain, M. E. Cruz, and M. M. Hussain, "High performance high-κ/metal gate complementary metal oxide semiconductor circuit element on flexible silicon," *Applied Physics Letters*, vol. 108, no. 9, 2016.

[10] J. M. Nassar, M. D. Cordero, A. T. Kutbee et al., "Paper skin multisensory platform for simultaneous environmental monitoring," *Advanced Materials Technologies*, vol. 1, no. 1, 2016.

[11] A. M. Hussain and M. M. Hussain, "Deterministic integration of out-of-plane sensor arrays for flexible electronic applications," *Small*, vol. 12, no. 37, pp. 5141–5145, 2016.

[12] A. M. Hussain, E. B. Lizardo, G. A. Torres Sevilla, J. M. Nassar, and M. M. Hussain, "Ultrastretchable and flexible copper interconnect-based smart patch for adaptive thermotherapy," *Advanced Healthcare Materials*, vol. 4, no. 5, pp. 665–673, 2015.

[13] H. Zhao, A. M. Hussain, M. Duduta, D. M. Vogt, R. J. Wood, and D. R. Clarke, "Compact dielectric elastomer linear actuators," *Advanced Functional Materials*, vol. 28, no. 42, 2018.

[14] A. M. Hussain, F. A. Ghaffar, S. I. Park, J. A. Rogers, A. Shamim, and M. M. Hussain, "Metal/polymer based stretchable antenna for constant frequency far-field communication in wearable electronics," *Advanced Functional Materials*, vol. 25, no. 42, pp. 6565–6575, 2015.

[15] S. Hong, S. H. Kang, Y. Kim, and C. W. Jung, "Transparent and flexible antenna for wearable glasses applications," *IEEE Transactions on Antennas and Propagation*, vol. 64, no. 7, pp. 2797–2804, 2016.

[16] M. T. Ghoneim, M. A. Zidan, M. Y. Alnassar et al., "Thin PZT-based ferroelectric capacitors on flexible silicon for nonvolatile memory applications," *Advanced Electronic Materials*, vol. 1, no. 6, 2015.

[17] M. T. Ghoneim and M. M. Hussain, "Study of harsh environment operation of flexible ferroelectric memory integrated with PZT and silicon fabric," *Applied Physics Letters*, vol. 107, no. 5, 2015.

[18] A. T. Kutbee, R. R. Bahabry, K. O. Alamoudi et al., "Flexible and biocompatible high-performance solid-state micro-battery for implantable orthodontic system," *npj Flexible Electronics*, vol. 1, p. 7, 2017.

[19] D. Singh, A. T. Kutbee, M. T. Ghoneim, A. M. Hussain, and M. M. Hussain, "Strain-induced rolled thin films for lightweight tubular thermoelectric generators," *Advanced Materials Technologies*, vol. 3, 2018.

[20] S. Xu, Y. Zhang, J. Cho et al., "Stretchable batteries with self-similar serpentine interconnects and integrated wireless recharging systems," *Nature Communications*, vol. 4, article 1543, 2013.

Research Article

RSHSC-Routing Algorithm Based on Simplified Harmony Search and Coding for UWSNs

Meiju Li,[1,2,3] **Xiujuan Du** [1,2] **and Chunyan Peng** [1,2]

[1]*Computer Department, Qinghai Normal University, Xining 810008, China*
[2]*Key Laboratory of the Internet of Things of Qinghai Province, Xining 810008, China*
[3]*College of Physics and Electronic Information Engineering, Qinghai Nationalities University, Xining 810007, China*

Correspondence should be addressed to Xiujuan Du; 124111397@qq.com

With the development of wireless networks and increasingly interest of people in underwater resources and environment, UWSNs are being paid more and more attention. Because of the characteristics of underwater channel and acoustic signal, the protocols used in the terrestrial networks cannot be directly used in UWSNs. In this paper, a reliable and energy-efficient routing protocol based on SHS and coding, called RSHSC, is proposed. Firstly, regular nodes are assigned to cluster heads according to simplified harmony search algorithm. Secondly, partial network encoding is introduced and the next two-hop information is considered when data packets are transmitted to sink nodes from the source node. Only the best next-hop forwards data packets. All data packets from neighbor nodes are used for decoding. Thirdly, two schemes of updating routing are designed and compared. Lastly, extensive simulations prove RSHSC is effective in improving reliability and decreasing energy consumption.

1. Introduction

In recent years, UWSNs (underwater wireless sensor networks) attracted more and more attentions because of the wide application such as marine source exploration and pollution monitor [1–3]. Like other wireless networks, it is necessary to improve the communication performance for UWSNs. However, UWSN is different from other wireless networks. UWSN has some characteristics that other wireless networks have not. Firstly, UWSN is provided energy by batteries. Once the battery is exhausted, the node is considered as dead [4]. Meanwhile, the acoustic communication consumes more energy than radio signal and optical signal. Secondly, underwater channel is complex because of shipping, marine organisms, and so on [5]. Besides, the communication quality is affected by multipath resulting from the reflections, water salinity, temperature, and so on [6]. Thirdly, mobile topology [7]. The position of the node is forced to change with the water currents and marine biological activities [8]. Fourthly, the propagation delay is longer than terrestrial networks. The propagation speed of acoustic signal under water is just 1500 m/s, which is five magnitude lower than radio signal on land (3×10^8 m/s) [9]. Because of those factors of UWSNs, the protocols used on the land cannot be directly applied in UWSNs, especially for routing protocols. Therefore, designing a routing protocol special for UWSNs is necessary [10–12].

Like most wireless networks, the performances of delay, energy consumption, reliability, and throughput and bandwidth utilization are important in UWSNs [13]. In recent years, more and more routing protocols are proposed. Some of them are to decrease energy consumption, some of them are to shorten delay. They are effective in certain scenarios but cannot take into account multiple performance.

The contributions of this paper are showed as follows:

(1) The regular nodes are assigned to the cluster heads based on simplified harmony search algorithm (SHS). Two schemes are designed

(2) Partial network coding is introduced when routing data from source cluster head to the sink node. Meanwhile, the data from all neighbor nodes are used

for decoding, which makes full use of the broadcast characteristics of UWSNs

(3) Two schemes are compared for maintaining routing timely: when the speed of water flow is constant, scheme 1 is adopted; otherwise, the scheme 2 is used

(4) Through simulations, the best SHS and routing maintaining algorithm are determined and the performance of RSHSC is evaluated

2. Relative Works

Researchers have designed some routing protocols for UWSNs in recent years. In 2008, Yan et al. proposed DBR routing algorithm [14]. In DBR, neighbors with less depth need to wait a certain time to forward data packets. The lengths of waiting time of neighbors are set according to the depth. The more depth, the shorter waiting time. The neighbor will cease to forward if hearing the same data packets during waiting time. DBR has some defects. Therefore, some improved protocols are provided. Residual energy is introduced to select next-hop in EEDBR [15]. DBR-NC uses the coding technique [16]. To avoid selecting next-hop in the void area, next-hop of the next-hop is considered in WDFAD-DBR [17]. Meanwhile, the forwarding area is adjusted according to node dense. LMPC is proposed in [18]. In LMPC, a data packet is delivered along multiple paths according to binary tree. FLMPC improved LMPC in [19]. Nodes are classified into cross nodes and regular nodes. Only the cross nodes generate binary tree. Hao et al. proposed GPNC algorithm [20]. Data packets are forwarded to sink greedily using the sensor nodes' location information. GPNC incorporates partial network coding. In L2-ABF, the sender selects next-hop by calculating the forwarding angle. CoUWSN uses cost function of distance and SNR of the link to decide the next-hop [21]. Sink mobility pattern is given in DEADs [22]. AEDG is proposed in [23]. In AEDG, AUV is used to collect data. To prevent gateway overloading, the number of associated node with the gateway node is limited. The residual energy and number of neighbors are considered. Hubcode is proposed in [24]. Hubcode is an algorithm based on cluster. Hubcode exchanges coefficient matrix and gets initial data via calculating inverse matrix. In BLOAD [25], the weight of nodes is calculated according to the distance among nodes, the more overlap area in the coverage range of the node, the less importance for the node. In TSBNC, the coding is introduced into the time-slot algorithm [26]. Network coding and cross-layer are used in NCRP [27]. The node with the least weight is selected as the cluster head. In QDAR [28], end-to-end delay and residual energy are introduced into the Q-Learning algorithm. In LB-AGR, the best next-hop is determined based on density, available energy, location, and level difference between neighbor nodes [29]. The characteristics of these protocols are showed as Table 1.

3. Model Analysis

In this sector, network model, energy and propagation model are analyzed.

3.1. Network Model. The network model is showed in Figure 1. In our network, nodes are deployed in the 3D underwater environment and divided into three types: regular nodes, advanced nodes, and sink nodes. The first two nodes are defined as follows:

(i) Regular nodes: the nodes have ordinary amount of initial energy, which can communicate with advanced nodes and sink nodes

(ii) Advanced nodes: the nodes have more initial energy than regular nodes. Advanced nodes can communicate with each other, regular nodes and sink nodes. The advanced node is also called as the cluster head (CH). The advanced nodes with almost depth are divided into the same levels

In the network, each sink node is equipped with both acoustic modem and RF modem, which are responsible for communicating with underwater nodes (regular nodes and advanced nodes) and data centers, respectively. Each underwater node is equipped with an acoustic modem, which is responsible for communicating with each other and sink nodes. All nodes mobile with water flow. Each node can get the location information of itself.

3.2. Channel Model. To design a routing algorithm with high bandwidth utilization, energy efficient and reliable for UWSNs, we must learn about the channel model. In UWSNs, channel is affected by absorption loss and spreading loss. The attenuation $A(d, f)$ is showed as (1) [21].

$$A(d, f) = A_0 d^k \alpha(f)^d. \tag{1}$$

Here, k is the spreading factor, and the value is 1.5 for practical applications. d is the spreading distance. A_0 is a normalization constant. $\alpha(f)$ is presented as (2).

$$10 \log \alpha(f) = \frac{0.11f^2}{1 + f^2} + \frac{44f^2}{4100 + f^2} + \frac{2.75f^2}{10^4} + 0.003 [\text{dB/km}]. \tag{2}$$

There are great many types of noise under water. The main noise include turbulence (N_t), shipping (N_s), waves (N_w), and thermal noise (N_{th}). These noises can be modeled by the power spectral and Gaussian statistics as (3), (4), (5), (6), and (7) [22].

$$N(f) = N_t(f) + N_s(f) + N_w(f) + N_{th}(f), \tag{3}$$

$$10 \log N_t(f) = 17 - 30 \log f, \tag{4}$$

$$10 \log N_s(f) = 40 + 20(s - 0.5) + 26 \log f - 60 \log (f + 0.03), \tag{5}$$

$$10 \log N_w(f) = 50 + 7.5\sqrt{w} + 20 \log f - 40 \log (f + 0.4), \tag{6}$$

$$10 \log N_{th}(f) = -15 + 20 \log f. \tag{7}$$

TABLE 1: Protocols characteristics.

Protocol name	Characteristics	Advantage	Disadvantage
DBR	Select next-hop only based on depth	Independent location information, decrease part of redundant forwarding	Long delay, high energy consumption
EEDBR	Residual energy is considered	Prolong network life	Long delay, redundant forwarding
DBR-NC	Coding is introduced	Reliable	Long delay, energy is not considered
WDFAD-DBR	Next two-hop information is considered. Adaptively adjust the forwarding area according to node dense	Avoid selecting the node in the void area as the next-hop	Long delay in sparse network delivery ratio is low
iAMCTD	Courier node is used	Courier node decreases delay, optimized threshold decreases redundant forwarding	Energy unbalance
LMPC	Establish binary tree	Reliable, high delivery ratio	High energy consumption, void node is not considered
FLMPC	Establish binary tree from the sensor nodes which reside near the layer	Copies in the cross node increase the delivery ratio, decrease the retransmission	Routing update is not considered, multiple routing wastes energy
GPNC	Network coding is used based on geographic location information	Reliable, decrease energy consumption, shorten delay	Void node is not considered, energy unbalance
CoUWSN	Uses multiple input multiple output	Save transmit power, increase data rate, extend the communication range	Consume more energy, long delay
DEADs	Cooperative routing is joined with sink mobility	High throughput, prolong network life	Waste energy, energy unbalance
AEDG	Use shortest path tree to assign nodes to gate way	Network lifetime prolongation, throughput maximization	Long delay
Hubcode	Use hubs as relay and encode multiple messages address to the same destination	Reducing the forwarding overheads, increasing the delivery ratio	Energy balance long delay
BLOAD	Addressing energy hole, mixed routing scheme (including directly and multiple hop communication) is used	Balance energy, avoid energy hole	The node with longer distance to sink dies quickly
TSBNC	Theory of network coding is introduced into time-slot based routing algorithm	Decrease energy consumption and collisions	Energy unbalance, long delay
NCRP	Network coding and cross-layer design are used	High delivery ratio, save energy	Void node is not considered, energy unbalance
QDAR	Q-learning algorithm is introduced	Extending network lifetime and short delay	In the mobile network, energy consumption is high. Link quality is not considered
LB-AGR	Nodes are divided into different levels, upstream and downstream are considered when selecting the best-next-hop	Comprehensive factors are considered	The void node is not considered, greedy routing

Here, s is the shipping factor (varies from 0 to 1), W is the wind velocity (varies from 0 to 10 m/s), and f denotes the carrier frequency.

Therefore, the signal to noise (SNR) is showed as (8), which is related to the propagation distance (d) and the carrier frequency (f). B is the bandwidth.

$$\text{SNR}(d, f) = \frac{P}{A(d, f)N(f)B}. \tag{8}$$

According to Shannon theory, channel capacity is calculated as (9) [21].

$$C(d, f) = B\log_2(1 + \text{SNR}(d, f)). \tag{9}$$

4. Protocol Design

The implementation of RSHSC consists of four steps: initialization, cluster construction, intercluster routing, and routing
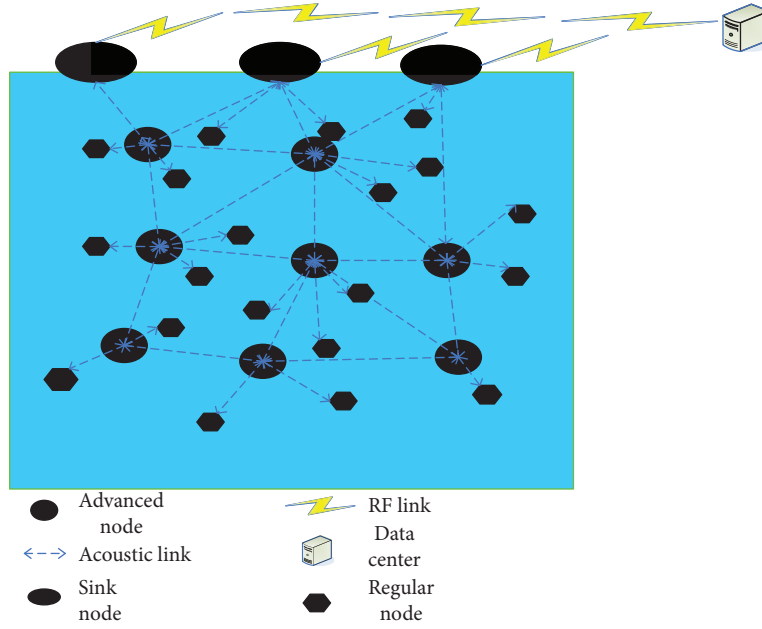
FIGURE 1: Network model.

TABLE 2: Format of hello packet.

ID	Seq number	ID1	ID2	ID3	Reserve	RE_ENERGY	Address

maintaining. In initialization phase, sink nodes broadcast beacon signal with the location information of themselves to underwater nodes. Cluster heads broadcast hello packets. Regular nodes broadcast information packets. The details of initialization phase are showed in Section 4.1. In cluster construction phase, regular nodes are assigned to the cluster head based on SHS algorithm, which is detailed in Section 4.2. In the interclusters routing phase, the cluster head encodes original packets and selects the best next-hop according to the information of neighbors and next two hop, which is detailed in Section 4.3. Because nodes mobile with the water flow, the routing needs to be updated timely. In routing maintaining phase, two algorithms are provided to decrease the energy consumption and collision results from sending too many nondata packets, which is detailed in Section 5.

4.1. Initialization.
Sink nodes broadcast beacon signal including location and ID of themselves. After receiving beacon signal, each cluster head calculates and saves the distance between itself and sink nodes. Then, the cluster head broadcasts hello packet, whose format is showed in Table 2. "ID" is the source node ID of the hello packet. Seq number is the sequence number of the hello packet. "ID1," "ID2," and "ID3" are the ID of member nodes. Initially, the field of "ID1", "ID2," and "ID3" are filled with "0." Address is the location information of the cluster head. "RE_ENERGY" is the residual energy of the cluster head. The regular node sends information packets after receiving a hello packet. The format of information packet is showed in Table 3. "ID1" is the ID number of the cluster head with the highest priority that the regular node joins in. "Distance 1" is the

TABLE 3: Format of information packet.

ID	ID1	Distance1	ID2	Distance 2

distance to the cluster head with ID1. "ID2" and "Distance 2" are as the ID1 and Distance1. Before receiving less than three information packets from different regular nodes, the corresponding ID is filled with "0." Analogously, the ID2 and Distance2 are filled with "0" when receiving hello packets with only ID address.

In this phase, on one hand, regular nodes and cluster heads get information from each other; on the other hand, cluster heads get the information of neighbor cluster heads.

4.2. Cluster Constructing.
In the process of cluster constructing, the harmony search algorithm is introduced.

4.2.1. Harmony Search (HS) Algorithm.
HS is a heuristic global search algorithm. The I instruments ($I = 1, 2, \ldots, m$) are analogous as the I variables to solve optimization problems, and the harmonic R_j of each musical instrument tone ($j = 1, 2, \ldots, m$) is equivalent to the j solution vectors of the optimization problem, and the evolution is analogous to the objective function.

The procedure of HS is as follows:

(1) The algorithm generates m initial solutions into the harmony memory (HM) and searches for new solutions in HM with a probability HR
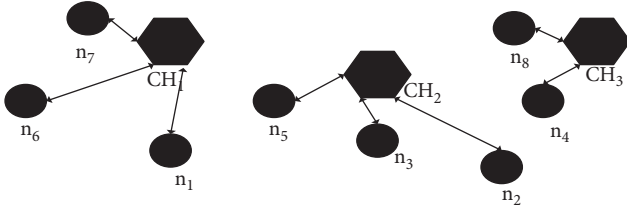
Figure 2: Regular node assignment.

(2) The algorithm generates local perturbations to the new solution with probability P_r. If the new solution objective function value is better than the worst solution in HM, replace it

(3) Iterate iteratively until the expected number of iterations is $T_{\max}$

(4) As above, by introducing HR and P_r, HS algorithm is expected to the balance of exploration ability of the solution space, but there is no the recital basis for how to choose the value

4.2.2. Simplified HS. According to the characteristics of UWSNs, the average number of regular nodes managed by each cluster head is small, and it is difficult to get the global information of the whole networks. Therefore, the simplified HS algorithm is proposed for UWSNs.

(A) Taking regular nodes as research objects, the assignment is determined by regular nodes. We simplify the HS (HSA) as follows:

(1) The objective function is

$$F_1 = \alpha \sum_{i=1}^{\tilde{CH}_i} \frac{|d_{n_i - CH_i}|}{R} + \beta \sum_{i=1}^{i=N} \frac{|\tilde{CH}_i - \bar{N}|}{\bar{N}}. \quad (10)$$

Here, $\alpha + \beta = 1$. $|d_{n_i - CH_i}|$ presents the distance between the regular node n_i and the cluster head CH_i. $\tilde{CH}_i$ presents the number of members for cluster head CH_i. R is the communication radius. When $\tilde{CH}_i$ is constant, the less F_1, the better assignment. The first part reflects the balance among regular nodes, and the second part reflects the balance among cluster heads.

(2) Because any regular node is assigned to only the cluster head in its communication range, we use the local selection of regular nodes being assigned to the cluster head to replace the global assignment. So the $X_i = (x_{i,1}, x_{i,2} \ldots x_{i,k} \ldots x_{i,n})$. n is the number of member nodes of cluster heads CH_i and adjacent to CH_i. X_i is the HM, $x_{i,k}$ is the ID of the cluster head the regular node n_i joining in. For example, in Figure 2, the regular nodes are $R = (n_1, n_2, n_3, n_5, n_6, n_7)$, $X_1 = (1, 2, 2, 2, 1, 1)$.

While $R = (n_1, n_2, n_3, n_4, n_5, n_6, n_7, n_8)$, $X_2 = (1, 2, 2, 2, 3, 2, 1, 1, 3)$

(3) According to the information of cluster heads recorded in the regular nodes, the HM is adjusted at probability P. P is calculated by (11). Here, $p_i' = 1/d_i$, $p' = \sum_{i=1}^{i=n_i^{\cdot}} (1/d_1 (1/d_1))$, $n_i^{\cdot}$ is the number of cluster head in the communication range of regular node n_i, d_i is the distance between the node n_i and the cluster head. If the adjusted objective function is bigger than the value before, replace it. Otherwise, the HM is kept

$$P = \frac{p_i'}{p'}. \quad (11)$$

(B) Taking cluster heads as research objects, the assignment is determined by cluster heads. We simplify the HS (HSB) as follows:

(1) The objective function is the same as HSA

(2) Similar to HSA, $X_i = (x_{i,1}, x_{i,2} \ldots x_{i,k} \ldots x_{i,n})$. $x_{i,k}$ is the aggregate of member nodes in the cluster head CH_i. As is showed in Figure 2, $R = (CH_1, CH_2, CH_3)$, then $X_i = (\{n_1, n_6, n_7\}, \{n_2, n_3, n_5,\}, \{n_3, n_4, n_8\})$

(3) According to the information of regular nodes recorded in the cluster heads, the HM is adjusted at probability P. P is calculated by (12), p_i^- is the probability each member n_i having only one cluster head, and p_i' is the probability n_i being adjusted into another cluster head. p_i' can be gotten from (13). R_i and R_j denote the residual energy of the cluster heads in a regular node communication range, $\tilde{CH}_i$ and $\tilde{CH}_j$ are the number of members in a cluster, respectively, $\gamma_1 + \gamma_2 = 1$

$$P = 1 - \prod_{i=1}^{i=\tilde{CH}_i} \left(1 - (1 - p_i^-)p_i'\right), \quad (12)$$

$$p_i' = \gamma_1 \frac{R_i}{R_i + R_j} + \gamma_2 \frac{1/\tilde{CH}_i}{\left(1/\tilde{CH}_i\right) + \left(1/\tilde{CH}_j\right)}. \quad (13)$$

4.3. Routing Construction. How are data packets transmitted from a source node to the sink node? In this section, the procedure is analyzed.

4.3.1. Review of Routing. According to the initialization procedure, each CH saves the information of neighbor CHs as showed in Table 4. After receiving a hello packet, the CH

TABLE 4: Neighbors' information table of cluster head.

ID	Address	Residual energy	Address of next-hop	Next-hop residual energy	Priority

FIGURE 3: Advanced distance.

firstly checks the "address" field and calculates the distance between the source node of hello packet and the sink node. Only the cluster head with shorter dist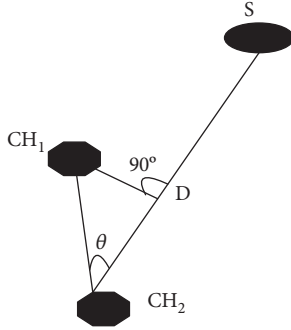ance to the sink node has opportunity to be the next-hop. The priority of neighbors is calculated by formula (14). $d(t)$ is the advanced distance to the sink node. As showed in Figure 3, CH_2 is the source cluster head, CH_1 is the neighbor of CH_2, S is the sink node. The $\overline{CH_2D}$ is the advanced distance to node S. We set the coordinate of CH_2, CH_1, and S is (x_0, y_0, z_0), (x_1, y_1, z_1), and $(0,0,0)$, respectively. From the coordinate, we can get $\overline{CH_2S} = \sqrt{x(t)_0^2 + y(t)_0^2 + z(t)_0^2}$, $\overline{CH_1S} = \sqrt{x(t)_1^2 + y(t)_1^2 + z(t)_1^2}$, $\overline{CH_2CH_1} = \sqrt{(x(t)_0 - x(t)_1)^2 + (y(t)_0 - y(t)_1)^2 + (z(t)_0 - z(t)_1)^2}$, $\cos \theta = \overline{CH_2CH_1}^2 + \overline{CH_2S}^2 - \overline{CH_1S}^2/2\overline{CH_2CH_1} \times \overline{CH_1S}$. So $d(t) = \overline{CH_2CH_1} \cos \theta$. The more $p(t)$, the higher priority. Only the neighbor cluster head with the highest priority forwards the data packet.

$$p(t) = k_1 \frac{E_R(t)}{E_I(t)} + k_2 \frac{d(t)}{R}. \tag{14}$$

As above, the node with bigger advanced distance to sink and more residual energy is selected as the best next-hop. Therefore, the selected next-hop may have far distance to the previous hop, which leads to the big probability of failing to deliver. To enhance the reliability of the network, in our algorithm, coding is introduced.

4.3.2. Network Coding. In most of conventional routing algorithms, the forwarder is responsible for relaying data without any processing. However, in UWSNs, like other wireless communications, broadcast is adopted. Meanwhile, the bandwidth is limited and delay is long. In order to make full use of the characteristics of broadcast and limited bandwidth, network coding is an efficient measure. The basic procedure of network coding is showed in Figure 4.

The data packet a is from node A. The data packet b is from node B. The node C is a relay.

In the network without coding as Figure 4(a), the necessary number of time slots to exchange data packets a and b is 4. While in Figure 4(b), the number is 3.

Furthermore, we compare the partial network coding with the full network coding. In Figure 5, the data packets d_1, d_2, and d_3 are sent from the node A to node B. Here, we make

$$[d] = \begin{matrix} d_1 \\ d_2 \\ d_3. \end{matrix} \tag{15}$$

Node A encode data packets $[d]$ into $[d']$.

$$\left[d' \right] = \begin{bmatrix} \gamma_{11} & \gamma_{12} & \gamma_{13} \\ \gamma_{21} & \gamma_{22} & \gamma_{23} \\ \gamma_{31} & \gamma_{32} & \gamma_{33} \end{bmatrix} [d]. \tag{16}$$

To decode the encoded packets into original data packets, node B needs all data packets. So, the delay to transmit these three data packets is 3T (T is one slot time). In Figure 5(b), the partial network coding is showed. Here, $d'_1 = \gamma_1 d_1$, $d'_2 = \gamma_2 d_1 + \gamma_3 d_2$, and $d'_3 = \gamma_4 d_1 + \gamma_5 d_2 + \gamma_6 d_3$. So, in the partial network coding, recovering d'_1, d'_2, and d'_3 into original packets needs T, 2T, and 3T, respectively. The average delay to transmit these three packets is $(T + 2T + 3T)/3 = 2T$. Comparing the partial network coding with full network coding, we can get the partial network coding is better than full network coding.

In our algorithm, partial network coding is adopted. Each relay receives the encoded packets and decodes them. Then the next-hop of relay continues to encode the original data packets until the sink node receives the packets. If the sink node is in the communication range of the relay, the decoded packets are directly forwarded to the sink node.

As showed in Figure 6, during the routing procedure, the CH receives original data packets from member nodes and encodes the original data packets. The CH hears the data packets from regular nodes which are not its member node, drops them. When it hears a data packet from the neighbor with longer distance to the sink node, the CH checks weather it is helpful to decode if the next-hop of data packets is not the current ID. If received encoded packet have been decoded, CH drops it. If there is no association with the encoded packets saved, CH saves them and broadcasts data packets for a certain time. Otherwise, the received data packet is used to decode. For example, CH_1 successively hears encoded packets P_1, P_2, P_3 and P_4, $P_1 = d_1 \oplus d_2$, $P_2 = d_2 \oplus d_3$, $P_3 = d_1 \oplus d_3$, and $P_4 = d_4 \oplus d_5$. We assume d_1 have been decoded in CH_1, then d_2 is decoded using P_1, d_3 is decoded by P_2, however, P_3 is helpless for decoding any new original

(a) Without coding

(b) Coding

FIGURE 4: Coding theory.

(a) Full network coding
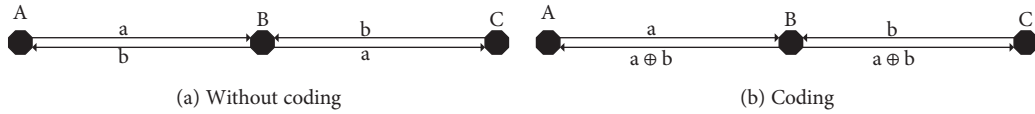
(b) Partial network coding
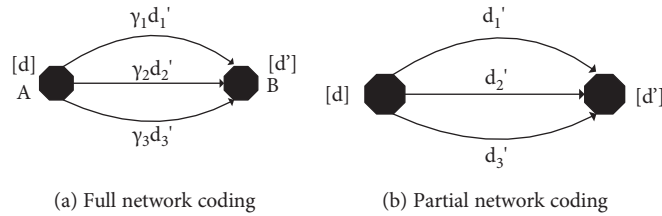
FIGURE 5: Full network coding and partial network coding.
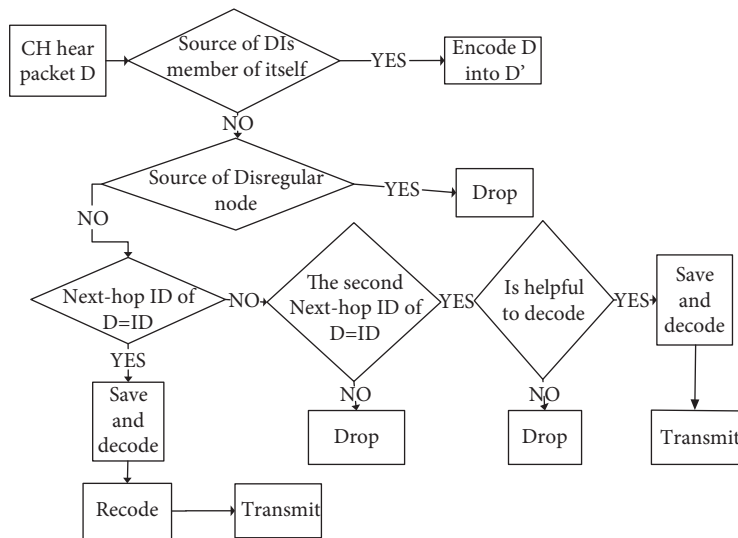
FIGURE 6: Encoding algorithm flow chart.

packet, CH_1 will drop P_3. While there is no association between data packets are encoded into P_4 and the encoded packets saved in CH_1, so CH_1 saves P_4 and broadcasts P_4 after a certain time.

The procedure of encoding algorithm is showed in Figure 6.

4.3.3. Routing Procedure. The detailed routing procedure is showed in Figure 7. After receiving a hello packet, cluster head checks three conditions including: (1) the hello packet is from a neighbor nearer to the sink node. (2) The residual energy is more than a preset value Re_{-th}. (3) The source node of D exits next-hop. When these three conditions meet requirements, the node calculates the priority $p(t)$ of the neighbor as (14). If the $p(t)$ is bigger than the priority value P_0 of the next-hop saved before, $p(t)$ replaces P_0. Otherwise, drop the hello packet.

5. Routing Maintained and Update

Because of the topology is mobile as the time goes by, routing needs to be updated timely. Here, there are two schemes to update route.

5.1. Scheme 1. In our protocol, data is transmitted block by block [27]. In scheme 1, control packets are introduced. After receiving the last packets in a block, the next-hop node reply ACK packets including the number and ID of recovered packets and unrecovered packets. When the ratio of recovered packets to transmitted packets is lower than 70%, the previous hop resends the unrecovered original packets. Meanwhile, the cluster head sends request packets to update routing. The neighbor nodes send reply packets after receiving hello packets according to the requirements in Figure 7. The node calculates the priority and updates the best next-hop.
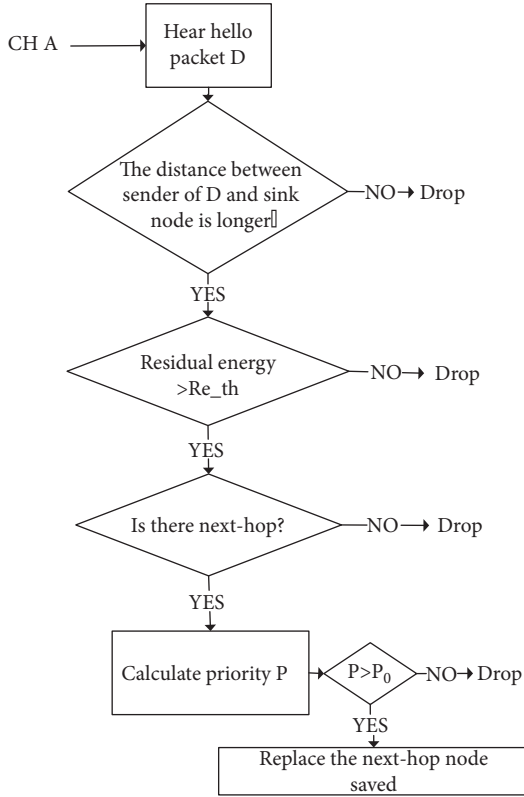
FIGURE 7: Routing algorithm flow chart.

The scheme 1 is simple to realize, and period broadcasting control packets is avoided. Extra control packets are decreased compared with the previous routing update algorithms, which decreases the collisions and energy consumption. Meanwhile, only the next-hop with lower delivery ratio is updated, and other nodes are not affected.

However, the back and forth time of the control packets is too long because of the long propagation delay in UWSNs. The unstable stage results in the failing to deliver data packets. Therefore, the scheme 2 of updating routing is proposed.

5.2. Scheme 2. We know, in our algorithm, the location information of nodes can be gotten. The updating algorithm can be designed according to the location information. As Figure 8, CH_1 is the sender and CH_2 and CH_3 are the neighbors of CH_1 with the shorter distance to the sink node. With the water flow by, CH_2 and CH_3 may run out of the communication range of CH_1 in some time. Because of the distance between CH_1 and its neighbors is different, the time varies. To get the average time of running out of the current cluster head for each neighbor, the expected value of time is calculated.

Comparing with the horizontal movement, the motion of vertical direction has a small range and can be ignored. The neighbors with shorter distance to the sink node are set as uniform distribution. The expected distance, $\overline{E(d)}$, running out of communication range is showed as (17). The expected
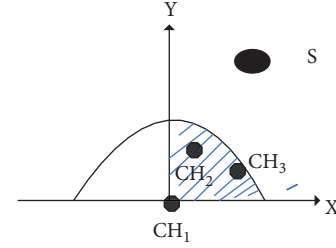
FIGURE 8: Expected time.

time is $\overline{E(t)}$ as showed in (18). Here, v is the water flow speed. The period of updating routing is set as $\overline{E(t)}$.

$$\overline{E(d)} = \int_0^R \int_0^R \left(\sqrt{R^2 - y^2} - x \right) dx dy, \tag{17}$$

$$\overline{E(t)} = \frac{\overline{E(d)}}{v}. \tag{18}$$

6. Performance Evaluation

6.1. Theoretical Analysis

6.1.1. The Size of a Block. To get the information of recovered data packets in next-hop, an ACK packet is necessary from the next-hop. To decrease the number of ACK packets, an ACK packet is sent for a block. The bigger the block, the less ACK to transmit constant data packets. However, because of the harsh environment under water, the bigger the block, the less probability of a successful delivery, which leads to too many re-transmission of original data packets. We know, the more original packets being transmission, the more energy consumption.

For the size of block is n_b packets and the packets is l bits, we assume the probability failing to deliver one bit is p. The probability of a block successfully delivery to next-hop is P as (19).

$$P = \left((1 - p)^l \right)^{n_b} = (1 - p)^{n_b l}. \tag{19}$$

Therefore, we should select moderate block size to balance the delivery ratio and energy consumption.

6.1.2. The Number of Encoded Packets. From the basic theory of coding, we know the number of sending encoded packets should be more than original packets to decode them into initial packets. In fact, the more linearly independent encoded packets are sent, the easier they are to decode. However, too many packets being transmitted wastes energy and results in collision. The effective transmission is defined as (20). μ can be adjusted according to ACK from the next-hop. When the ratio recovered packets to total transmitted original packets is lower than α_0, the number of sending encoded packets must be adjusted according to (21). $\alpha(t)$ is

the number ratio of recovered packets to total transmitted original packets at time t.

$$\mu = \frac{\text{number of sending encoded packets}}{\text{number of original data packets}}, \qquad (20)$$

$$\mu(t+1) = \mu(t) + \mu(t)(\alpha_0 - \alpha(t)). \qquad (21)$$

6.1.3. The Energy Consumption. We assume the total number of original packets is n_0 and the average ratio sending encoded packets to original packets is μ_0. Because the number ratio of recovered packets to total transmitted original packets fluctuates near α_0, the average value is set as α_0. The average hop is n_h. Therefore, the total number of sending data packets N' is showed as (22).

$$N' = n_0(1 + \mu_0) + n_0(1 - \alpha_0). \qquad (22)$$

In addition, the ACK packets are sent, and the number of ACK packets is relative with the size of block. So, the number of ACK packets n_a is showed in (23)

$$n_a = \frac{n_0}{n_b}. \qquad (23)$$

During initial phase and routing updating phase, the control packets are sent. The number of control packets is increased as the number of nodes. We assume the value is constant n_c. During routing update phase, in scheme 1, only the recovered ratio is lowered than 70%, the node sends request packet, and the neighbor sends reply packets. We set the number of control packets as n_{cu}. In scheme 2, the node update routing according to $\overline{E(t)}$. The number of sending control packets is $n_u = (T_l/\overline{E(t)})n_c$.

In our algorithm, for simplicity, the energy consumption of receiving packets is ignored, the energy consumption of sending a data packets and a control packet is set as e_d and e_c. Therefore, the energy consumption E in scheme 1 and scheme 2 are showed, respectively, as (24) and (25).

$$E = N'e_d + (n_c + n_{cu})e_c, \qquad (24)$$

$$E = N'e_d + \left(n_c + \frac{T_l}{\overline{E(t)}}n_c\right)e_c. \qquad (25)$$

6.2. Simulation Analysis. Because the cost of arranging the UWSNs is too high, simulations are adopted to evaluate the performance of the designed protocol. NS3 is a popular simulator to simulate UWSNs. NS3 offers some characteristics that other simulators have not, such as underpinning to discrete-event-driven networks, simulation of high-fidelity UWSNs channels, complete protocol stack, and mobile 3D networks. Firstly, the schemes of constructing cluster and updating routing are evaluated. Secondly, the influence of the node density and the number ratio of regular nodes to cluster heads on the performance of the system is tested. Lastly, we compare RSHSC with NCRP and VBF. NCRP uses network coding to greedily forward data packets to the sink.

VBF constructs a vector pipe from the source node to the sink node. Only the nodes in the pipe forward data.

In our simulations, the nodes are deployed in a 3D area with $3000 \, \text{m}^*3000 \, \text{m}^*2000 \, \text{m}$. The number of data packets is set as 60 in a block. When a node energy is exhausted, the simulation of this round is over. We show the average value of 50 runs. The detailed parameters are set as follows:

The data rate is 10 kbps. The center frequency is 12 KHZ. The bandwidth is 10 KHZ. Packet error rate model is ns3: UanPhyPerNoCode. Mode type is FSK. Signal noise model is ns3 :: Uan Phy Calc Sinr Default. Acoustic propagation speed is 1500 m/s. UAN Propagation model is ns3 :: Uan Prop Model Thorp. Energy model is acoustic modem energy model. MAC model is CWMAC. The mobility model is random walk 2D mobility model (speed: $2 \sim 4$ m/s, directions are chosen randomly). The payload of DATA is 64 bytes, and the number of data packets in each block is 60. Deployment region is 3D region of $3 \times 3 \times 2 \, \text{km}^3$. Node number is 20–75. The initial energy of advanced nodes is set as 100 J, and regular nodes is set as 25 J.

6.2.1. Performance at Different Cases. In our design, the ways of constructing clusters include SHSA and SHSB. Maintaining routing includes scheme 1 and scheme 2. Here, the number ratio of regular nodes to advanced node is $2:1$. To evaluate the performance of each scheme, four cases are studied as Table 4. Delivery ratio and network life are two important parameters to evaluate the performance of the protocol. Delivery ratio is the ratio of number of sink nodes received data packets to the number of regular nodes sent data packets. Network life is total performing time until the first node drains its energy. For simplicity, we replace network life with the ratio of network life to evaluate the performance of the protocol.

From Figure 9(a) (Supplementary material (available here)), the delivery ratio of SHSA is almost the same with SHSB. The SHSA is based on regular based during constructing cluster, which can make each regular node assigned to a cluster head. Some regular nodes are kicked out by all cluster heads in its coverage in SHSB, which leads to the data packets collected by these nodes cannot be delivered to the sink node. The delivery ratio of scheme 2 is lower than scheme 1. On the one hand, a large number of control packets cause collisions. On the other hand, the instability of the whole network leads to the failure of delivery. The instable stage in scheme 1 also leads to failure of delivery. However, the successful reception of an original packet may increase the delivery rate. Because the reception of an original packet can help to decode multiple encoding packets. The different cases are showed in Table 5. In Figure 9(b), the network life ratio is not almost affected by the SHSA and SHSB (Supplementary material). The network life of case 1 and case 2 is longer than case 3 and case 4. Because scheme 2 produces many control packets, which wastes energy. Combining the above simulation results, we continue to study the performance of the protocol based on case 1.

6.2.2. The Affection of Number Ratio of Regular Nodes to Advanced Nodes (RRTA). In Figure 10 (Supplementary

(a) The delivery ratio

(b) The network life ratio
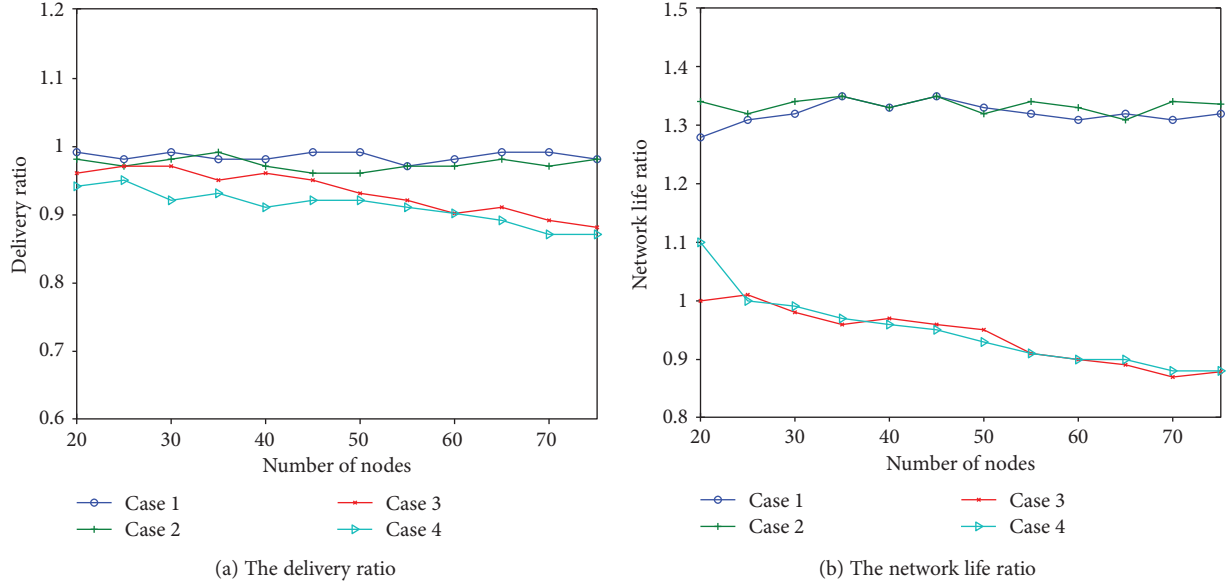
FIGURE 9: Affection of different schemes.

TABLE 5: Four cases.

Case number	Constructing cluster	Maintaining routing
Case 1	SHSA	Scheme 1
Case 2	SHSB	Scheme 1
Case 3	SHSA	Scheme 2
Case 4	SHSB	Scheme 2

material), N presents the layer numbers of advanced node being layout along vertical direction. We can see that the network life ratio decreases with the RRTA increasing, which is because the node first drains energy is regular node when the ratio is small. The regular nodes are in charge of only collecting data. The lifetime of regular nodes is related with the frequency of producing data packets and the initial energy. Meanwhile, the network life ratio decreases with the layer numbers increasing, because of the more layers, upper cluster heads consuming more energy than below nodes. In our simulation, the deliver ratio is about 60% when the communication range of nodes is 1000 m [27], and the vertical depth of the research area is 2000 m. Therefore, we select $N = 3$ and RRTA = 3.

6.2.3. Comparation with NCRP and VBF. NCRP is a cross-layer routing protocol based on network coding (NCRP) for UWSNs, which utilizes network coding and cross-layer design to greedily forward data packets to sink nodes efficiently [27]. We set 60 data packets in each transmission block. The degree distribution is degree value = [1 4 6], degree probability distribution = [0.500 0.075 0.425], and average degree = 3.35. In VBF, a vector pipe is created from the source to the sink node [30]. Only the node in the pipe is qualified to be the next-hop. To limit the number of forwarding nodes, the delay time of forwarding data for each node is set. In simulations, the routing pipe radius is set as 300 m, the time interval of forwarding a packet is set as $T_{\text{adaption}} = \sqrt{\alpha} \times$
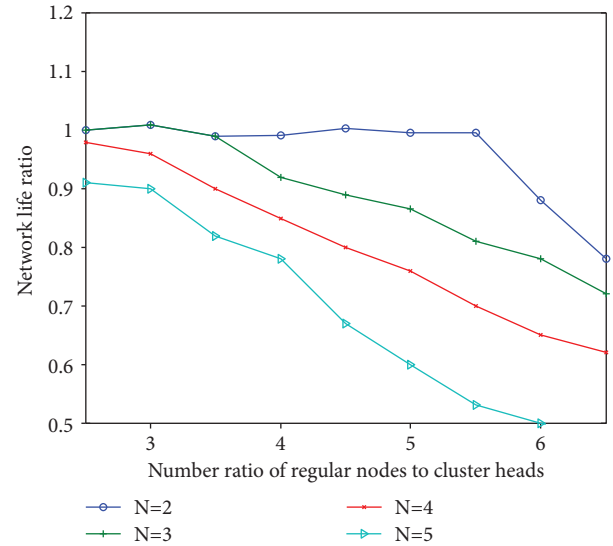
FIGURE 10: Affection of RRTA.

$T_{\text{delay}} + (R - d/v_0)$, α is calculated according to [30], T_{delay} is set as $0.02\sqrt{\bar{d}}$, $\bar{d}$ is the average distance among all nodes. R is the transmission radius. d is the distance between the current node and the forwarder. The other simulation parameters of VBF and NCRP are the same with the RSHSC.

From Figure 11(a) (Supplementary material), the delivery ratio of RSHSC is higher than VBF. Because in VBF, only the nodes in the pipe can forward data packets. However, in the sparse network, there may be no nodes in the pipeline, which leads to the failure of delivery. The delivery ratio of RSHSC is higher than NCRP. Although both the two protocols use coding techniques, the information of the next two hop is considered in RSHSC and avoids selecting void node as the next-hop. Figure 11(b) shows the comparison of energy consumption (Supplementary material). The energy

(a) Delivery ratio

(b) Energy consumption per packet

(c) End-to-end delay
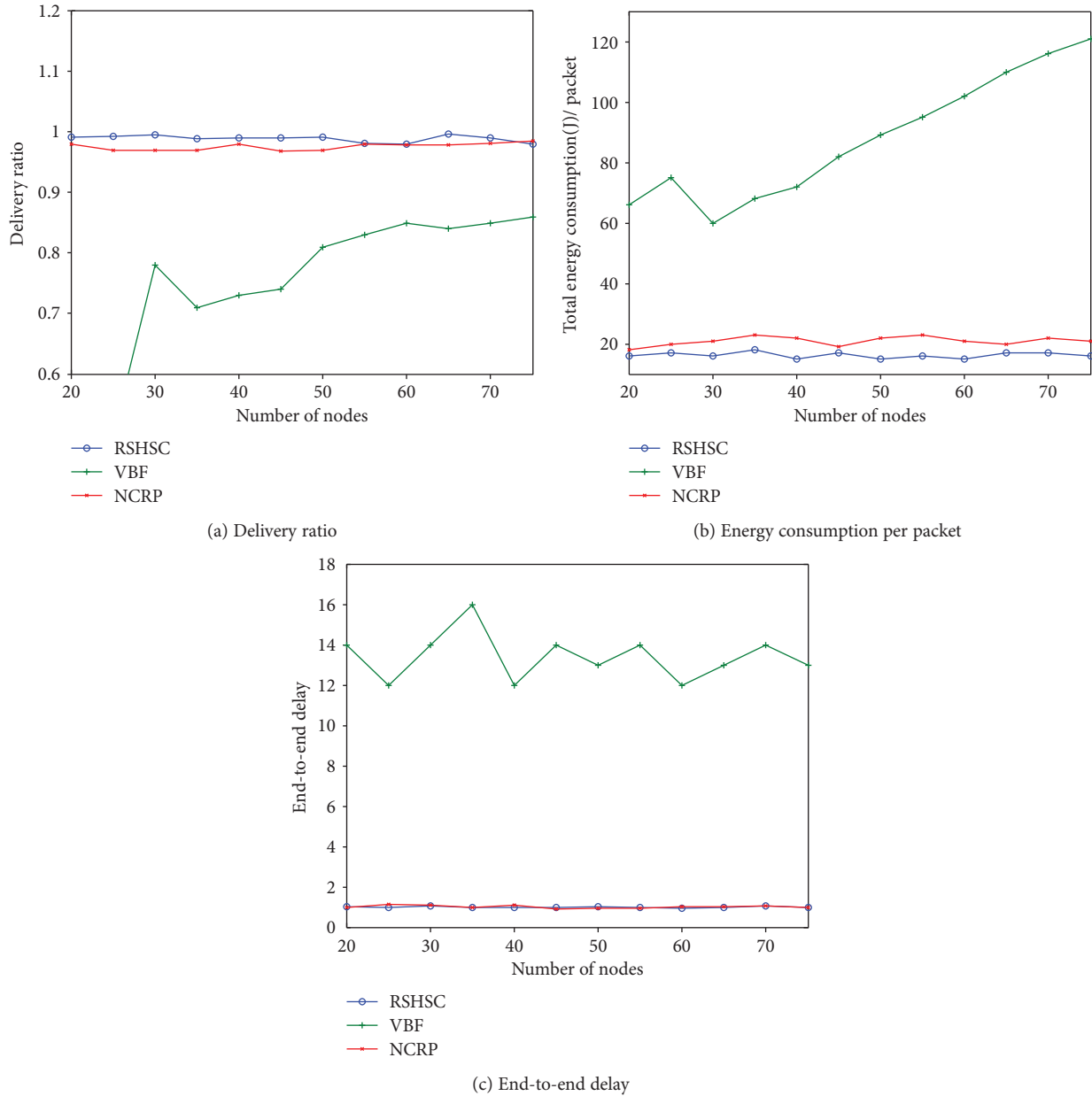
Figure 11: Comparison of performance.

consumption of VBF is higher than others, because VBF needs to send a large number of control packets. In addition, redundant forwarding exists in VBF. The energy consumption of RSHSC is lower than NCRP. In NCRP, the secondary nodes join to forward data packets, which wastes energy. While in RSHSC, only the best next-hop forwards data packets, and the data packets from other neighbors just join to decode. In addition, simplified harmony search algorithm is helpful to save energy of regular nodes and balance the energy among cluster heads. Figure 11(c) indicates the end-to-end delay of RSHSC is almost equal to NCRP and lower than VBF. Because VBF needs to wait to forward data packets, while NCRP and RSHSC transmit data block by block, the node immediately forward once

received a data packet. After transmitting a block, the acknowledgement is sent, which shortens waiting time.

7. Conclusion

In this paper, RSHSC, an energy effective and reliable routing protocol based on harmony search algorithm and coding, is proposed for UWSNs. The process of RSHSC can be mainly divided into four parts: initialization, constructing clusters, intercluster routing and routing maintenance. In the initialization phase, the control packets are sent and nodes got the information of each other. In the process of constructing routing, each regular node is assigned to a cluster head according to simplified harmony search algorithm. The

energy balance between cluster heads and the energy between ordinary nodes are taken into account when assigning. During the process of constructing routing, data packets are encoded. The best next-hop is responsible for forwarding data packets. The data packets from other neighbors is used to decode. The utilization of data packets from other neighbors increases the channel utilization. Meanwhile, the next two-hop is considered when selecting the best next-hop, which avoids the void node being selected as the next-hop. Two schemes are compared in the phase of maintaining routing. We get that scheme 1 is effective to save energy via theoretical analysis. Lastly, extensive simulations are conducted based NS-3. The results show that RSHSC is more effective than VBF and NCRP in decreasing energy consumption and increasing delivery ratio. In the future work, we will explore the implement of RSHSC and the better topology for improving the performance of UWSNs.

Data Availability

The data used to support the findings of this study are available from the corresponding author upon request. We agree that readers are free to use any data in the article.

Conflicts of Interest

The authors declare that they have no conflicts of interest.

Authors' Contributions

Meiju Li designed the experiments; Meiju Li and Chunyan Peng analyzed the data; Xiujuan Du contributed analysis tools; and Meiju Li and Xiujuan Du wrote the paper.

Acknowledgments

Supplementary Materials

The supplementary material provides the arranged data of NS-3 simulation results in Section 6.2. (*Supplementary Materials*)

References

[1] E. Felemban, F. K. Shaikh, U. M. Qureshi, A. A. Sheikh, and S. B. Qaisar, "Underwater sensor network applications: a comprehensive survey," *International Journal of Distributed Sensor Networks*, vol. 11, no. 11, Article ID 896832, 2015.

[2] M. Murad, A. A. Sheikh, M. A. Manzoor, E. Felemban, and S. Qaisar, "A survey on current underwater acoustic sensor network applications," *International Journal of Computer Theory and Engineering*, vol. 7, no. 1, pp. 51–56, 2015.

[3] J. Lloret, "Underwater sensor nodes and networks," *Sensors*, vol. 13, no. 9, pp. 11782–11796, 2013.

[4] X. Du, C. Peng, and K. Li, "A secure routing scheme for underwater acoustic networks," *International Journal of Distributed Sensor Networks*, vol. 13, no. 6, 2017.

[5] C. Peng, X. Du, K. Li, and M. Li, "An ultra-lightweight encryption scheme in underwater acoustic networks," *Journal of Sensors*, vol. 2016, Article ID 8763528, 10 pages, 2016.

[6] S. Climent, A. Sanchez, J. Capella, N. Meratnia, and J. Serrano, "Underwater acoustic wireless sensor networks: advances and future trends in physical, MAC and routing layers," *Sensors*, vol. 14, no. 1, pp. 795–833, 2014.

[7] M. Li, X. Du, K. Huang, S. Hou, and X. Liu, "A routing protocol based on received signal strength for underwater wireless sensor networks (UWSNs)," *Information*, vol. 8, no. 4, p. 153, 2017.

[8] S. Cai, N. Yao, and Z. Gao, "A reliable data transfer protocol based on twin paths and network coding for underwater acoustic sensor network," *EURASIP Journal on Wireless Communications and Networking*, vol. 2015, no. 1, 2015.

[9] X. Du, K. Li, X. Liu, and Y. Su, "RLT code based handshake-free reliable MAC protocol for underwater sensor networks," *Journal of Sensors*, vol. 2016, Article ID 3184642, 11 pages, 2016.

[10] M. R. Jafri, N. Javaid, N. Amjad, M. Akbar, Z. A. Khan, and U. Qasim, "Impact of acoustic propagation models on depth-based routing techniques in underwater wireless sensor networks," in *2014 28th International Conference on Advanced Information Networking and Applications Workshops*, pp. 479–485, Victoria, BC, Canada, 2014, IEEE.

[11] I. F. Akyildiz, D. Pompili, and T. Melodia, "Underwater acoustic sensor networks: research challenges," *Ad Hoc Networks*, vol. 3, no. 3, pp. 257–279, 2005.

[12] R. Headrick and L. Freitag, "Growth of underwater communication technology in the U.S. Navy," *IEEE Communications Magazine*, vol. 47, no. 1, pp. 80–82, 2009.

[13] S. Misra, S. Dash, M. Khatua, A. V. Vasilakos, and M. S. Obaidat, "Jamming in underwater sensor networks: detection and mitigation," *IET Communications*, vol. 6, no. 14, pp. 2178–2188, 2012.

[14] H. Yan, Z. J. Shi, and J. H. Cui, "DBR: depth-based routing for underwater sensor networks," in *NETWORKING 2008 Ad Hoc and Sensor Networks, Wireless Networks, Next Generation Internet*, vol. 4982 of Lecture Notes in Computer Science, pp. 72–86, Springer, Berlin, Heidelberg, 2008.

[15] A. Wahid, S. Lee, H. J. Jeong, and D. Kim, "EEDBR: energy-efficient depth-based routing protocol for underwater wireless sensor networks," in *Advanced Computer Science and Information Technology*, pp. 223–234, Springer, Berlin, Heidelberg, 2011.

[16] B. Diao, Y. Xu, Q. Wang et al., "A reliable depth-based routing protocol with network coding for underwater sensor networks," in *2016 IEEE 22nd International Conference on Parallel and Distributed Systems (ICPADS)*, pp. 270–277, Wuhan, Hubei, China, 2017, IEEE.

[17] H. Yu, N. Yao, T. Wang, G. Li, Z. Gao, and G. Tan, "WDFAD-DBR: weighting depth and forwarding area division DBR routing protocol for UASNs," *Ad Hoc Networks*, vol. 37, Part 2, pp. 256–282, 2016.

[18] J. Xu, K. Li, G. Min, K. Lin, and W. Qu, "Energy-efficient tree-based multipath power control for underwater sensor networks," *IEEE Transactions on Parallel and Distributed Systems*, vol. 23, no. 11, pp. 2107–2116, 2012.

[19] B. Ali, A. Sher, N. Javaid, S. Islam, K. Aurangzeb, and S. Haider, "Retransmission avoidance for reliable data delivery in underwater WSNs," *Sensors*, vol. 18, no. 2, p. 149, 2018.

[20] K. Hao, Z. Jin, H. Shen, and Y. Wang, "An efficient and reliable geographic routing protocol based on partial network coding for underwater sensor networks," *Sensors*, vol. 15, no. 6, pp. 12720–12735, 2015.

[21] S. Ahmed, N. Javaid, F. A. Khan et al., "Co-UWSN: cooperative energy-efficient protocol for underwater WSNs," *International Journal of Distributed Sensor Networks*, vol. 11, no. 4, Article ID 891410, 2015.

[22] A. Umar, N. Javaid, A. Ahmad et al., "DEADS: depth and energy aware dominating set based algorithm for cooperative routing along with sink mobility in underwater WSNs," *Sensors*, vol. 15, no. 6, pp. 14458–14486, 2015.

[23] N. Ilyas, T. A. Alghamdi, M. N. Farooq et al., "AEDG: AUV-aided efficient data gathering routing protocol for underwater wireless sensor networks," *Procedia Computer Science*, vol. 52, pp. 568–575, 2015.

[24] S. Ahmed and S. S. Kanhere, "HUBCODE: message forwarding using hub-based network coding in delay tolerant networks," in *Proceedings of the 12th ACM international conference on Modeling, analysis and simulation of wireless and mobile systems - MSWiM '09*, pp. 288–296, Tenerife, Canary Islands, Spain, 2009, ACM.

[25] I. Azam, N. Javaid, A. Ahmad, W. Abdul, A. Almogren, and A. Alamri, "Balanced load distribution with energy hole avoidance in underwater WSNs," *IEEE Access*, vol. 5, no. 99, pp. 15206–15221, 2017.

[26] H. Wu, M. Chen, and X. Guan, "A network coding based routing protocol for underwater sensor networks," *Sensors*, vol. 12, no. 4, pp. 4559–4577, 2012.

[27] H. Wang, S. Wang, R. Bu, and E. Zhang, "A novel cross-layer routing protocol based on network coding for underwater sensor networks," *Sensors*, vol. 17, no. 8, p. 1821, 2017.

[28] Z. Jin, Y. Ma, Y. Su, S. Li, and X. Fu, "A Q-learning-based delay-aware routing algorithm to extend the lifetime of underwater sensor networks," *Sensors*, vol. 17, no. 7, p. 1660, 2017.

[29] X. J. Du, K. J. Huang, S. L. Lan, Z. X. Feng, and F. Liu, "LB-AGR: level-based adaptive geo-routing for underwater sensor network," *The Journal of China Universities of Posts and Telecommunications*, vol. 21, no. 1, pp. 54–59, 2014.

[30] P. Xie, J. H. Cui, and L. Lao, "VBF: vector-based forwarding protocol for underwater sensor networks," in *NETWORKING 2006. Networking Technologies, Services, and Protocols; Performance of Computer and Communication Networks; Mobile and Wireless Communications Systems*, pp. 1216–1221, Springer, Berlin, Heidelberg, 2006.

Research Article

Wearable Lumbar-Motion Monitoring Device with Stretchable Strain Sensors

Hiroyuki Nakamoto [iD],[1] **Tokiya Yamaji,**[1] **Akio Yamamoto,**[2] **Hideo Ootaka,**[3] **Yusuke Bessho,**[3] **Futoshi Kobayashi** [iD],[1] **and Rei Ono**[2]

[1]*Graduate School of System Informatics, Kobe University, 1-1 Rokkodai-cho, Nada, Kobe 657-8501, Japan*
[2]*Graduate School of Health Science, Kobe University, 7-10-2 Tomogaoka, Suma, Kobe 654-0142, Japan*
[3]*Bando Chemical Industries Ltd, 4-6-6 Minatojima Minamimachi, Chuo, Kobe 650-0047, Japan*

Correspondence should be addressed to Hiroyuki Nakamoto; nakamoto@panda.kobe-u.ac.jp

Low-back pain is a common affliction. Epidemiological analyses have reported that periodic cycles of lumbar flexion and rotation are major risk factors for low-back pain. To prevent low-back pain, a lumbar-motion monitoring device could help diagnosticians assess patients' risk for low-back pain. This study proposes such a device that uses lightweight stretchable strain sensors. Six of these strain sensors form a parallel-sensor mechanism that measures rotation angles of lumbar motion in three axes. The parallel-sensor mechanism calculates rotation angles from the lengths of the strain sensors iteratively. Experimental results reveal that the prototype device is effective for lumbar-motion measurement and significantly improves in terms of wearability over comparable devices.

1. Introduction

Low-back pain (LBP) is a common affliction in contemporary life. Globally, two-thirds of adults experience LBP to the extent that treatment is required [1, 2]. Hoy et al. reported that the point prevalence of LBP is as much as 10%, and the 1-month prevalence is over 20% [3]. LBP sufferers often have difficulty maintaining healthy living habits and steady work.

Although the prevalence of LBP is not limited to a particular job category, industrial workers, nurses, and healthcare workers tend to experience a relatively high prevalence of LBP [4–11]. These workers frequently use their back muscles and spines in lumbar motions of flexion, rotation, and side bending. With epidemiological analysis, Hoogendoorn et al. revealed that periodic lumbar flexion and rotation is a major risk factor for LBP [12]. Overall, LBP risk is assessed in terms of accumulated lumbar motions and loads, and patients can benefit from alerts of excess lumbar motions to prevent the onset or worsening of LBP. Waters et al. estimated the

risk for LBP in manual lifting tasks with calculations [13]. Norman et al. assessed the risk for LBP in automotive industries using peak motion and cumulative lumbar motions as risk factors [14]. These methods are difficult to compare with each other, as they use different metrics for understanding lumbar risk. A measurement system that can continuously record time-series data during lumbar motions of flexion, rotation, and side bending could provide comparable lumbar data for a range of industries and subject groups.

To obtain time-series measurements of the pressure between lumbar bones, Lisi et al. obtained in vivo measurements with a load sensor inserted between lumbar vertebrae [15]. Wilke et al. measured the pressure between lumbar vertebrae during various motions such as lying, sitting, walking, and lifting and verified the results of Nachemson's study using EMG signals [16, 17]. Although these sensors directly provide the loads on lumbar vertebrae for various motions, such an invasive procedure cannot be used to continuously monitor movements for workers in practical environments. For less-invasive applications, camera-based

motion-capture systems are generally used to record human motions. Motion-capture systems require expensive cameras and markers on the bodies to be measured, and the measured subjects must remain within a small area. Wearable sensors could dramatically reduce costs and allow workers to move unimpeded while monitoring their movements.

Milea measured joint motion with lightweight and inexpensive bend sensors [18]. Though the materials used were simple and inexpensive, the three-axis motions possible at the lumbar joints cannot be measured with bend sensors alone.

Inertial measurement unit (IMU) systems have also been used to measure body motions. Since IMUs can estimate three-axis angles using accelerometers and gyroscopes, the measured values will include errors [19]. Marras et al. developed a lumbar-motion monitoring device that uses a three-axis electrogoniometer [20]. With this apparatus, Marras et al. monitored lumbar motion for industrial workers [21] and health care workers [22]. This lumbar-motion monitor effectively recorded time-series data about lumbar motions. However, the device covered the subjects' low back and may have been heavy for the subjects to work with over the course of a full shift. The weight of such a device must be reduced significantly if workers' low backs are to be monitored continuously.

We therefore propose a novel lightweight lumbar-motion measurement device (LMMD). The key component of the device is a flexible and stretchable strain sensor. This strain sensor is lightweight and features low elasticity, high durability, and good repeatability [23]. The strain sensor we use has been applied to measurements of wrist and elbow motions [24] and rapid prototyping human interfaces [25]. These joints rotate in one or two axes and can be modeled with a simple equation. Since lumbar motion includes flexion, rotation, and side bending, lumbar motion must be modeled with three degrees of freedom. To solve this problem, we designed a parallel-sensor device with six strain sensors. This device is lighter than comparable devices, and tests reported in this paper show that it can effectively measure lumbar motion over time.

2. Methods

The stretchable strain sensor we chose is flexible and thin. The main material of the strain sensor is urethane elastomer. Three elastomer sheets sandwich two carbon-nanotube membranes. These carbon-nanotube membranes work as electrodes in the strain sensor and are flexible enough to expand or contract along with the elastomer sheets. The sandwiched carbon-nanotube membranes are effectively a parallel-plate capacitor, the capacitance of which changes as the strain sensor expands and contracts. Hence, the strain sensor works as a variable capacitor, accurate to within 5% of its range [23]. The elastomer sheets are 70 mm long and 15 mm wide. The electrodes are 50 mm long and 10 mm wide. The whole strain sensor is approx. 150 μm thick [23]. The strain sensors we used have protective fabric on both sides, as shown in Figure 1. Snap buttons on both terminals are used to anchor terminals of the strain sensor. The strain
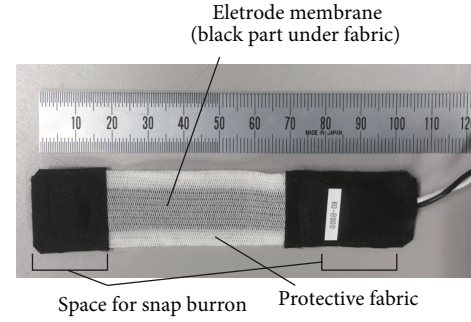
FIGURE 1: Stretchable strain sensor with protective fabric and snap buttons.
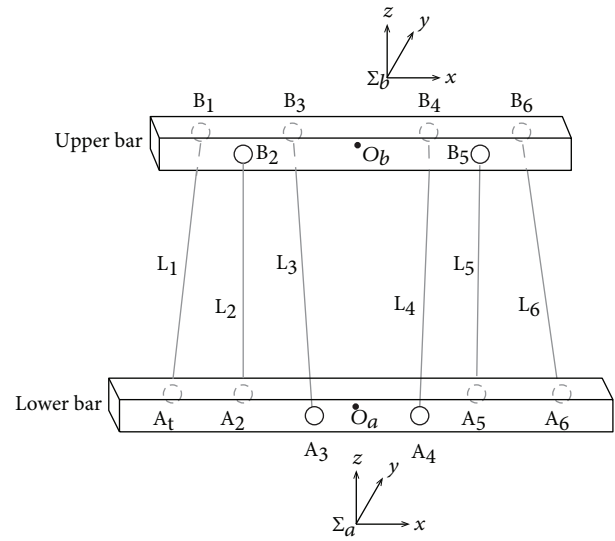
FIGURE 2: Model of the parallel-sensor mechanism. The origins of the coordinate systems of the lower and upper bars, Σ_a and Σ_b, are coincident with the center points of the bars, O_a and O_b, respectively.

sensor shown in Figure 1 is 110 mm long and 20 mm wide and weighs 4.1 g.

The proposed measurement device is built around a parallel-sensor mechanism. The parallel-sensor mechanism is based on the Stewart platform [26]. A diagram of the parallel-sensor mechanism is shown in Figure 2. Two bars are connected by six links. The terminals of each link are attached to the lower and upper bars. When the links are actuators, the mechanism is a positional control device with six degrees of freedom [27]. If the links are linear encoders, the mechanism can function as a measurement system [28]. In this study, as in our previous work, the strain sensors serve as links and the device measures their lengths. When the upper bar moves or tilts relative to the lower bar, the strain sensors expand or contract. In that case, the relative three-dimensional position and rotation of the upper bar can be calculated based on the lengths of the strain sensor.

The terminals of the links in the parallel-sensor model are labeled from A_1 to A_6 and from B_1 to B_6. The coordinate systems of the lower bar and upper bar are Σ_a and Σ_b,
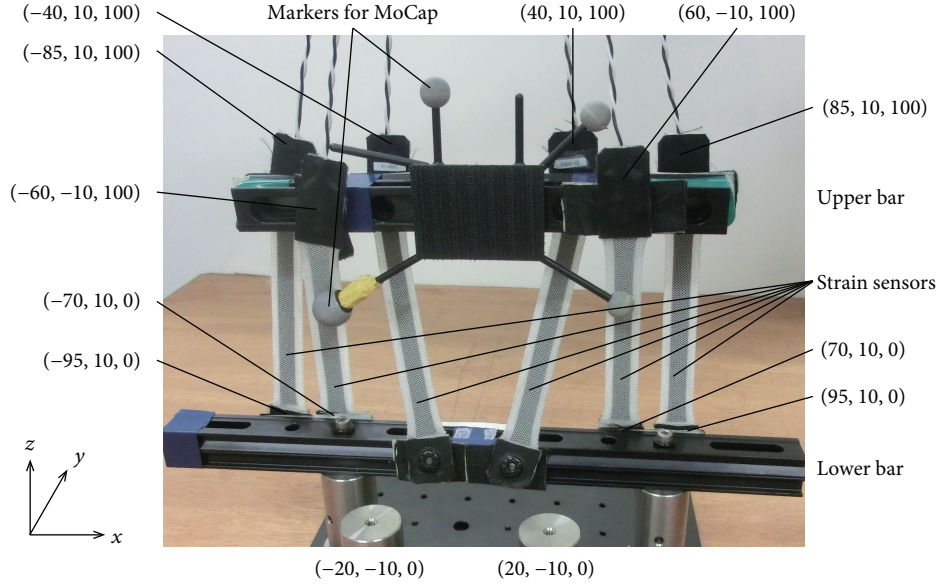
FIGURE 3: Parallel-sensor mechanism prototype. The origin of the coordinate system of the lower bar is at the center of the bar. The position of each terminal of the strain sensor in terms of the coordinate system is marked in units of mm.

respectively. The origin O_b of Σ_b is represented as ${}^aO_b = \left[{}^aO_{bx}\,{}^aO_{by}\,{}^aO_{bz}\right]^T$ in the coordinate system Σ_a. In coordination system Σ_a, the rotation angles of the upper bar around the x, y, and z axes are represented as θ_x, θ_y, and θ_z, respectively. The position and rotation of the origin of the upper bar are written as $P = \begin{bmatrix} {}^aO_{bx} & {}^aO_{by} & {}^aO_{bz} & \theta_x & \theta_y & \theta_z \end{bmatrix}^T$. Coordinates from B_1 to B_6 in Σ_b are represented as ${}^bB_i = \begin{bmatrix} {}^bB_{ix} & {}^bB_{iy} & {}^bB_{iz} \end{bmatrix}^T$, where i is the index number of the sensor and ranges from 1 to 6. Similarly, the coordinates from B_1 to B_6 in Σ_a are represented as ${}^aB_i = \begin{bmatrix} {}^aB_{ix} & {}^aB_{iy} & {}^aB_{iz} \end{bmatrix}^T$, which is calculated from P. The coordinates from A_1 to A_6 in Σ_a are ${}^aA_i = \begin{bmatrix} {}^aA_{ix} & {}^aA_{iy} & {}^aA_{iz} \end{bmatrix}^T$. ${}^bB_i$ and ${}^aA_i$ are predefined constants. The lengths of the strain sensors are represented as L_{si}. L_i is obtained by the following equation.

$$L_i = {}^aB_i - {}^aA_i = \begin{bmatrix} L_{ix} & L_{iy} & L_{iz} \end{bmatrix}^T. \tag{1}$$

The equation expresses the relation between L_i and P. If we consider the difference between L_{si} and L_i as the length $\dot{L}_i$ changes

$$\dot{L}_i = L_{si} - L_i, \tag{2}$$

the following equation can be derived using the Jacobian determinant J.

$$\dot{P} = J^{-1}\dot{L}_i. \tag{3}$$

From the difference between L_i and L_{si}, the change in position and rotation of the upper bar $\dot{P}$ is determined iteratively by Newton's method. The position and rotational
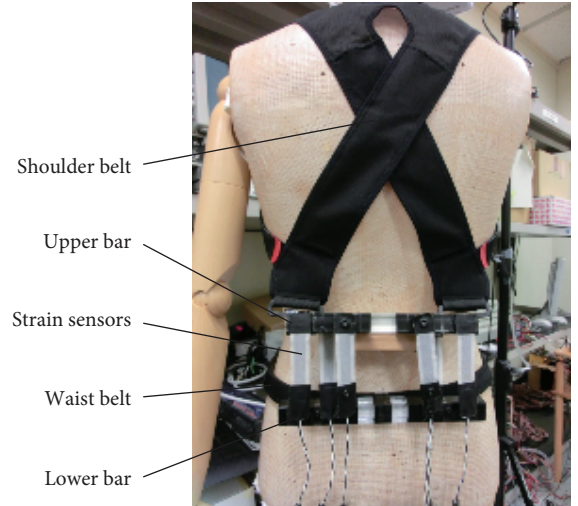
FIGURE 4: Prototype of LMMD on the low back of mannequin.

orientation of the upper bar P is calculated by adding $\dot{P}$ to the previous P.

The prototype parallel-sensor mechanism we constructed is pictured in Figure 3. The parallel-sensor mechanism is built from two rectangular bars and six strain sensors, as shown in Figure 3. The dimensions of the upper and lower rectangular bars are $20 \times 200 \times 20\,\text{mm}$ and $20 \times 260 \times 20\,\text{mm}$, respectively. One terminal of each strain sensor is fixed on the upper bar, and the other terminal is fixed on the lower bar. Although the length between the two bars is about 100 mm in this picture, the default length is 80 mm. The prototype weighs 235 g.

The upper and lower bars are worn on the back over the first lumbar vertebra and the fifth lumbar vertebra with shoulder straps and a waist belt, as pictured in Figure 4. The overall weight of the sensor mechanism with straps is

480 g. The weight of the LMMD is lighter than that of the lumbar-motion monitor in [20]. This configuration assumes that the relative position and twist of the upper and lower bars change along with the motions of the first and fifth lumbar spines. As the relative position of the two bars changes, the capacitances of the strain sensors change. A capacitance-to-voltage converter processes the signals into voltages that are recorded by an analog-to-digital converter running on a desktop computer. The computer translates voltages into lengths of the strain sensors and iteratively calculates the relative position and rotation of the upper bar.

3. Results and Discussion

3.1. Parallel-Sensor Mechanism. First, a preliminary experiment was conducted to confirm the accuracy of the parallel-sensor mechanism. The lower bar was fixed on a table. The bend angle and rotation of the upper bar were manipulated by a hand. The computer sampled the lengths of the strain sensors at 20 Hz and calculated the displacement and rotation in three dimensions. An optical motion-capture system (Optitrack, NaturalPoint, USA) simultaneously measured the displacement and rotation of the upper bar from markers attached to the bar, as pictured in Figure 3. The motion-capture data were used as reference data. Overall, ten trials were performed to compare data from the parallel-sensor mechanism and motion-capture system. Each trial lasted for about 25 s. Typical results from these tests are shown in Figure 5. We calculated the cross-correlation values between the motion-capture data and the parallel-sensor mechanism data. The cross-correlation values of x, y, z, flexion-extension, side bending, and rotation were 0.84, 0.93, 0.83, 0.84, 0.94, and 0.93, respectively. The parallel-sensor mechanism data agreed well with those from the motion-capture system, with some error that we assume to be caused by errors in the individual length measurements.

The accuracy of the parallel-sensor mechanism was quantified using the residual errors between the parallel-sensor mechanism and the motion-capture data. The mean and standard deviation (SD) of each dataset are listed in Table 1. Table 1 also lists the ranges of motion (ROM). The means for side bending and rotation were within 2° and were small. Compared to the data for these motions, the difference in the mean of the flexion-extension data was large. The means of the displacement data were nearly a function of the measured ROM. The ROM in the x-axis was limited by the maximum length of the sensors and was smaller than that of the other axes.

3.2. Lumbar-Motion Monitoring Device. We also tested LMMD with human subjects. Our study protocol complied with the Declaration of Helsinki. All participants were fully informed and provided written informed consent before participating in the study. The study and all procedures were approved by the Ethical Committee of Graduate School of System Informatics, Kobe University (Permission number: 28-03). The human subjects were ten volunteers of average dimensions: female : male = 1 : 1, mean age: 19.8 ± 1.0 years, height: 164.9 ± 11.9 cm, and weight: 58.1 ± 18.2 kg. The

human subjects wore the LMMD and adjusted the tension of the straps to fit it to their low backs. Subjects were instructed to perform a motion typically encountered by nursing professionals, i.e., the transfer of a patient from bed to a wheelchair. Each subject performed the motion twice. The motion-capture system was used to obtain reference data as it was in the preliminary test. A selection of typical results is shown in Figure 6. The motion-capture data for flexion and extension had missing values due to a marker that was not detected by the motion-capture system. Excluding the missing data, the cross-correlation values of flexion-extension, side bending, and rotation were 0.78, 0.89, and 0.79, respectively. Although the results differ somewhat, the LMMD data still agree reasonably with the reference data. Table 2 lists the mean and SD of the residual errors between the LMMD and the motion capture and the ROM of the LMMD. The mean for the side bending angle was relatively small, and flexion-extension motions had more than double the error of the other motions.

3.3. Discussion. The comparison of data from the parallel-sensor mechanism and motion-capture system demonstrates the validity of the proposed measurement device. The cross-correlation values showed strong positive correlations. The difference in the means of the measurement and reference angles was less than 4.5°, which is less than 8.3% of the ROM of the device. These results show that the parallel-sensor mechanism with strain sensors can measure rotation in three dimensions with reasonable accuracy.

In the tests with human subjects, the cross-correlation values also showed strong positive correlations. The ROMs of the side bending and rotation motion were small compared to that of flexion-extension and were less than 35°. The ROM of the flexion-extension was greater than 50°. Although these ROMs are expected for the single motion we tested, the device must measure rotation around all three axes to be effective. The differences in the means of the side bending and rotation measurements were less than 5°. In contrast, measurements of the flexion-extension motion returned errors greater than 10°. Two explanations of these errors seem likely. First, we note that arrangement of the sensors will lead to some error due to geometry. The Stewart platform has circular plates and places links at dispersed positions on those plates; however, the LMMD terminals are attached to sensors linked to a smaller range of positions on the upper and lower bars. In this arrangement, the sensor lengths change less as the upper bar moves than they would in the Stewart platform. The other cause is that the sensors are stretched along the curve of the low back so they do not remain straight as they move. The Jacobian matrix calculation then generates errors in the angle calculations; therefore, the length of the sensor is not accurately recorded as it bends. Improved bars and belts are required to prevent these errors. Sensors could be distributed evenly around the waist, and they could be kept straight. These limitations decrease the latitude of the design of bars and belts. For example, extremely downsizing the device is difficult. The errors yielded by this LMMD are acceptable for practical purposes, though, because the device is more wearable than similar

(a) *x*-axis displacement

(b) *y*-axis displacement

(c) *z*-axis displacement

(d) Flexion-extension

(e) Side bending
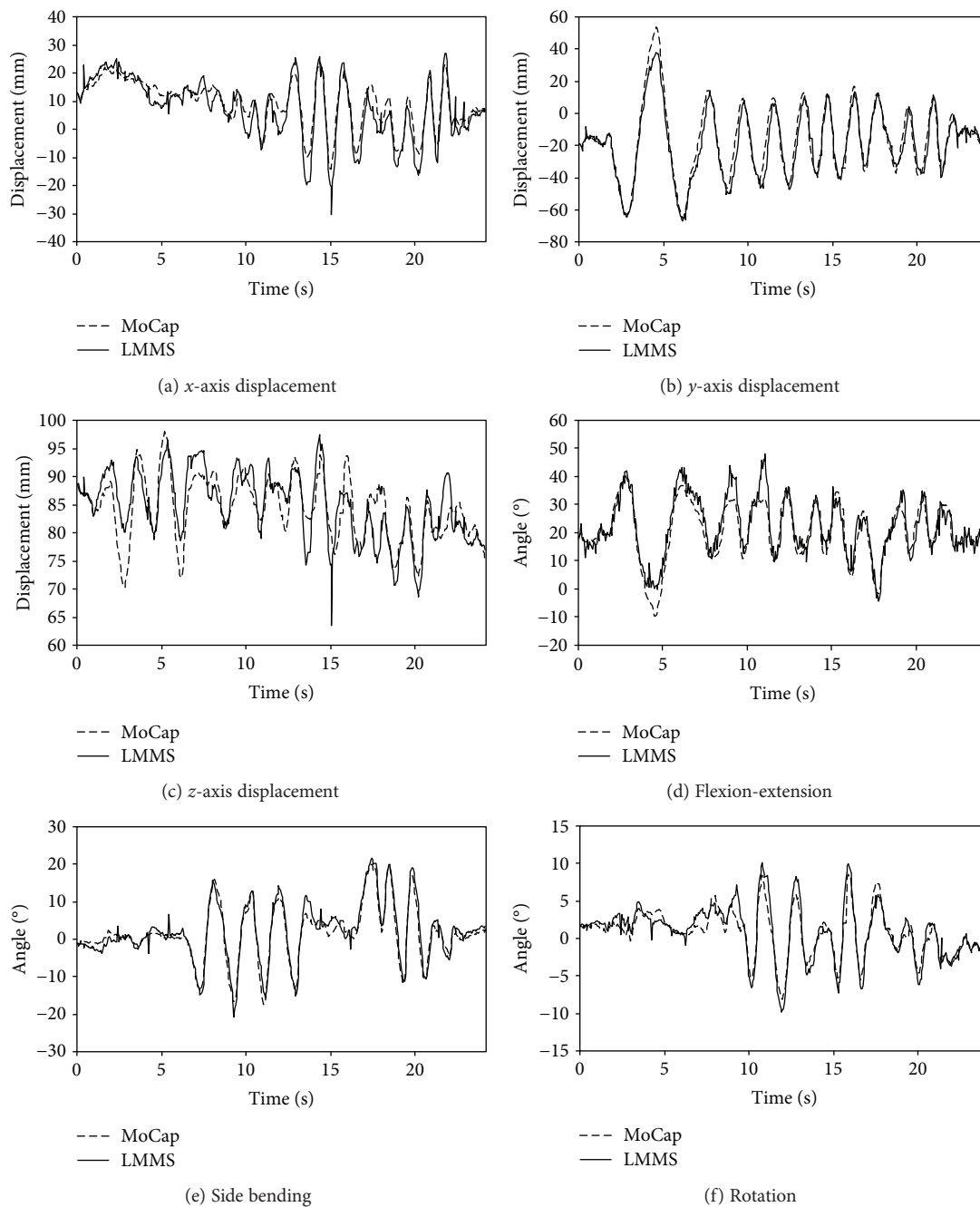
(f) Rotation

FIGURE 5: Typical time-series data for displacements and rotation angles when moving the parallel-sensor mechanism alone.

TABLE 1: Range of motion values and means and SDs of residual errors between measured and reference displacements and rotation angles in preliminary tests with the parallel-sensor mechanism on a bench.

Axis	Displacement (mm)			Angle (°)		
	x	*y*	*z*	Flexion-extension	Side bending	Rotation
ROM	56.69	131.97	84.56	51.24	22.13	67.35
Mean	3.23	5.42	2.79	4.22	1.04	1.52
SD	3.24	5.43	2.36	3.43	1.02	2.17

devices that have been proposed. The device could be effective for rough measurements and monitoring of multiaxis lumbar motion such as the transfer of a patient.

4. Conclusion

We developed a lumbar-motion monitoring device that uses flexible and stretchable strain sensors. The LMMD measured three-axis lumbar motion using a parallel-sensor mechanism with six strain sensors. The accuracy of the parallel-sensor mechanism was evaluated as the residual errors within 4.5°, and this may be sufficient for a wearable lumbar-motion

(a) Flexion-extension

(b) Side bending
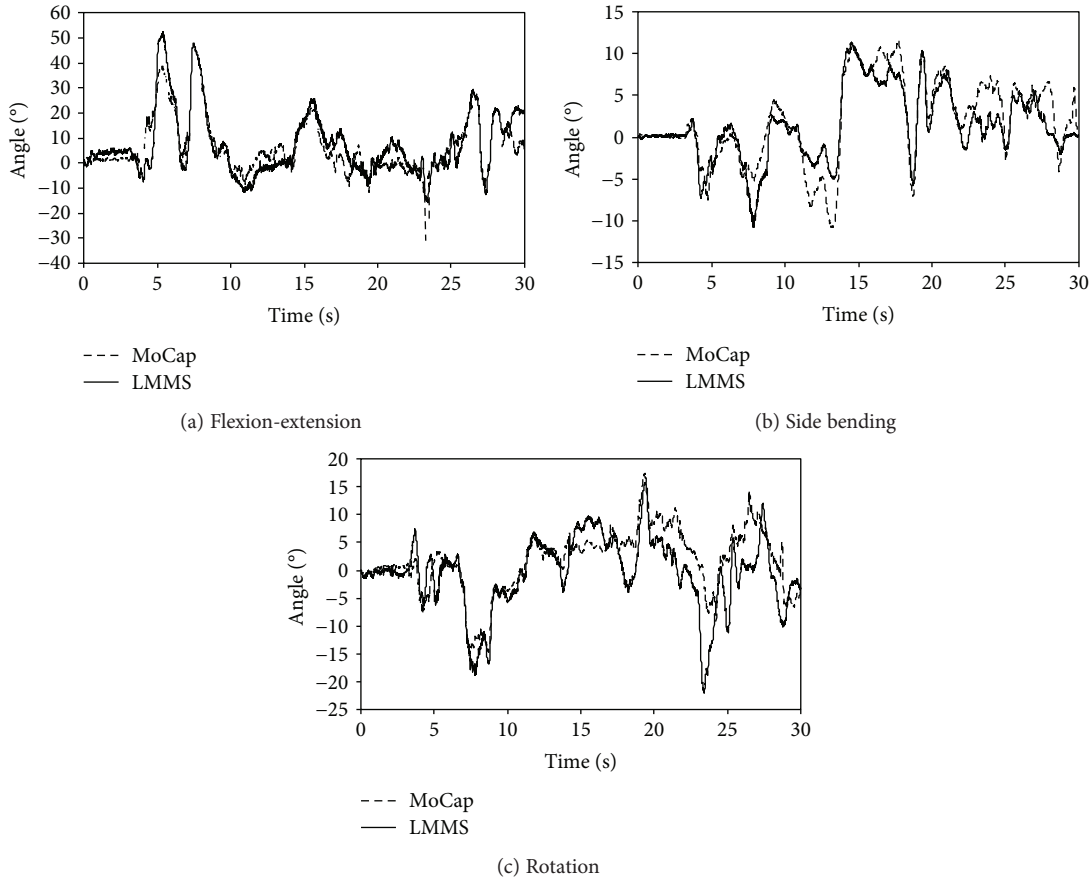
(c) Rotation

FIGURE 6: Typical time-series data of rotation angles for the device worn by human subjects.

TABLE 2: ROM values and means and SDs of residual errors between measured and reference rotation angles in human-subject experiments.

Axis	Flexion-extension	Side bending	Rotation
ROM°	54.64	31.78	34.01
Mean°	11.11	3.26	4.64
SD°	7.47	3.09	3.79

monitoring device. The accuracy of the LMMD for tracking low-back movements of human subjects was evaluated against reference data from a motion-capture system. The accuracy of the LMMD was slightly inferior when worn by human subjects.

In future work, we plan to implement an arc-shaped bar that fits the user's waist better. If the sensors are evenly distributed to the arc-shaped bar, the LMMD could have high accuracy. We also plan to improve the device as a wireless device and to adapt the measurement device for continuous monitoring to make it practical for preventing LBP in the workplace.

Data Availability

The relevent data used to support the findings of this study are included within the article.

Ethical Approval

All procedures used in this research were approved by the Ethical Committee of Graduate School of System Informatics, Kobe University (Permission number: 28-03).

Disclosure

The funders provided part of the experimental materials used for data collection, but this does not alter our adherence to the publication ethics of the journal on sharing data and materials.

Conflicts of Interest

YB and HO are employees of Bando Chemical Industries, Ltd. All other authors declare that they have no conflicts of interest.

References

[1] C. Leboeuf-Yde, N. Klougart, and T. Lauritzen, "How common is low back pain in the Nordic population? Data from a recent

study on a middle-aged general Danish population and four surveys previously conducted in the Nordic countries," *Spine*, vol. 21, no. 13, pp. 1518–1525, 1996.

[2] R. A. Deyo and J. N. Weinstein, "Low back pain," *The New England Journal of Medicine*, vol. 344, no. 5, pp. 363–370, 2001.

[3] D. Hoy, C. Bain, G. Williams et al., "A systematic review of the global prevalence of low back pain," *Arthritis and Rheumatism*, vol. 64, no. 6, pp. 2028–2037, 2012.

[4] A. Leclerc, F. Tubach, M. F. Landre, and A. Ozguler, "Personal and occupational predictors of sciatica in the GAZEL cohort," *Occupational Medicine*, vol. 53, no. 6, pp. 384–391, 2003.

[5] L. Punnett, L. J. Fine, W. M. Keyserling, G. D. Herrin, and D. B. Chaffin, "Back disorders and nonneutral trunk postures of automobile assembly workers," *Scandinavian Journal of Work, Environment and Health*, vol. 17, no. 5, pp. 337–346, 1991.

[6] H. Miranda, E. Viikari-Juntura, L. Punnett, and H. Riihimäki, "Occupational loading, health behavior and sleep disturbance as predictors of low-back pain," *Scandinavian Journal of Work, Environment and Health*, vol. 34, no. 6, pp. 411–419, 2008.

[7] I. Niedhammer, F. Lert, and M. J. Marne, "Back pain and associated factors in French nurses," *International Archives of Occupational and Environmental Health*, vol. 66, no. 5, pp. 349–357, 1994.

[8] J. Smedley, P. Egger, C. Cooper, and D. Coggon, "Manual handling activities and risk of low back pain in nurses," *Occupational and Environmental Medicine*, vol. 52, no. 3, pp. 160–163, 1995.

[9] A. M. Trinkoff, J. A. Lipscomb, J. Geiger-Brown, C. L. Storr, and B. A. Brady, "Perceived physical demands and reported musculoskeletal problems in registered nurses," *American Journal of Preventive Medicine*, vol. 24, no. 3, pp. 270–275, 2003.

[10] T. Videman, A. Ojajärvi, H. Riihimäki, and J. D. G. Troup, "Low back pain among nurses: a follow-up beginning at entry to the nursing school," *Spine*, vol. 30, no. 20, pp. 2334–2341, 2005.

[11] R. Ono, S. Yamazaki, M. Takegami et al., "Patient-reported disability in the general Japanese population was associated with medical care visits for low back pain, regardless of pain intensity," *Journal of Orthopaedic Science*, vol. 20, no. 4, pp. 742–749, 2015.

[12] W. E. Hoogendoorn, P. M. Bongers, H. C. W. de Vet et al., "Flexion and rotation of the trunk and lifting at work are risk factors for low back pain: results of a prospective cohort study," *Spine*, vol. 25, no. 23, pp. 3087–3092, 2000.

[13] T. R. Waters, V. Putz-Anderson, A. Garg, and L. J. Fine, "Revised NIOSH equation for the design and evaluation of manual lifting tasks," *Ergonomics*, vol. 36, no. 7, pp. 749–776, 1993.

[14] R. Norman, R. Wells, P. Neumann et al., "A comparison of peak vs cumulative physical work exposure risk factors for the reporting of low back pain in the automotive industry," *Clinical Biomechanics*, vol. 13, no. 8, pp. 561–573, 1998.

[15] A. J. Lisi, C. W. O'Neill, D. P. Lindsey, R. Cooperstein, E. Cooperstein, and J. F. Zucherman, "Measurement of in vivo lumbar intervertebral disc pressure during spinal manipulation: a feasibility study," *Journal of Applied Biomechanics*, vol. 22, no. 3, pp. 234–239, 2006.

[16] H.-J. Wilke, P. Neef, M. Caimi, T. Hoogland, and L. E. Claes, "New in vivo measurements of pressures in the intervertebral disc in daily life," *Spine*, vol. 24, no. 8, pp. 755–762, 1999.

[17] A. L. Nachemson, "The lumbar spine an orthopaedic challenge," *Spine*, vol. 1, no. 1, pp. 59–71, 1976.

[18] L. Milea, "Detection and tele-replication of human hand motions by a robotic hand," *American Journal of Aerospace Engineering*, vol. 2, no. 4, p. 30, 2015.

[19] M. C. Schall Jr, N. B. Fethke, H. Chen, and F. Gerr, "A comparison of instrumentation methods to estimate thoracolumbar motion in field-based occupational studies," *Applied Ergonomics*, vol. 48, pp. 224–231, 2015.

[20] W. S. Marras, F. A. Fathallah, R. J. Miller, S. W. Davis, and G. A. Mirka, "Accuracy of a three-dimensional lumbar motion monitor for recording dynamic trunk motion characteristics," *International Journal of Industrial Ergonomics*, vol. 9, no. 1, pp. 75–87, 1992.

[21] W. S. Marras, W. G. Allread, D. L. Burr, and F. A. Fathallah, "Prospective validation of a low-back disorder risk model and assessment of ergonomic interventions associated with manual materials handling tasks," *Ergonomics*, vol. 43, no. 11, pp. 1866–1886, 2000.

[22] W. S. Marras, K. G. Davis, B. C. Kirking, and P. K. Bertsche, "A comprehensive analysis of low-back disorder risk and spinal loading during the transferring and repositioning of patients using different techniques," *Ergonomics*, vol. 42, no. 7, pp. 904–926, 1999.

[23] H. Nakamoto, H. Ootaka, M. Tada, I. Hirata, F. Kobayashi, and F. Kojima, "Stretchable strain sensor based on areal change of carbon nanotube electrode," *IEEE Sensors Journal*, vol. 15, no. 4, pp. 2212–2218, 2015.

[24] H. Nakamoto, H. Ootaka, M. Tada, I. Hirata, F. Kobayashi, and F. Kojima, "Stretchable strain sensor with anisotropy and application for joint angle measurement," *IEEE Sensors Journal*, vol. 16, no. 10, pp. 3572–3579, 2016.

[25] T. Yamaji, H. Nakamoto, H. Ootaka, I. Hirata, and F. Kobayashi, "Rapid prototyping human interfaces using stretchable strain sensor," *Journal of Sensors*, vol. 2017, Article ID 9893758, 9 pages, 2017.

[26] D. Stewart, "A platform with six degrees of freedom," *Proceedings of the Institution of Mechanical Engineers*, vol. 180, no. 1, pp. 371–386, 1965.

[27] R. C. Merkle, "A new family of six degrees of freedom positional devices," *Nanotechnology*, vol. 8, no. 2, pp. 47–52, 1997.

[28] Y. Kitano and K. Yokota, "Method for measuring position and posture of the shoulder skeleton using parallel links," *Transactions of the Japan Society of Mechanical Engeneers, Series C*, vol. 79, no. 802, pp. 2004–2012, 2013.

Research Article

Intensity and Wavelength Division Multiplexing FBG Sensor System Using a Raman Amplifier and Extreme Learning Machine

Yibeltal Chanie Manie [ID],[1] **Run-Kai Shiu,**[1] **Peng-Chun Peng** [ID],[1] **Bao-Yi Guo,**[1] **Mekuanint Agegnehu Bitew** [ID],[2] **Wei-Chieh Tang,**[1] **and Hung-Kai Lu**[1]

[1]*Department of Electro-Optical Engineering, National Taipei University of Technology, Taipei, Taiwan*
[2]*Department of Computer Science, Bahir Dar University, Bahir Dar, Ethiopia*

Correspondence should be addressed to Peng-Chun Peng; pcpeng@ntut.edu.tw

A fiber Bragg grating (FBG) sensor is a favorable sensor in measuring strain, pressure, vibration, and temperature in different applications, such as in smart structures, wind turbines, aerospace, industry, military, medical centers, and civil engineering. FBG sensors have the following advantages: immune to electromagnetic interference, light weight, small size, flexible, stretchable, highly accurate, longer stability, and capable in measuring ultra-high-speed events. In this paper, we propose and demonstrate an intensity and wavelength division multiplexing (IWDM) FBG sensor system using a Raman amplifier and extreme learning machine (ELM). We use an IWDM technique to increase the number of FBG sensors. As the number of FBG sensors increases and the spectra of two or more FBGs are overlapped, a conventional peak detection (CPD) method is inappropriate to detect the central Bragg wavelength of each FBG sensor. To solve this problem, we use ELM techniques. An ELM is used to accurately detect the central Bragg wavelength of each FBG sensor even when the spectra of FBGs are partially or fully overlapped. Moreover, a Raman amplifier is added to a fiber span to generate a gain medium within the transmission fiber, which amplifies the signal and compensates for the signal losses. The transmission distance and the sensing signal quality increase when the Raman pump power increases. The experimental results revealed that a Raman amplifier compensates for the signal losses and provides a stable sensing output even beyond a 45 km transmission distance. We achieve a remote sensing of strain measurement using a 45 km single-mode fiber (SMF). Furthermore, the well-trained ELM wavelength detection methods accurately detect the central Bragg wavelengths of FBG sensors when the two FBG spectra are fully overlapped.

1. Introduction

Fiber optic sensors are important in smart structures, mostly as a transmission line, as a sensing medium, or a combination of both. Fiber Bragg grating (FBG) is a favorable fiber optic sensor to measure strain, pressure, vibration, and temperature in different applications, such as in smart structures, wind turbines, aerospace, industry, military, medical centers, and civil engineering. In addition, applications of FBG sensors related to bridge monitoring, damage detection, structural health monitoring, railway transportation applications, and other harsh environment applications [1–3]. FBG sensors have the advantages of being immune to electromagnetic interference, light weight, small size,

highly accurate, longer stability, and capable in measuring ultra-high-speed events. The sensing characteristics of FBG sensors involve identifying the variation of the central Bragg wavelength when it is subjected to physical parameters like vibration, strain, temperature, and other changes in the properties of the sensor [4–6]. Multiplexing of FBG sensors is an effective technology to deliver multipoint measurement along a single-fiber cable. Multiplexing reduces the operation and installation costs for quasidistributive strain measurements [7]. Among the various multiplexing techniques, wavelength division multiplexing (WDM) is an essential mechanism to recognize the exact central wavelength of each FBG sensor within the sensor network [7, 8]. In WDM, each FBG sensor needs a different Bragg wavelength and no

spectral overlap is allowed. However, the number of multiplexed sensors is restricted by both the broadband source bandwidth and the operating wavelength range required for each FBG sensor [9].

Recently, researchers have proposed intensity and wavelength division multiplexing (IWDM) techniques to increase the number of FBG sensors to be multiplexed [8–10]. IWDM has the advantage of low complexity. The IWDM scheme proposed in [9] used tunable fiber ring laser as a light source and a Fabry–Perot filter to select different wavelengths. However, this scheme is inappropriate for long-distance environment sensing, as it does not amplify the FBG signal. In [10], the authors proposed capacity and capability enhancement of the FBG sensor system using IWDM technique. However, IWDM has a problem of unmeasurable gap when two or more FBG spectra are partially or fully overlapped. Overlapping spectra cause crosstalk among the sensors and induce errors in central Bragg wavelength detection. Moreover, IWDM have a restriction on long-distance transmission when the number of FBG sensors increases. Nowadays, in addition to increasing the number of FBG sensors using IWDM, increasing the signal transmission distance is a very important issue.

In FBG sensor systems, the maximum signal transmission distance is commonly limited to 25 km due to signal loss in fiber link and Rayleigh scattering [11–16]. Moreover, signal loss and Rayleigh scattering induce optical noise and degrade the transmitted signal quality. Signal amplification is very important for long-distance transmission and remote sensing functionality. Among different optical signal amplification techniques, Raman amplification is the best amplifier to increase the transmission distance. Raman amplification entails generating a gain medium within the transmission fiber, which amplifies the signal before it reaches the optical receiver. Raman amplification has the capacity to amplify signals in any wavelength band using an appropriate pumping scheme [13–15]. By adding a Raman amplifier to a fiber span, signal power loss is decreased and it highly improves the signal-spontaneous beat noise performance. In order to realize a long-distance FBG sensor system, several approaches are proposed [13–17]. In [13], Raman laser for long-distance sensing has been demonstrated. However, FBGs are grouped together in the direction of the end of a long fiber, and consequently, the dynamic range of the interrogator is not possible to extend as it affects the response time of the system. Scheme [17] proposed linear-cavity fiber Raman laser for a long-distance FBG sensor system. The cavity consists of two FBGs connected to a fiber loop mirror. However, a fiber loop mirror has a limiting factor in system stability and configuration complexity. In addition, when strain is applied, the spectra of two FBGs might be overlapped and cannot address the sensing information of each FBG. Recently, besides increasing the number of FBG sensors and increasing the maximum transmission distance, much attention was focused on wavelength detection of spectrally overlapped FBG sensors.

In IWDM, central Bragg wavelength detection technique is a very important issue to detect each FBG central wavelength even when two or more FBG spectra are partially or fully overlapped [18]. Previous researchers have proposed several central wavelength detection methods, such as tabu-gradient search algorithm [18], filters [19, 20], conventional peak detection (CPD) [21], radial basis function network [22], and ADALINE network [23]. In [19], the sensing accuracy of FBG sensors was improved using a digital low-pass filter. However, the filter affects the measurement accuracy due to noise within the filter. CPD uses a tunable optical filter to detect the central wavelength of each FBG sensor [21]. However, this technique is inappropriate if the spectra of two or more FBGs are overlapped because it cannot address the sensing information of each FBG. All the above central wavelength detection methods have limitations on increasing the number of FBG sensors and detecting the central Bragg wavelength of FBGs when FBG spectra are overlapped.

This paper proposes a novel extreme learning machine (ELM) based central Bragg wavelength detection scheme for spectrally overlapped FBG sensors. An ELM accurately determines the central Bragg wavelengths. Compared to CPD machine learning methods, such as a neural network (NN) or support vector machine (SVM) [24], an ELM has the importance of good generalization and fast learning and requires less human intervention. An ELM is effective in real-time applications because it automatically determines all network parameters [25, 26]. Moreover, we propose IWDM to increase the number of FBG sensors and we employ a Raman amplifier to increase the sensing signal transmission distance and to improve the signal quality.

The rest of this paper is organized as follows. In Section 2, a brief discussion about operational principles with a mathematical expression is presented. Section 3 presents about an ELM. In Section 4, the experimental and simulation results are presented. Finally, we summarize the conclusion part of this paper in Section 5.

2. Operational Principles and Methods

The schematic diagram of applying IWDM and ELM techniques to a FBG sensor system is explained by using three FBG sensors as shown in Figure 1. A broadband light source is emitted from EDFA. The light emitted from the broadband light sources is injected into FBG sensors through a 2×2 coupler (50 : 50) and split into two branches (50 : 50). The one branch of a 50 : 50 coupler comprised a 1×2 coupler (30 : 70). The two FBG sensors (i.e., FBG1 and FBG2) are employed after a 30% and 70% output power ratio of a 1×2 coupler, respectively. FBG3 is employed after a 50% output power ratio of a 50 : 50 coupler. FBG3 is deployed after a 45 km SMF in order to have a gain medium. The back-reflected light from each FBG is propagated through the other arm of a 2×2 coupler and passes into the Raman amplifier. The Raman output power can be pumped to the SMF via a WDM coupler. The Raman amplifier consists of two laser diodes (LDs) with wavelengths of 1420 nm and 1450 nm. The polarization beam combiner (PBC) combines the outputs from the two LDs. The combined outputs from the two laser diodes are inserted into the Raman pump through the WDM coupler and the combined light is fed into a 45 km SMF. The output signal from the Raman amplifier is
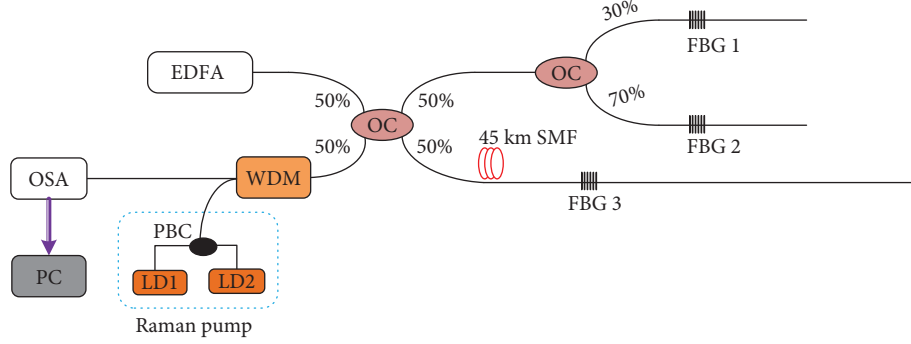
FIGURE 1: The schematic diagram of the proposed system (EDFA: erbium-doped fiber amplifier; OSA: optical spectrum analyzer; OC: optical coupler; FBG: fiber Bragg grating; SMF: single-mode fiber; WDM: wavelength division multiplexing; PBC: polarization beam combiner; LD: laser diode; PC: personal computer).
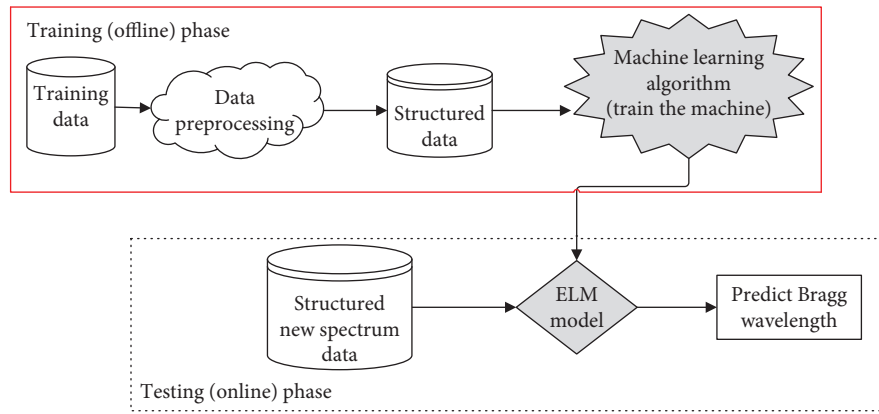
FIGURE 2: The architecture of ELM-based wavelength detection.

fed into the optical spectrum analyzer (OSA) to show the back-reflected wavelengths and to measure the central Bragg wavelengths. Finally, the measured reflected spectra of FBGs from OSA are sent to a personal computer (PC) for additional data processing.

The traditional WDM requires that each FBG sensor should have a unique spectral region, which limits the multiplexing capability of the sensor system [9]. The proposed method allows the reflection spectra of two FBGs which are overlapped when entering into the overlapping region. When a bandwidth of the full width at half maximum (FHWM) is larger than the distance between two FBG central wavelengths, it is difficult to identify each FBG central Bragg wavelength [24]. Hence, in our study, the central wavelength detection of overlapped spectra is converted to a regression problem. We assume that $R(\lambda)$ is the reflected spectra of FBGs from the OSA and λ_{Bi} ($i = 1, 2, 3$) are the central Bragg wavelengths of the ith FBG. The measured spectra from the OSA are expressed as

$$R(\lambda, \lambda_B) = \left(\sum_i^n R_i g_i(\lambda, \lambda_{Bi}) \right) + \text{noise}(\lambda), \qquad (1)$$

where $\lambda_B = [\lambda_{B1}, \lambda_{B2}, \lambda_{B3}]$ are the central Bragg wavelengths of FBGs, $R_i g_i(\lambda, \lambda_{Bi})$ is the peak reflectivity of

the ith FBG, n is the number of FBG sensors, and noise (λ) is a random noise.

If the spectra of FBGs are overlapped, it is very difficult to determine the central Bragg wavelengths (λ_{Bi}) from the spectra $R(\lambda, \lambda_B)$ using CPD methods. Hence, we use ELM techniques to detect (identify) the central Bragg wavelength of each FBG sensor. The proposed ELM is employed to do multiple-input-multiple-output regression as shown in Figure 2. ELM is a supervised learning algorithm which has two different phases, that is, the training phase (offline phase) and testing phase (online phase). During the training phase, a number of training data are provided to train the ELM.

$$\text{Data} = \{(x_1, y_1), \dots, (x_k, y_{k1}), \dots, (x_n, y_n)\}, \qquad (2)$$

where $x_k = R(\lambda) \in R^n$ is the sampling data from the FBG reflection spectra generated using (1), $y_k = \lambda_B \in R^m$ are the corresponding target outputs, n is the number of wavelengths in the spectra, and m is the number of FBG sensors in the system.

During the testing phase, only the new measured FBG reflection spectra from the OSA are fed into the well-trained ELM model. The well-trained ELM model quickly detects (identify) the central Bragg wavelengths of each FBG.

Figure 3: Structure of a single-hidden layer feedforward neural network (SLFN).

3. Extreme Learning Machine (ELM)

This paper proposes an ELM-based central Bragg wavelength detection to address the issue of a nonlinear relationship between FBG and 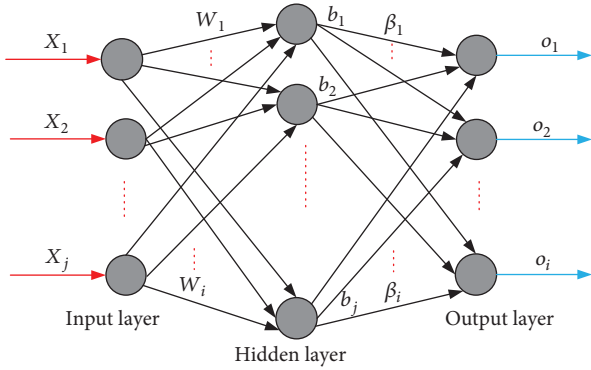strain factors. Scheme [24] proposed an ELM for single-hidden layer feedforward networks (SLFNs). A SLFN structure contains three layers, such as the input layer, hidden layer, and output layer, which are connected by neurons, as shown in Figure 3. This method is limited to feedforward neural networks with a single nonlinear hidden layer, as this type of network is capable of making a random close approximation of any continuous nonlinear mapping [27]. Instead of using traditional gradient-based learning methods which require several iterations, an ELM has its input weights randomly generated and uses simple matrix computations between hidden layers and output layers to determine the output weights. Solving the regularized least squares in ELM is faster than solving the quadratic programming problem in the SVM method [25, 26].

The ELM approach considers the wavelength detection problem as a regression problem. During the training process, the ELM randomly generates input weights w_i and bias values b_i. The prediction can be computed only by determining the activation function and the number of neurons in the hidden layer. Given the training data by (2), the standard SLFN for an arbitrary N different samples (x_j, t_j), where $x_j = [x_1, x_2, \ldots, x_n]^T \in R^n$ is the input wavelength spectra and $t_j = [t_1, t_2, \ldots, t_m]^T \in R^m$ is the target Bragg wavelength of FBGs. Standard SLFNs with activation function $g(x)$ and $\tilde{N}$ hidden neurons are mathematically expressed as follows:

$$\sum_{i=1}^{\tilde{N}} \beta_i g\left(w_i \cdot x_j + b_i\right) = t_j, \quad i = 1, 2, \ldots, N, \tag{3}$$

where $\beta_i = [\beta_1, \beta_2, \ldots, \beta_m]^T$ is the output weights connecting the ith hidden neuron and output neurons, $w_i = [w_1, w_2, \ldots, w_n]^T$ is the randomly chosen input weights connecting the input neurons and the ith hidden neurons, $\tilde{N}$ is hidden neuron number, b_j is the random bias connecting

the input layers and the ith hidden layer, and t_j is the actual outputs of input x_j.

According to [24], (3) can be rewritten into a matrix form as follows:

$$\mathbf{H}\boldsymbol{\beta} = \mathbf{T}, \tag{4}$$

where

$$\mathbf{H} = \begin{bmatrix} g(w_1 \cdot x_1 + b_1) & \cdots & g(w_{\tilde{N}} \cdot x_1 + b_{\tilde{N}}) \\ \vdots & \cdots & \vdots \\ g(w_1 \cdot x_N + b_1) & \cdots & g(w_{\tilde{N}} \cdot x_N + b_{\tilde{N}}) \end{bmatrix} N \times \tilde{N},$$

$$\boldsymbol{\beta} = \begin{bmatrix} \beta_1^T \\ \vdots \\ \beta_{\tilde{N}}^T \end{bmatrix} \tilde{N} \times m,$$

$$\mathbf{T} = \begin{bmatrix} t_1^T \\ \vdots \\ t_{\tilde{N}}^T \end{bmatrix} N \times m,$$

$$\tag{5}$$

where $\mathbf{H}$ is the output matrix of hidden layers, $\boldsymbol{\beta}_i$ is the output weight matrix, and $\mathbf{T}$ is the target output. In backpropagation learning algorithm, a user requires specifying the value of the learning rate and the total error function will not be found. Backpropagation learning algorithm may overtrain and can have local minima [28]. To overcome this problem, scheme [28] proposed the smallest norm least squares solution of $\mathbf{H}\boldsymbol{\beta} = \mathbf{T}$. Thus, the output weight $\boldsymbol{\beta}$ can be calculated by the inner product of the matrix of $\mathbf{H}$ and $\mathbf{T}$ as the following [24].

$$\boldsymbol{\beta} = \mathbf{H}^+\mathbf{T}, \tag{6}$$

where $\boldsymbol{\beta}$ is the output weight matrix, $\mathbf{H}^+$ is the Moore-Penrose pseudoinverse (MPPI) of matrix $\mathbf{H}$ [29], and $\mathbf{T}$ is the target output. Equation (6) provides the best generalization performance with a minimum training error [28]. Finally, once $\boldsymbol{\beta}$ is obtained, the well-trained ELM can be used for regression task. When we obtain newly measured reflected overlap spectra of FBGs from the OSA as a testing sample data z_i, the equivalent outputs of the well-trained ELM can be mathematically calculated as

$$O_i = \sum_{i=1}^{\tilde{N}} \boldsymbol{\beta}_i g(w_i \cdot z_i + b_i), \quad i = 1, 2, \ldots, N, \tag{7}$$

where O_i is the output of the ELM which is the detected (estimated) central Bragg wavelength of each FBG. Therefore, the well-trained ELM can detect or estimate the central wavelengths of the testing sample. Generally, the algorithm of the ELM network is a learning algorithm which is given a training set: $D = \{(x_j, t_j) \mid x_j \in R^n t_j \in R^m j = 1 \ldots N\}$, activation function $g(w, b, x)$, and the number of
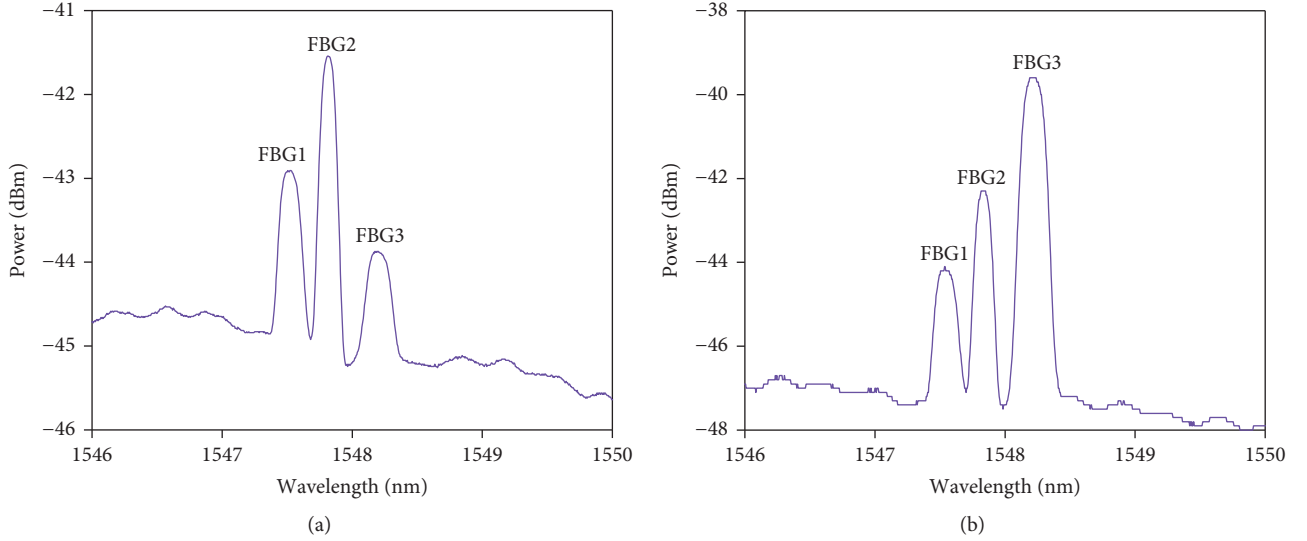
FIGURE 4: The measured spectra of three FBGs (a) before the Raman pump (b) after the Raman pump.

hidden nodes $\tilde{N}$. The ELM-based learning procedure can be summarized as follows:

(1) Determine the number of hidden layer neurons, randomly set bias b_i, and set weights w_i between the input layer and the hidden layer.

(2) Choose distinguishable activation function and then calculate output matrix $\mathbf{H}$ of the hidden layer for all the training samples.

(3) The weights b_i and the output weight $\boldsymbol{\beta}$: $\boldsymbol{\beta} = \mathbf{H}^+\mathbf{T}$ are calculated, where $\mathbf{H}^+$ is the MPPI of the hidden layer output matrix $\mathbf{H}$.

4. Experimental and Simulation Results

Figure 1 shows the experimental setup of the IWDM-FBG sensor system using a Raman amplifier and ELM. A broadband light source emitted from EDFA is injected into three FBG sensors. The measured reflection spectra of FBGs are sampled into 1001 points within a wavelength range from 1545.71 nm to 1550.71 nm. The span width of OSA is set to be 4 nm and the minimum resolution of the OSA is 0.03 nm. The measured reflection spectra of FBGs from the OSA are passed to a PC for further data processing. The central wavelengths of FBG1, FBG2, and FBG3 are 1547.54 nm, 1547.83 nm, and 1548.21 nm, respectively. The 3 dB bandwidths of the FBG1, FBG2, and FBG3 sensors are 0.24 nm, 0.226 nm and 0.24 nm, respectively. The reflectivity as well as bandwidth of the FBG sensors changes under different grating lengths and refractive index changes. We assumed that the reflection spectra of three FBGs are Gaussian shaped given by

$$R(\lambda, \lambda_{\mathrm{B}i}) = I_{\mathrm{peak}} \exp\left[-4\ln 2 * \left(\frac{\lambda - \lambda_{\mathrm{B}i}}{\Delta\lambda_{\mathrm{B}i}}\right)^2\right], \qquad (8)$$

where λ is the wavelength, I_{peak} is the FBG maximum peak reflectivity, $\lambda_{\mathrm{B}i}$ is the peak wavelength of FBGs, and $\Delta\lambda_{\mathrm{B}i}$ is the full width at half maximum. Typically, when the distance between three central Bragg wavelengths is smaller than the bandwidth of the full-width half maxima (FWHM), it is hard to directly distinguish each peak wavelength. The peak reflectivity of each FBG must be different to identify each FBG central Bragg wavelength from the overlapping spectra.

In the FBG sensor system, the maximum signal transmission distance is commonly limited to 25 km due to signal loss in fiber link and Rayleigh scattering. Signal loss and Rayleigh scattering induces optical noise and degrade the transmitted signal quality [11–16]. Therefore, we use a Raman amplifier to increase the transmission distance (long-distance sensing) and to compensate for the signal losses in long-distance transmission. As shown in Figure 1, FBG3 is deployed after 45 km SMF for long-distance signal transmission or for remote sensing up to 45 km. Figure 4(a) shows the measured spectra of three FBGs when the Raman pump is turned off. As shown in the figure, the power of FBG3 wavelength is very small and even disappears when the Raman pump is turned off. Hence, after 45 km transmission, it is very challenging to detect the central Bragg wavelength of FBG3 without employing a Raman amplifier. Therefore, by adding a Raman amplifier to a fiber span (FBG3), signal power loss is decreased and it highly improves the signal-spontaneous beat noise performance. Signal propagating along the fiber will be attenuated, but as it moves toward the fiber end where the Raman pump is located, it will start to experience some gain from the Raman pump wavelength. The higher power in the signal thus increases the signal-to-noise ratio (SNR), which enables longer fiber span, higher capacity and spectral efficiency, and longer distance. On the other hand, FBG1 and FBG2 have not been positioned in long distance compared to FBG3 as shown in Figure 1. Hence, FBG1 and FBG2 can sense signals below 25 km. As shown in Figure 4(a), the measured spectra of FBG1 and FBG2 are
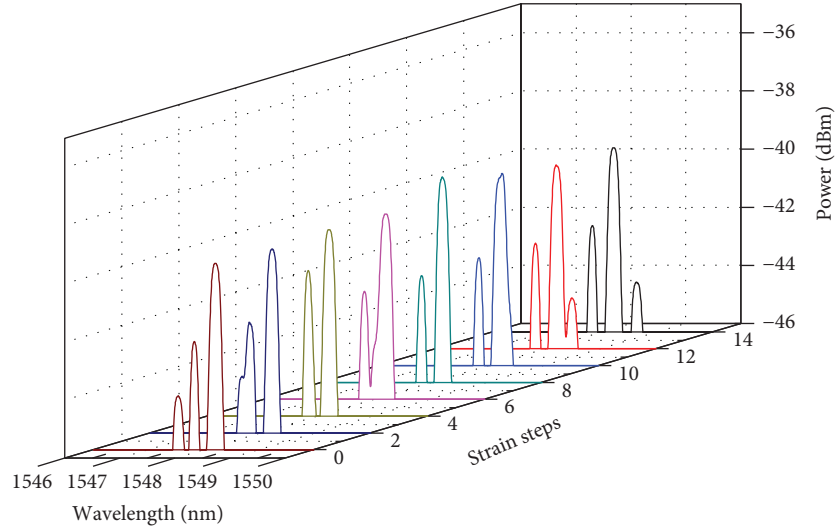
FIGURE 5: The reflected spectra of three FBG sensors using simulation when strain is applied to FBG1 corresponding to strain steps 0, 2, 4, 6, 8, 10, 12, and 14.

visible and can detect the central Bragg wavelength even when the Raman pump is turned off. Because of this, we do not need any Raman amplification in the FBG1 and FBG2 sensors. Figure 4(b) shows the measured spectra when the Raman pump is turned on. As shown in the figure, the sensing signal quality of FBG1 and FBG2 is the same with when the Raman pump is turned off. But, the sensing signal of FBG3 is significantly improved when the Raman pump is turned on because the Raman pump compensates for the signal loss of a long-distance fiber. After 45 km SMF transmission, the gain medium value of FBG3 before and after the Raman amplifier is 4 dB, which is adequate to compensate for the signal losses.

IWDM technique can increase the number of FBG sensors to be multiplexed by keeping the same dynamic range for each FBG sensor [8]. However, as the number of FBG sensors increases, the spectra of two or more FBGs are partially or fully overlapped. Hence, we use ELM to accurately determine the central Bragg wavelengths of each FGB when the spectra of two FBGs are overlapped. We develop a simulation environment using MATLAB to verify ELM-based central Bragg wavelength detection techniques when the spectra of FBGs are overlapped. The simulation runs on a PC, which has Intel Core i7-4790 3.60 GHz CPU and 20.48 GB RAM. The simulation of ELM-based central wavelength detection is conducted with three FBG sensors. Assume that the reflected spectra of three FBGs are Gaussian shaped [30]. The reflected spectra of three FBGs are added with random noise using (1) to simulate in a bad environment. During the simulation, the central Bragg wavelength of FBG1 is shifted from 1547.54 nm to 1548.662 nm by applying a changing strain to FBG1, while the Bragg wavelengths of FBG2 and FBG3 are fixed at 1547.83 nm and 1548.21 nm, respectively. The strain applied to FBG1 is increased by ~75 $\mu\varepsilon$ at each step. If a strain is applied to FBG1, the central Bragg wavelength will shift because the refractive index changes. Hence, the detected wavelength

of FBG1 also shifts. The center Bragg wavelength shift of FBG1 according to the axial strain applied to a fiber grating is described as

$$\Delta\lambda B = \lambda B(1 - Pe)\varepsilon, \tag{9}$$

where $\Delta\lambda B$ is the central Bragg wavelength shift, λB is the central Bragg wavelength, Pe is the elastic-optical constant (Pe $\approx$ 0.22), and ε is the applied strain to FBG1. If we know the central Bragg wavelength shift of FBG1 at each applied strain value, we can calculate the central Bragg wavelength of FBG1 at each applied strain value by using the following equation:

$$\lambda B = \frac{\Delta\lambda B}{(1 - Pe)\varepsilon}. \tag{10}$$

Therefore, we can change the central wavelength of FBG1 at each applied strain value using (1) and then the reflection spectra of FBGs are calculated by (1) using MATLAB simulation. The measurements are repeated for 14 different strain values (steps). Figure 5 shows the reflected spectra of three FBGs when a strain is applied to FBG1 corresponding to strain steps 0, 2, 4, 6, 8, 10, 12, and 14. As shown in the figure, it can be seen that the spectra of three FBGs are distinct at strain step 0, step 12, and step 14. But, the spectra of FBG1 and FBG2 are partially overlapped at strain step 2 and fully overlapped at strain step 4. Similarly, the spectra of FBG1 and FBG3 are partially overlapped at strain step 6 and step 10 and fully overlapped at strain step 8. As shown in Figure 6, the overlapping FBG spectra causes crosstalk and unmeasurable gaps between FBG sensors, which is why it is difficult to determine the exact central (peak) wavelength using the traditional CPD technique (without using ELM techniques).
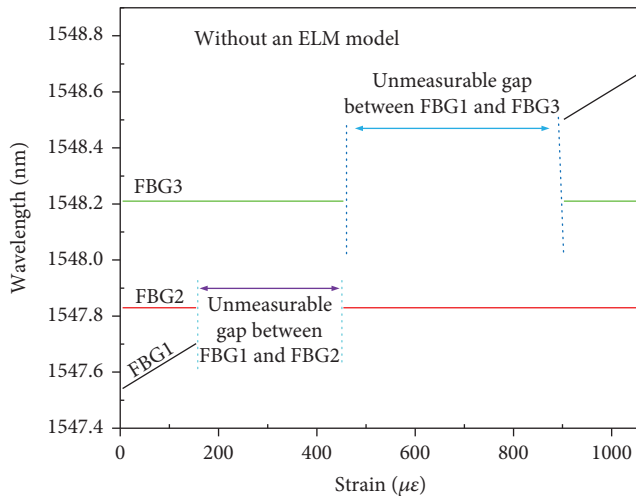
FIGURE 6: Unmeasurable gaps when the spectra of two FBG sensors are overlapped (i.e., without using an ELM model).

Figure 6 shows the unmeasurable gaps of three FBG sensors when the spectra of two FBGs are overlapped. We apply a strain within the range from $0\,\mu\varepsilon$ to $1052\,\mu\varepsilon$ to FBG1, and this causes its central wavelength to shift from $1547.54\,nm$ to $1548.662\,nm$. When the applied strain to FBG1 is between $150\,\mu\varepsilon$ and $450\,\mu\varepsilon$, the spectra of FBG1 and FBG2 are overlapped and we cannot detect the central wavelengths of the two FBG sensors using CPD technique. The range that cannot detect the central wavelength of FBGs is called unmeasurable gaps. When the applied strain to FBG1 is greater than $450\,\mu\varepsilon$, the spectra of FBG1 and FBG2 are separated but the spectra of FBG1 are overlapped with FBG3. Applying a strain to FBG1 within the range of $450\,\mu\varepsilon$–$900\,\mu\varepsilon$ will create unmeasurable gaps for both FBG1 and FBG3. Hence, we cannot detect the central wavelengths of FBG1 and FBG3 using CPD techniques. We can directly detect all the three FBG central Bragg wavelengths using CPD technique only if the applied strain is less than $150\,\mu\varepsilon$ or greater than $900\,\mu\varepsilon$. When the applied strain is between $150\,\mu\varepsilon$ and $900\,\mu\varepsilon$, unmeasurable gaps will be created for at least in the two FBG sensors. Because of this, we have proposed ELM to solve the overlapping or unmeasurable gap problem subsequently. For each applied strain value, the well-trained ELM can accurately detect the central Bragg wavelengths of three FBGs using (8) even when the spectra of FBGs are within the overlapping or unmeasurable gap range.

The proposed ELM techniques is demonstrated and tested by using MATLAB simulation to verify the feasibility of an ELM for wavelength detection mechanisms. In order to train an ELM, the training dataset are generated using (1), which is the reflection spectra of three FBGs by applying a changing strain to FBG1. The measurements are repeated for 14 different strain values (steps), and the reflection spectra of FBGs are calculated by (1) using MATLAB simulation. Figure 5 shows the reflection spectra of three FBGs when we apply different strains to FBG1. The training dataset has inputs and corresponding targets. The inputs are the reflection spectra of three FBGs at each applied strain value to FBG1, and the corresponding targets are the central

wavelength of each FBG at each applied strain value to FBG1. The generated training data can be preprocessed and prepared to be used for training an ELM based on (2). The sample size of training data is 15000. ELM is trained for 30 times with the training datasets using feedforward neural network algorithms. During the training phase, we have adjusted the number of neurons, number of epochs, and the number of hidden layers to get the best generalization performance of the ELM. The best performance of the well-trained ELM is obtained when the number of neurons is 2000 and the number of epochs is 1000. The training and testing accuracy increases when the number of neurons increases. The test dataset is generated from the reflection spectra of three FBGs measured by an OSA using an experimental method. During the experiment, strain is applied to FBG1 to shift the central Bragg wavelength from $1547.54\,nm$ to $1548.662\,nm$, while the central Bragg wavelengths of FBG2 and FBG3 are fixed. To apply a strain to FBG1, FBG1 is mounted on a translation stage (TS). Then, by manually tuning the TS, a strain is applied to FBG1. This manual tuning of the TS in the fiber grating leads to a shift in the central Bragg wavelength of FBG1. When the central Bragg wavelength of FBG1 shifts, an overlap occurs between FBG1 and FBG2 and between FBG1 and FBG3 at a different time. The shift in the central Bragg wavelength of FBG1 is observed and obtained from an OSA. The applied strain to FBG1 at each step is ~$75\,\mu\varepsilon$. The strain (ε) is related to the displacement (ΔL) of the translation stage by $\varepsilon = \Delta L/L$, where L is the total fiber length under strain. After the strain is applied to FBG1, the reflection spectra of three FBGs are measured by using an OSA. The measurements are repeated for 14 different strain values (steps). For each applied strain value, three measurements are carried out within a period of 3 minutes. The sample size of testing data is 2000. Figures 7(a) and 7(b) show the reflection spectra of three FBGs generated by the OSA for some typical applied strain values (steps) to FBG1 corresponding to strain steps 4 and 8, respectively. During the test phase, we have taken new fully overlapped spectra from the OSA, as shown in Figures 7(a) and 7(b), to test the well-trained ELM model. The well-trained ELM model can accurately detect or determine the central Bragg wavelengths of FBG1, FBG2, and FBG3 by (8).

Figures 7(a) and 7(b) show the reflected spectra of three FBGs measured by an OSA by applying a strain to FBG1 corresponding to strain steps 4 and step 8, respectively. As shown in the figure, the two FBG sensor spectra are overlapped, which is why it is difficult to identify the central Bragg wavelength of each FBG using traditional CPD techniques. Therefore, we use ELM techniques to solve this problem. For each applied strain, an ELM achieved to obtain the exact central Bragg wavelengths of FBG1, FBG2, and FBG3 in all independent test runs. Figure 8 shows the simulation output of the detected central Bragg wavelengths of three FBGs using the well-trained ELM model when the spectra of FBG1 and FBG2 are fully overlapped at strain step 4 (see Figure 7(a)). The absolute value of the difference between the predicted central wavelength value and actual central wavelength values is calculated as the detection error, expressed as detection error = |predicted central wavelength
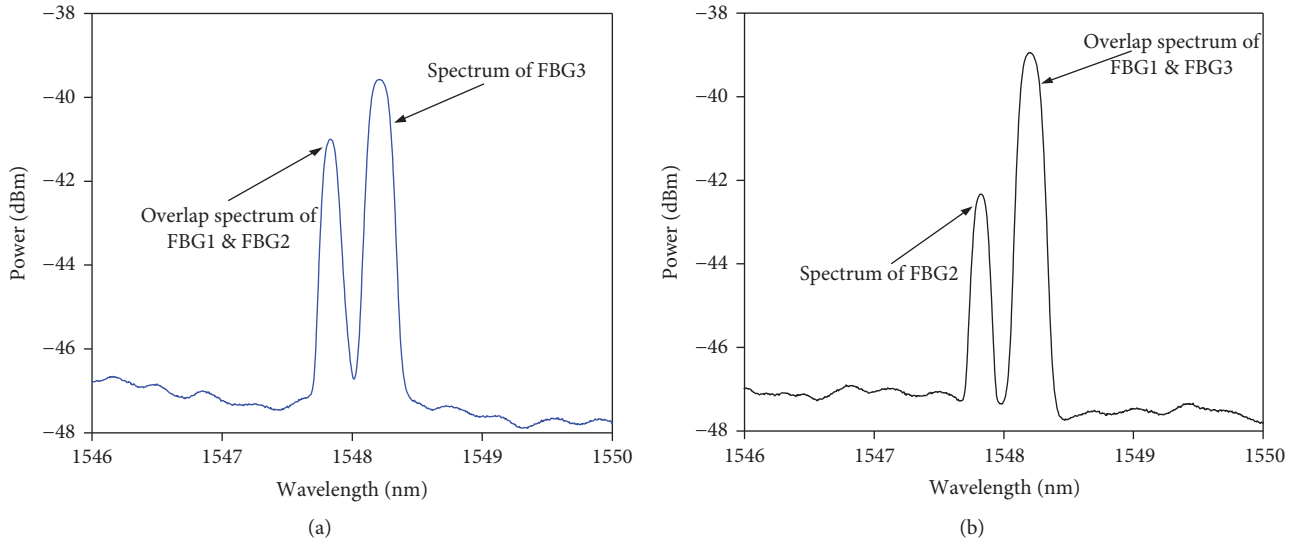
FIGURE 7: The reflected spectra of three FBG sensors from OSA (a) when the spectra of FBG1 and FBG2 are fully overlapped at strain step 4 (b) when the spectra of FBG1 and FBG3 are fully overlapped at strain step 8.
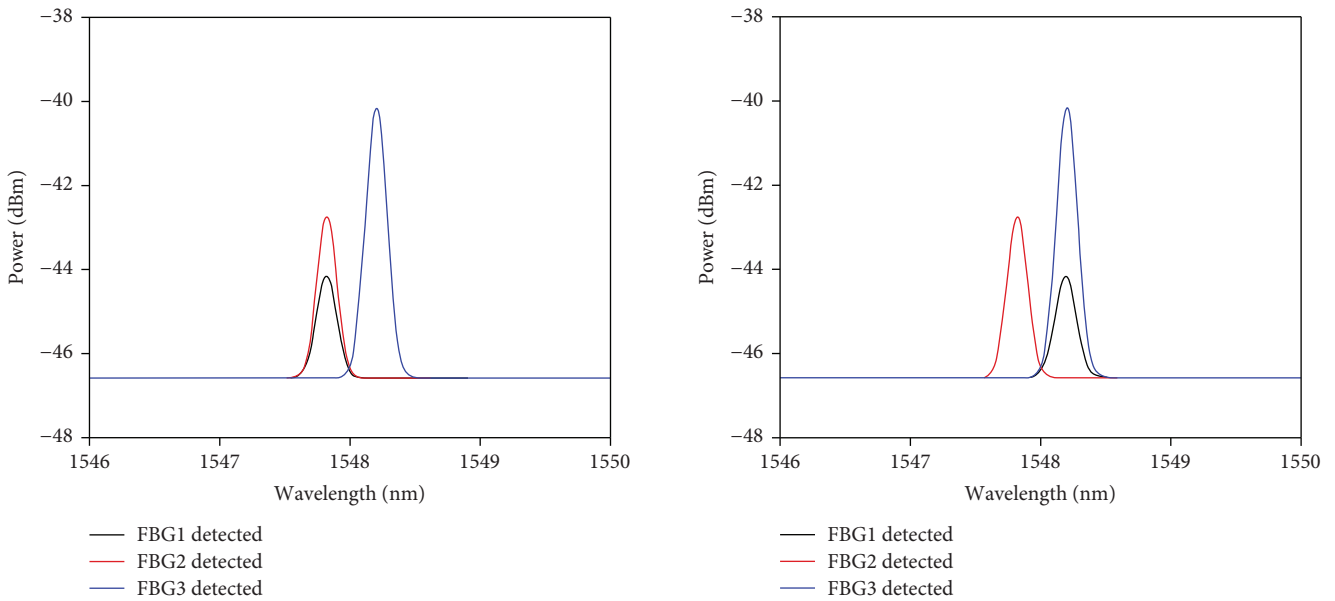
FIGURE 8: Output of the ELM model (the detected Bragg wavelengths of three FBGs when FBG1 and FBG2 are overlapped at strain step 4 using an ELM model).

FIGURE 9: Output of the ELM model (the detected central Bragg wavelengths of three FBGs when FBG1 and FBG3 are overlapped at strain step 8 using an ELM model).

value – actual central wavelength values|. The detection error of the proposed ELM model when FBG1 and FBG2 spectra are overlapped is 0.018, which is a very small error. This indicates that we can accurately identify the central Bragg wavelengths of FBG1 and FBG2 even though the input spectra of the two FBG sensors are fully overlapped. Similarly, Figure 9 shows the simulation output of the detected central Bragg wavelengths of three FBGs using the well-trained ELM when the spectra of FBG1 and FBG3 are fully overlapped at strain step 8 (see Figure 7(b)). The detection error of the proposed method when FBG1 and FBG3 spectra are overlapped is 0.021, which is a very small error. Because the central wavelengths of FBG2 and FBG3 are fixed (constant), we can easily

identify which central wavelength is for FBG1, FBG2, and FBG3 when the well-trained ELM detects (identify) the central wavelengths of three FBGs (see Figures 8 or 9). Only the FBG1 central wavelength varies during wavelength shift or overlap. Therefore, Figures 8 and 9 indicate that the well-trained ELM model can accurately detect the central Bragg wavelengths of FBG1, FBG2, and FBG3 even though the input spectra of the two FBG sensors are fully overlapped.

Figure 10 shows the output of the well-trained ELM model, which is the detected central Bragg wavelengths of three FBGs at each strain value (steps). When the central Bragg wavelengths of two FBGs are partially or fully overlapped (from strain step 2 to step 12), the proposed ELM

FIGURE 10: The detected central Bragg wavelengths of three FBGs at different strain values by using an ELM model.

FIGURE 11: Performance of the proposed ELM model at each applied strain step.

can determine the central Bragg wavelengths of three FBGs even in the overlapping wavelength range. The performance of the ELM model can be described in terms of training time, testing 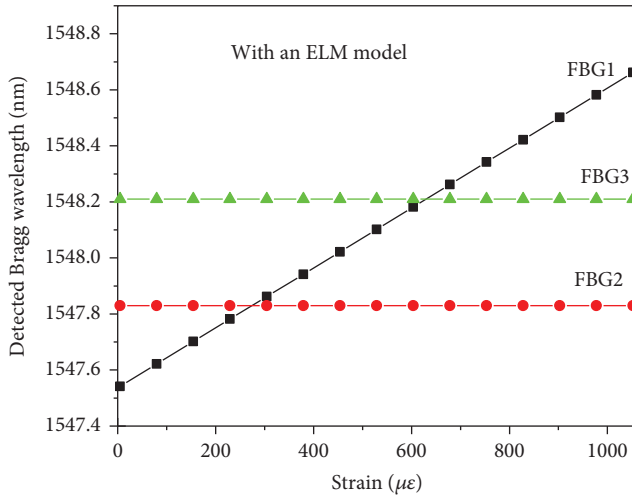time, and root-mean-square error (RMSE) values of the testing result. An ELM has an enormous advantage in training time and learning speed. When the number of hidden neurons is 2000, the training time of the ELM is 12 s and the testing time of the ELM is 0.10 s. Both the training time and testing time increase when the number of hidden neurons increases. Since an ELM model can directly determine the central Bragg wavelengths of FBG sensors, an ELM is much simpler and greatly reduces the training time and testing time than CPD techniques. RMSE can evaluate the central Bragg wavelength detection performance of the well-trained ELM when two or more FBG spectra are partially or fully overlapped. RMSE values can be calculated by the following equation:

$$\text{RMSE} = \sqrt{\frac{\sum_{i=1}^{n}(P_i - A_i)^2}{n}}, \tag{11}$$

where A_i is the actual central Bragg wavelength, P_i is the predicted (detected) central Bragg wavelength, and n is the number of test data. The central Bragg wavelength detection accuracy of the well-trained ELM model in terms of RMSE throughout the operation strain range (from 0 to 1052 $\mu\varepsilon$) is 0.3 pm.

Figure 11 shows the well-trained ELM central Bragg wavelength detection errors (i.e., RMSE) against 14 strain steps. As shown in the figure, the RMS error is very high when the two FBG spectra is fully overlapped (when strain step = 4 and step = 8) which means that the detection accuracy decreases when the two wavelength spectra are overlapped. When the two central Bragg wavelengths fully overlapped (at strain step = 4 and step = 8), an ELM can identify the central Bragg wavelengths of three FBGs. The RMS error in strain step 4 and step 8 is 1.25 pm and 1.28 pm, respectively. Figure 12 shows the RMS errors
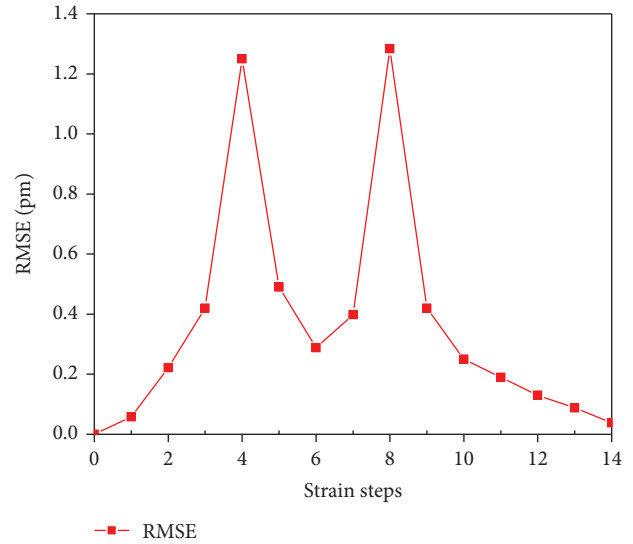
with epochs. The detection performance of an ELM is stable when the number of epoch increases, but it tends to become worse when too few epochs are used. As shown in the figure when the epoch number is 1000, the RMS error becomes around 0.25 pm which is very small. Therefore, experimental and simulation results show, using the well-trained ELM, that the central Bragg wavelengths of FBGs are identified with definite accuracy, even if the reflected spectra of FBGs are fully overlapped. The central Bragg wavelength detection accuracy achieved by an ELM is 0.3 pm, which has better generalization performance than CPD techniques [19–23].

5. Conclusion

This paper introduces an IWDM-FBG sensor system using a Raman amplifier and ELM. FBGs are favorable sensors in different applications and have the advantages of being immune to electromagnetic interference, light weight, flexible, stretchable, small size, highly accurate, longer stability, and capable in measuring ultra-high-speed events. A Raman amplifier is used to increase the sensing signal transmission distance and optimize the quality of the signal. Increasing the Raman pump power increases the transmission distance and the sensing signal quality. The experimental result revealed that a Raman amplifier can compensate for the signal losses and can provide a stable sensing output even beyond a 45 km transmission distance. Moreover, we achieve a remote sensing of strain measurement at a remote location of 45 km. We employed IWDM to increase the number of FBG sensors and to allow FBG spectra to overlap. The proposed ELM can address the problem of the unmeasurable gaps that have been faced in IWDM techniques. ELM is much simpler, greatly reduces the training time and testing time, and improves the detection accuracy than convolutional wavelength detection techniques. The RMSE of the proposed system is 0.3 pm which is possible to accurately

FIGURE 12: Performance of the proposed ELM model on a number of epochs.

detect the central Bragg wavelengths of each FBG even if the spectra of FBGs are fully overlapped.

Data Availability

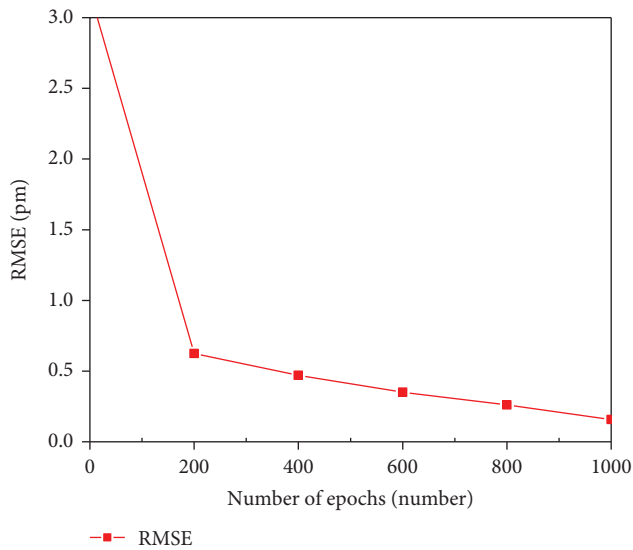The data used to support the findings of this study are available from the first author upon request.

Conflicts of Interest

The authors declare that there is no conflict of interest regarding the publication of this paper.

Acknowledgments

References

[1] R. Kashyap, *Fiber Bragg Gratings*, Academic Press, New York, NY, USA, 2009.

[2] A. D. Kersey, M. A. Davis, H. J. Patrick et al., "Fiber grating sensors," *Journal of Lightwave Technology*, vol. 15, no. 8, pp. 1442–1463, 1997.

[3] J. Cui, Y. Hu, K. Feng, J. Li, and J. Tan, "FBG interrogation method with high resolution and response speed based on a reflective-matched FBG scheme," *Sensors*, vol. 15, no. 7, pp. 16516–16535, 2015.

[4] H. F. Lima, P. F. Antunes, J. D. L. Pinto, and R. N. Nogueira, "Simultaneous measurement of strain and temperature with a single fiber Bragg grating written in a tapered optical fiber," *IEEE Sensors Journal*, vol. 10, no. 2, pp. 269–273, 2010.

[5] C. C. Ma and C. W. Wang, "Transient strain measurements of a suspended cable under impact loadings using fiber Bragg grating sensors," *IEEE Sensors Journal*, vol. 9, no. 12, pp. 1998–2007, 2009.

[6] Z. Zhang, L. Yan, W. Pan et al., "Sensitivity enhancement of strain sensing utilizing a differential pair of fiber Bragg gratings," *Sensors*, vol. 12, no. 4, pp. 3891–3900, 2012.

[7] K. S. Choi, J. Youn, E. You et al., "Improved spectral tag method for FBG sensor multiplexing with equally spaced spectral codes and simulated annealing algorithm," in *2009 IEEE Sensors*, pp. 1256–1259, Christchurch, New Zealand, 2009.

[8] L. Zhang, Y. Liu, J. A. R. Williams, and I. Bennion, "Enhanced FBG strain sensing multiplexing capacity using combination of intensity and wavelength dual-coding technique," *IEEE Photonics Technology Letters*, vol. 11, no. 12, pp. 1638–1640, 1999.

[9] P. C. Peng, J. H. Lin, H. Y. Tseng, and S. Chi, "Intensity and wavelength-division multiplexing FBG sensor system using a tunable multiport fiber ring laser," *IEEE Photonics Technology Letters*, vol. 16, no. 1, pp. 230–232, 2004.

[10] C. H. Yeh, Y. H. Zhuang, N. Tsai, and C. W. Chow, "Capacity and capability enhancements of FBG sensor system by utilizing intensity and WDM detection technique," *Smart Materials and Structures*, vol. 26, no. 3, article 035026, 2017.

[11] H. Y. Fu, H. L. Liu, W. H. Chung, and H. Y. Tam, "A novel fiber Bragg grating sensor configuration for long-distance quasi-distributed measurement," *IEEE Sensors Journal*, vol. 8, no. 9, pp. 1598–1602, 2008.

[12] S. K. Liaw, Y. W. Lee, H. W. Huang, and W. F. Wu, "Multi-wavelength linear-cavity SOA-based laser array design for multiparameter and long-haul sensing," *IEEE Sensors Journal*, vol. 15, no. 6, pp. 3353–3358, 2015.

[13] Y. G. Han, T. V. A. Tran, S. H. Kim, and S. B. Lee, "Multiwavelength Raman-fiber-laser-based long-distance remote sensor for simultaneous measurement of strain and temperature," *Optics Letters*, vol. 30, no. 11, pp. 1282–1284, 2005.

[14] Y. G. Han, T. V. A. Tran, S. H. Kim, and S. B. Lee, "Development of a multiwavelength Raman fiber laser based on phase-shifted fiber Bragg gratings for long-distance remote-sensing applications," *Optics Letters*, vol. 30, no. 10, pp. 1114–1116, 2005.

[15] Y. Nakajima, Y. Shindo, and T. Yoshikawa, "Novel concept as long-distance transmission FBG sensor system using distributed Raman amplifier," in *Proceedings of the 16th International Conference on Optical Fiber Sensor (OFS) Th1-4*, pp. 530–533, Nara, Japan, October 2003.

[16] B. Y. Guo, W. C. Tang, Y. C. Manie, M. A. Bitew, H. K. Lu, and P. C. Peng, "Long-distance sensing fiber sensor system using broadband source and Raman amplifier," in *2017 IEEE International Conference on Consumer Electronics - Taiwan (ICCE-TW)*, pp. 413-414, Taipei, Taiwan, 2017.

[17] P. C. Peng, H. Y. Tseng, and S. Chi, "Long-distance FBG sensor system using a linear-cavity fiber Raman laser scheme," *IEEE Photonics Technology Letters*, vol. 16, no. 2, pp. 575–577, 2004.

[18] X. Xu, J. Chicharo, and J. Xi, "Improving the performance of IWDM FBG sensing system using tabu-gradient search algorithm," in *2006 International Symposium on Intelligent Signal Processing and Communications*, pp. 788–791, Tottori, Japan, 2006.

[19] C. C. Chan, W. Jin, and M. S. Demokan, "Enhancement of measurement accuracy in fiber Bragg grating sensors by using digital signal processing," *Optics & Laser Technology*, vol. 31, no. 4, pp. 299–307, 1999.

[20] C. C. Chan, J. M. Gong, C. Z. Shi et al., "Improving measurement accuracy of fiber Bragg grating sensor using digital

matched filter," *Sensors and Actuators A: Physical*, vol. 104, no. 1, pp. 19–24, 2003.

[21] E. Udd, "Fiber optic smart structures," *Proceedings of the IEEE*, vol. 84, no. 6, pp. 884–894, 1996.

[22] A. S. Paterno, J. C. C. Silva, M. S. Milczewski, L. V. R. Arruda, and H. J. Kalinowski, "Radial-basis function network for the approximation of FBG sensor spectra with distorted peaks," *Measurement Science and Technology*, vol. 17, no. 5, pp. 1039–1045, 2006.

[23] C. C. Chan, C. Z. Shi, W. Jin, and D. N. Wang, "Improving the wavelength detection accuracy of FBG sensors using an ADA-LINE network," *IEEE Photonics Technology Letters*, vol. 15, no. 8, pp. 1126–1128, 2003.

[24] G. B. Huang, Q. Y. Zhu, and C. K. Siew, "Extreme learning machine: theory and applications," *Neurocomputing*, vol. 70, no. 1–3, pp. 489–501, 2006.

[25] X. Chen, Z. Y. Dong, K. Meng, Y. Xu, K. P. Wong, and H. W. Ngan, "Electricity price forecasting with extreme learning machine and bootstrapping," *IEEE Transactions on Power Systems*, vol. 27, no. 4, pp. 2055–2062, 2012.

[26] R. Rajesh and J. S. Prakash, "Extreme learning machines-a review and state-of-the-art," *International Journal of Wisdom Based Computing*, vol. 1, no. 1, pp. 35–39, 2011.

[27] F. Han, D. S. Huang, Z. H. Zhu, and T. H. Rong, "The forecast of the postoperative survival time of patients suffered from non-small cell lung cancer based on PCA and extreme learning machine," *International Journal of Neural Systems*, vol. 16, no. 1, pp. 39–46, 2006.

[28] M. Pal, "Extreme-learning-machine-based land cover classification," *International Journal of Remote Sensing*, vol. 30, no. 14, pp. 3835–3841, 2009.

[29] D. Serre, *Matrices: Theory and Applications*, Springer-Verlag, New York, NY, USA, 2010.

[30] C. Z. Shi, N. Zeng, C. C. Chan, Y. B. Liao, W. Jin, and L. Zhang, "Improving the performance of FBG sensors in a WDM network using a simulated annealing technique," *IEEE Photonics Technology Letters*, vol. 16, no. 1, pp. 227–229, 2004.

Research Article

Textile Concentric Ring Electrodes: Influence of Position and Electrode Size on Cardiac Activity Monitoring

Gema Prats-Boluda [iD],[1] **Yiyao Ye-Lin,**[1] **Francisco Pradas-Novella,**[1]
Eduardo Garcia-Breijo [iD],[2] **and Javier Garcia-Casado**[1]

[1]*Centro de Investigación e Innovación en Bioingeniería, Universitat Politècnica de València, Valencia 46022, Spain*
[2]*Instituto Interuniversitario de Investigación de Reconocimiento Molecular y Desarrollo Tecnológico (IDM), Universitat Politècnica de València, Valencia 46022, Spain*

Correspondence should be addressed to Gema Prats-Boluda; gprats@ci2b.upv.es

Continuous ECG monitoring can play an important role in the rapid detection of pathological signatures and arrhythmias. Current systems use electrodes with limitations in wearable long-term applications and spatial selectivity. In this work, two sizes of textile concentric ring electrodes (TCRE42 and TCRE50) were developed and tested for monitoring cardiac activity. The low-cost devices were found to be easy to implement and to potentially have the advantages of textile electrodes for being lightweight, stretchable, adjustable, washable, and long-lasting. Both TCREs yielded similar signal detectability of different ECG waves. The optimal P wave recording area (OPA) for detecting signals was on the upper right chest. Although the absolute signal amplitude of TCRE records was smaller than that of lead II, normalized amplitude in the OPA is similar for T wave and higher for P wave. The TCREs also allowed better analysis of P wave morphology and were able to detect more right and left atrial depolarization waves. TCRE48 showed slightly better detectability, normalized amplitude, and spatial selectivity than TCRE50 within the OPA. The authors consider the TCRE suitable for use in ubiquitous mobile health care systems, especially for atrial activity monitoring and diagnosis.

1. Introduction

Measurement of electrophysiological signals is crucial for monitoring bodily states and facilitating clinical diagnoses. Of all the vital signs, the electrocardiogram (ECG) is the most important, since it is the primary diagnostic tool for cardiovascular diseases, the first cause of death in developed countries. The analysis of the different cardiac waves in the ECG signals is of major importance; the P wave represents the depolarization wave that spreads from the sinoatrial node throughout the atria; the QRS complex represents ventricular depolarization, while the T wave represents ventricular repolarization. The ECG provides information on heart rate and electrical conduction in the heart, which enables the diagnosis of a wide range of cardiac pathologies, such as sinus tachycardia or bradycardia, bundle branch block, AV blocks, or atrial/ventricular fibrillation, which can be dangerous or even cause sudden death [1].

Diagnosis is usually by analyzing 12-lead ECG short-term records in clinics with benchtop equipment and wet disc electrodes. The most commonly used electrode for ECG monitoring is a gel-type silver/silver chloride (Ag/AgCl) electrode. However, as some pathologies require extended monitoring during the patient's normal activities, interest in mobile and long-term monitoring has grown for diagnosis, screening, risk assessment, prevention, and rehabilitation [2]. Wet electrodes are limited in their long-term use because they can irritate the skin. A conductive gel is a significant drawback as it can dry out over time, increasing contact impedance and losing signal quality [3]. Dry ECG electrodes have emerged as an alternative for long-term ECG monitoring. They do not need gel but operate through natural body

moisture and perspiration [4]. The simplest dry electrode is a metal disc in direct contact with the skin, but its use is limited due to its stiffness and the fact that it can cause skin irritation. Dielectric materials between the electrode conductor and skin make it possible to use noncontact dry electrodes based on capacitive coupling. These are similar to dry contact electrodes and are also sensitive to motion artifacts but show better behavior in terms of less skin irritation [5]. One of the newest electrodes is made of conductive textile, with the advantage of being lightweight, flexible, stretchable, adjustable, washable, and long-lasting and does not cause skin irritation [6]. These electrodes are now becoming more popular because they are easy to use and cause minimal discomfort to the wearer. A number of proposals to embed these electrodes in normal clothing have produced promising results [7–9].

However, the standard 12-lead ECG also has limitations in diagnosing pathologies related to regions of anomalous local electrical activity, such as ventricular ischemia, atrial hypertrophies, or atrial flutter, requiring invasive electrophysiology, which involves significant risks for the patient and lengthens the diagnosis time [10]. This is due to the poor spatial resolution of conventional disc and rectangular electrodes, which are affected by the blurring effects of the different conductivities in the conductor. Spatial resolution is associated with the ability to differentiate the activity of dipole sources in different areas. Other configurations of electrode layouts and shapes are needed for better spatial resolution. To deal with this issue, modified electrode designs based on concentric ring electrodes (CREs) have been applied to several bioelectric signal recording and analysis, such as electrocardiographic (ECG) [11–15], electroenterographic (EEnG) [16], and electrohysterographic (EHG) signals [17]. The concentric ring design is a physical approximation to the Laplacian filter, which is the second spatial derivative of the measured potentials and essentially assigns more weight to changes in bioelectric dipoles under measurement points, to enable better differentiation between concurrent, closely spaced dipole sources [14]. CREs have been shown to be more effective at increasing spatial resolution than merely increasing the number of electrodes in an array, as in conventional body surface potential mapping [18]. This enhanced spatial resolution is of great interest in studying atrial activity, since there are fewer cardiac cells involved in atrial than ventricular activities. In fact, atrial fibrillation is the typical example of an arrhythmia in which a standard 12-lead ECG is insufficient to guide clinical management [19].

So far, CREs have been built on rigid substrates [12, 20, 21] or flexible substrates such as polyester films [14, 16, 17] or polydimethylsiloxane (PDMS) elastomer [22]. We recently produced a CRE on a textile that can potentially benefit from the combination of long-term recording with high spatial resolution [23]. This initial experience showed it was possible to pick up cardiac activity with textile CRE (TCRE) and that silver inks performed better than PEDOT:PSS inks. The aim of the present work was to use this sensor to further explore the possibility of detecting and studying the different cardiac waves, with the emphasis on the *P* wave, and to analyze the influence of the size and position of the TCRE on the results.

2. Materials and Methods

2.1. Textile Concentric Ring Electrodes (TCREs). Two sets of TCREs of two different sizes were designed, developed, and tested in the present work. The TCREs were integrated in elastic strips for adaptation to the body surface. Each strip had two TCREs of the same size with centers separated by 12 cm. The TCREs were made up of an inner disc and an outer ring (Table 1). The TCRE's external diameter was similar to the distance between the surface of the chest and the heart (between 3.5 and 5.0 cm) [19]. Compared to other CRE developed onto plastic substrates and used for picking up ECG signals in wet recordings (using electrolytic gel) [14], TCRE recording areas were increased in order to reduce the electrode impedance considering the signals recorded by TCRE under dry conditions (without electrolytic gel) [23].

Applying conductive patterns to textiles can be achieved by microcontact embedded electrodes, inkjet printing, and screen printing [24]. Conductive patterns of thin stainless steel, copper, or other metal wires are embroidered onto textile fabrics [25]. Screen printing is a popular method due to its relatively low cost and became possible by the development of polymer-based inks, which allow low curing temperatures compatible with textile substrates [26]. TCRE electrodes were thus produced using multilayer thick film serigraphic technology [23]. The screen for the conductors was a 230-mesh polyester material (PET 1500 90/230-48, Sefar, Thal, Switzerland), and the screen for the dielectric layer was a 175-mesh polyester material (PET 1500 68/175-64 PW, Sefar). An UV film Dirasol 132 (Fujifilm, Tokyo, Japan) was used to transfer the stencil to the screen mesh. The final screen thickness was $10 \, \mu$m for the conductor screen and $15 \, \mu$m for the dielectric screen. The patterns were transferred to the screen by a UV light source. As for the materials: Mediatex TT ACQ $120 \, \mu$m textile (Junkers & Muellers GmbH, Mönchengladbach, Germany) was chosen for the substrate, C2131014D3 silver ink 59.75% (Gwent Group, Pontypool, UK) as the conductive ink, and D2081009D6 polymer dielectric (Gwent Group, Pontypool, UK) as the dielectric ink. The electrical connection of the CREs with the measuring system was a snap fastener in each terminal of the electrodes, as shown in Figure 1. Further physical and electrical characterization, that is, final layer thickness, magnitude and phase of the impedance, and skin-electrode impedance, can be found at [23].

2.2. Recording Protocol. Nine recording sessions were performed on healthy male subjects aged between 21 and 43 years of age, with body mass indexes between 19.6 and $27.47 \, \text{kg/m}^2$, thoracic contour between 81 and 119 cm, and an internipple distance ranging from 19 to 29 cm. The study was approved by the Universitat Politècnica de València's Ethics Committee, and the Declaration of Helsinki was adhered to. The volunteers were previously informed of the nature of the study, briefed on the recording protocol, and signed a consent form.

The recording sessions were carried out with the subjects lying on a stretcher. They were asked to relax and

TABLE 1: Dimensions and distances of the TCREs.

Parameter	TCRE50	TCRE42
Inner disc diameter (mm)	16	16
Ring internal diameter (mm)	36	28
Ring external diameter (mm)	50	42
Distance (between discs' centers) (mm)	120	120

remain motionless to avoid fluctuations on the body surface electrocardiographic recordings due to changes in the heart position. Firstly, to reduce skin-contact impedance, the skin under the electrodes was previously exfoliated (Nuprep, Weaver and Company, USA) and shaved if necessary. Two disposable Ag/AgCl electrodes (Kendall 100 Series Foam Electrodes, Medtronic, USA) were positioned on the left ankle and right wrist to obtain a standard lead II ECG signal, with a ground electrode on the right ankle.

To study the influence of the electrode position and to determine the best area to capture atrial activity, signals were recorded on a grid (see Figure 2) by two TCREs on elastic strips on the right of the subject vertically aligned with the right nipple, 8.5 cm above and 4.5 cm below it, respectively (see Figure 2). We adjusted the elastic strip so as to apply a light pressure to the dry TCRE and yield good electrode to skin contact. Subsequently, four bipolar concentric ECG signals (BC-ECG) (one per TCRE) and the standard lead II ECG signal were simultaneously recorded for 2 minutes with the subject at rest. The bands were then horizontally moved in steps of 2 cm, until the entire area between the nipples was recorded, with between 6 and 8 recordings per subject per strip. The same scan was repeated twice more with downward vertical displacements of 2 cm each (see Figure 2). This process yielded between 72 and 96 recording points per subject and was performed for both electrode sizes (TCRE50 and TCRE42).

Commercial instrumentation amplifiers (Grass Technologies P511, AstroNova Inc., West Warwick, RI, USA) performed the signal conditioning of the four simultaneous BC-ECGs and lead II ECG signals. Signals were band-pass (0.1–100 Hz) and power line (50 Hz) filtered and then acquired at a 1000 Hz sampling frequency (USB NI-6229 BNC National Instrument acquisition card, Austin, TX).

2.3. ECG Analysis. The signals were digitally high-pass filtered with a linear-phase FIR filter with a cutoff frequency of 0.3 Hz to diminish baseline drift, and notch filter at 100 Hz to attenuate power line harmonics. The first step in the ECG analysis was to obtain the ECG average beat for each recording position and subject; the Pan-Tompkins algorithm [27] was used for beat detection.

The electrocardiographic waves (P, QRS, T) were identified in the average beats. An experienced cardiologist determined if each wave was distinguishable (detected) or not. To determine the optimal recording area for picking up atrial activity with TCRE, the chest was divided into four areas, as shown in Figure 2. These were the upper and lower right areas (from the chest midline to the right above and below the nipple, resp.) and the upper and lower left areas (from the chest midline to the left above and below the nipple, resp.). Subsequently, the recording site percentage detectability (RSPD) for the different ECG waves (P, Q, R, S, and T) in each area and the global recording area was worked out for each subject. The area that provided the highest mean P wave detectability was selected as the optimal P wave recording area (OPA).

Absolute and normalized peak-to-peak amplitude of cardiac waves at each recording site was also computed to further characterize and compare BC-ECGs. Median and interquartile values of absolute amplitude over all the recorded positions on each subject were calculated to obtain information on signal intensity and variability. The normalized amplitude is relevant since it provides information on the ability to analyze the morphology of each wave for clinical diagnosis. Parameters related to normalized amplitudes (or amplitude ratios) of the cardiac waves have been extensively used in the literature for different aims, ranging from biometric recognition systems to developing new diagnostic algorithms [28, 29]. In the present work, peak-to-peak amplitudes of P and T waves were normalized to those of the whole average beat, that is, QRS in almost all cases. The median and maximum normalized amplitudes of the P and T waves were calculated over all the recorded positions on each subject. The absolute and normalized amplitudes of cardiac waves from lead II were also computed to compare the performance of TCREs with traditional cardiac sensing methods.

The capacity of TCRE to provide additional information on atrial activity to that from common disc electrodes was studied, especially the possibility of discriminating the electrical activity associated with the right and left atria in BC-ECG and lead II signals.

In order to assess the spatial selectivity of TCRE50 and TCRE42 in picking up cardiac activity, we used the SS_w parameter. This was worked out for each cardiac wave as the average of the ratios of the absolute amplitude at one recording site and the four neighboring sites, as follows [12]:

$$SS_w(x_0, y_0) = \frac{((PP(x_0, y_0)/PP(x_{-1}, y_0)) + (PP(x_0, y_0)/PP(x_{+1}, y_0)) + (PP(x_0, y_0)/PP(x_0, y_{-1})) + (PP(x_0, y_0)/PP(x_0, y_{+1})))}{4},$$
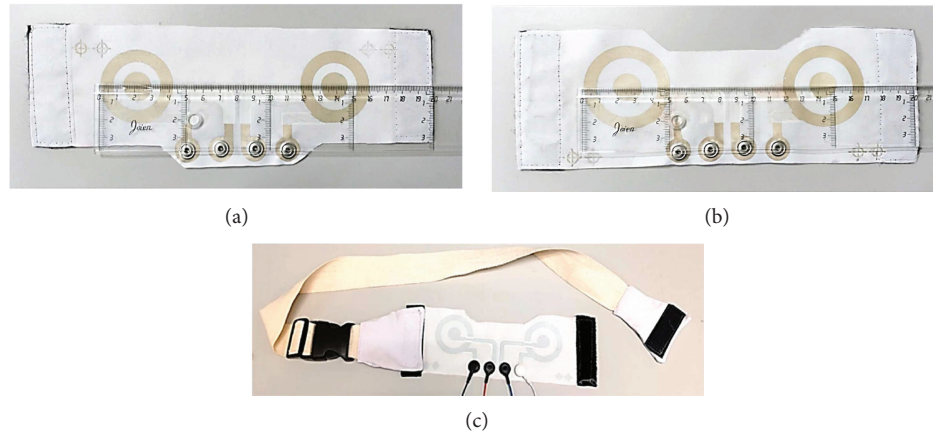
$$(1)$$

(a)

(b)

(c)

FIGURE 1: View of the elastic strip with silver concentric ring electrode TCRE42 (a) and silver concentric ring electrode TCRE50 (b). TCREs incorporated in an adjustable belt (c).
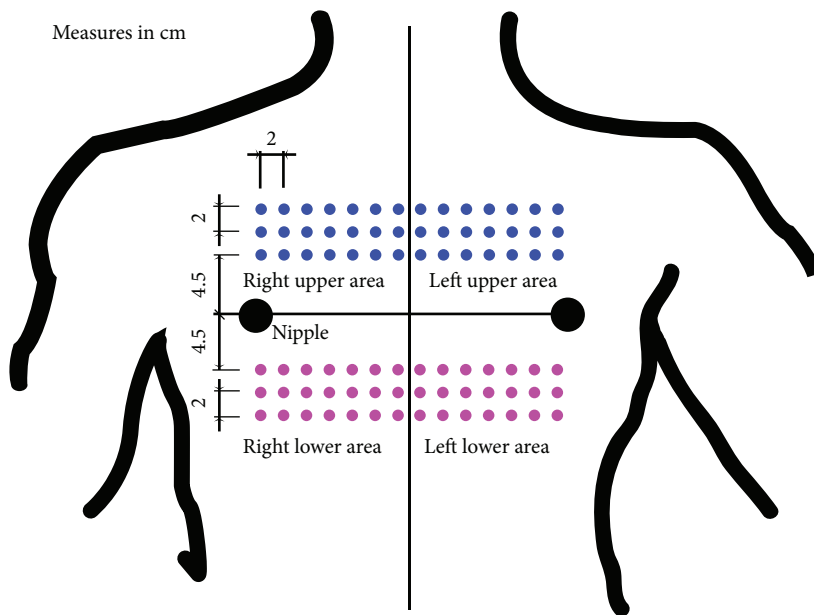
FIGURE 2: Grid of recording sites over the chest. Each dot represents a TCRE recording site. Horizontal and vertical distances between recording sites are indicated.

where PP is the peak-to-peak amplitude of the P, QRS, or T waves in the average beat at location (x_0, y_0) and its four adjacent average beats. Since the computation of this parameter requires records above and below the (x_0, y_0), it was only computed for the central recording rows above and below the nipples (see Figure 2). This could not be computed for the first and last recording sites (columns) in this row. The average spatial selectivity was then computed for each subject.

3. Results and Discussion

Figure 3 shows the average beats of body surface BC-ECG mapping obtained from one subject using TCRE50, depicted with the same amplitude scale for all the recording positions. It can be seen that the maximum amplitude of the BC-ECG signals is usually found in the third and fourth rows, in the

FIGURE 3: Body surface BC-ECG mapping obtained from subject number 1 using the TCRE50 electrode with the average beat at the different recording positions depicted in the same scale.

recording positions from the median line to the left nipple (see Figure 3). The BC-ECG signals recorded at the first 5 points on the right in the sixth row tended to have a v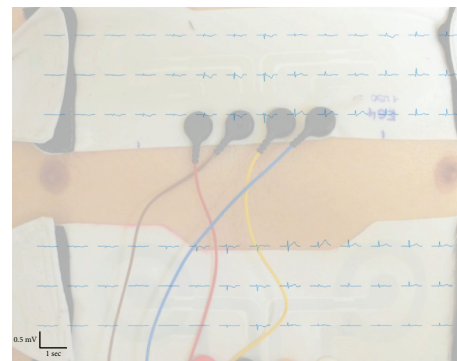ery low amplitude. This could be expected since the TCRE was quite far from the signal source and is in agreement with the findings of other authors [12]. The bipolar TCRE far-field rejection is proportional to the inverse fourth power of the distance between the signal wavefront and the electrode center [30]. Thus, the greater the distance from the ventricle, the greater the attenuation of the QRS complex. Nonetheless, the current signal conditioning and acquisition systems provide good quality signals for a wide range of input signal amplitudes such as those used in this study.

In fact, as clinical devices usually represent ECGs on a grid with adjustable vertical (and horizontal) scales for different traces, the use of autoscaled plots clinically makes sense. Figure 4 shows signals of Figure 3 with autoscaled vertical scales. It can be observed that, despite the low amplitude of the raw signal, both the QRS complex and T wave can be easily identified in all the recording positions. This outperforms other systems that failed to detect ECG fiducial points (P, QRS, T waves) using PEDOT:PSS rectangular-shaped electrodes dip-coated in polyester substrate [31]. The authors claim that this failure was due to the lower quantity of PEDOT:PSS absorbed by polyester and the high contact impedance between the skin and the polyester electrode [31]. In the present study, the screen-printed silver electrode probably provided better skin-electrode impedance, thus obtaining a high-quality ECG signal. The P wave was only detected in the BC-ECG signal recorded at 38 of the 84 recording positions on this subject (shaded green in Figure 4), which are distributed in an area far removed from the ventricle. It seems that in these areas, the proportional attenuation of ventricular activity is higher than that of the atrial activity, resulting in an area of enhanced P wave sensing, probably due to the relatively longer distance from the different cardiac signal sources.

The different ECG waves' RSPD of all the BC-ECG recording sites and each of the 4 predefined areas is shown in Table 2. It can be seen that TCRE50 and TCRE42 provided similar RSPD values for the different ECG waves. The QRS complex associated with ventricle depolarization can easily be recorded in any position, with 100% detectability for both TCREs. The T wave associated with the repolarization of the ventricle was present in the ECG signal acquired at almost all the recording points and was identifiable in 97% of the cases. However, the P wave associated with atrial depolarization was only detected in 41% of the recording sites by both TCREs. The detectability values of cardiac waves obtained in the present work are slightly higher than those obtained by other authors using CREs [14]. This may be related to various factors; firstly, the textile TCRE inherently provided better skin-electrode contact than CREs implemented on Melinex ST506 (plastic substrate) [14]. Furthermore, the adjustable belt used in the present study may also exert additional pressure and so may further improve skin-electrode contact, while the larger contact area of the TCRE poles than the CRE [14] may also contribute to better contact.
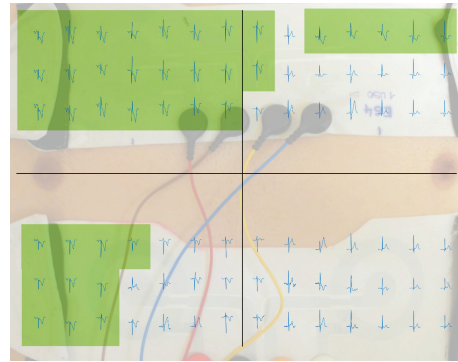

FIGURE 4: Body surface BC-ECG mapping obtained from subject number 1 using the TCRE50 electrode with the average beat at the different recording positions depicted in autoscale. The green areas are the recording sites in which the P wave was detected in this subject.

TABLE 2: Mean and standard deviation of the recording site percentage detectability of the ECG waves of all the recording sites (global) and for the 4 predefined areas when using both TCREs.

Electrode	Wave	Global (%)	Right upper area (%)	Left upper area (%)	Right lower area (%)	Left lower area (%)
	P	41 ± 11	86 ± 14	17 ± 12	52 ± 29	2 ± 5
TCRE50	QRS	100 ± 0	100 ± 0	100 ± 0	100 ± 0	100 ± 0
	T	97 ± 3	100 ± 0	99 ± 2	92 ± 11	98 ± 4
	P	41 ± 12	88 ± 8	22 ± 10	41 ± 29	6 ± 13
TCRE42	QRS	100 ± 0	100 ± 0	100 ± 0	100 ± 0	100 ± 0
	T	96 ± 3	98 ± 3	98 ± 4	95 ± 6	96 ± 6

No significant differences were found for the QRS complex and T wave detectability between the ECG wave RSPD in the 4 predefined areas. However, P wave detection varied widely in different areas. The RSPD results show a generalization of what was observed in Figure 3. Detectability on the left side was poor, almost null for the lower area and slightly better in the upper area. In the right lower area, the P wave was detected in about 50% of the sites, with better performance in the right upper area (86% and 88% for TCRE50 and TCRE42, resp.). This area was thus defined as the optimal P wave recording area (OPA) for further analysis. These results agree with a previous study that found BC-ECG recorded at CMV1 had a superior performance at picking up atrial activity when comparing the signal detectability at four predetermined positions: CMV1 (position comparable to V1), CMV2, CMV4R, and CMV5 [14].

Table 3 shows the absolute and normalized amplitude statistics of the different ECG waves for both BC-ECG and lead II records. In general, the BC-ECG signal amplitude exhibited high variability, not only in the same position among the different subjects but also among the different recording points in the same subject (as can be seen in Figure 3). This latter can be seen in the interquartile range

TABLE 3: Mean and standard deviation of the absolute signal amplitude statistics (median and interquartile range) and normalized amplitude statistics (median and maximum value) obtained using TCREs and lead II* (P_{OPA} refers to the P wave characteristics detected in the optimal P wave recording area).

Electrode	Wave	Absolute amplitude		Normalized amplitude	
		Median (μV)	Interquartile range (μV)	Median	Maximum
TCRE50	P	11.2 ± 2.9	14.7 ± 8.8	0.09 ± 0.03	0.29 ± 0.13
	P_{OPA}	11.5 ± 4.9	10.2 ± 6.2	0.14 ± 0.05	0.26 ± 0.11
	QRS	158.2 ± 38.8	296.3 ± 193.5	—	—
	T	38.7 ± 11.0	75.4 ± 47.4	0.28 ± 0.06	0.76 ± 0.14
TCRE42	P	8.1 ± 2.1	9.9 ± 5.8	0.09 ± 0.03	0.32 ± 0.19
	P_{OPA}	8.8 ± 3.3	7.9 ± 3.1	0.16 ± 0.07	0.32 ± 0.19
	QRS	118.2 ± 32.6	190.3 ± 87.9	—	—
	T	30.6 ± 8.3	59.9 ± 37.1	0.30 ± 0.07	0.89 ± 0.22
Lead II	P	116.0 ± 29.2	—	0.12 ± 0.09	—
	QRS	1182.9 ± 467.1	—	—	—
	T	316.3 ± 139.2	—	0.28 ± 0.14	—

*The constant location of lead II electrodes means some statistics have no practical meaning; these are indicated with dashes to avoid misinterpretation. Similarly, a double dash is used for the normalized QRS amplitude statistic, which is always 1.

value of the amplitude, which was of the same order of magnitude or even greater than the median value. One cause of the high variability in the BC-ECG signal amplitude can be differences in the pressure exerted by the elastic strip used to assure good electrode-skin contact [32]. In future studies, we intend to carry out measures to control this factor. This has been explored in other works in the literature either with direct measures [33] or through the use of inflatable vests/cuffs in which the electrodes are embedded, allowing the precise control of the pressure exerted [25]. Nevertheless, the signal amplitude acquired using both TCREs was typically much smaller than that of lead II for all the ECG waves. This was to be expected, since the distance between the outer ring and the central disc was much shorter than the distance across the body between the lead II electrodes. This result agrees with other authors who simultaneously recorded a standard 12-lead ECG signal and BC-ECG signals using CRE [15, 18, 12]. TCRE50 recorded a higher median signal amplitude than TCRE42, confirming that signal amplitude is dependent on interpole distance. The median amplitude of different ECG waves obtained from the TCREs was similar to that obtained by other authors that used CRE with outer diameters ranging from 21.6 to 45.6 mm [15]. As expected, the P wave amplitude acquired using both TCREs was very low (median value ~ 11 μV), which can be a challenge for the signal conditioning system. In the optimal recording area, the median value of P wave amplitude was slightly higher, with a lower interquartile range than that obtained from all the tested recording points.

As for the normalized P and T wave amplitudes computed from all the recording positions, TCREs generally provide similar values to those of standard lead II, while the maximum normalized BC-ECG amplitudes are at least twice as large as those of lead II. This suggests that this ratio, and thus the "contrast" with which the cardiac waves can be

observed, is highly dependent on the TCRE recording position. In the P wave optimal recording area (P_{OPA}), the median normalized amplitude value was almost double that of all the recording sites and slightly higher than that of lead II. This agrees with other authors who compared the normalized amplitude of BC-ECG signals acquired by CRE and standard 12-lead ECG recording and obtained the highest normalized amplitude at position V1 [14]. Wang et al. also found that signals obtained by CRE maintain good contrast for identifying P waves associated with atrial activity, the normalized P wave amplitude being 13% for lead I and 18% for the BC-ECG signal acquired using CRE at V1 [22]. Regarding the influence of electrode size, TCRE42 provided higher median and maximum normalized amplitude for both the P and T wave than TCRE50, which suggests that it is easier to identify and assess the morphology of these cardiac waves with the smaller electrode.

Regarding the possibility of discriminating the electrical activity associated with the right and left atria in BC-ECG and lead II signals, the associated P1 and P2 cardiac waves were identified in all the subjects by both TCRE50 and TCRE42, although they were observed in only 6 of the 9 subjects in standard lead II (see Figure 5). This suggests that both TCREs offered superior performance than standard lead II in the identification of local activity, which could be of great importance in the diagnosis of pathologies such as atrial hypertrophies or atrial flutter [10].

The average spatial selectivity computed from individual subjects ranged from 0.75 to 3.07, which was of the same order of magnitude as that obtained by Besio and Chen [12]. The mean and standard deviation of the average spatial selectivity for each TCRE size and cardiac wave are shown in Table 4. Similar spatial selectivity values were obtained for different ECG waves. In general, TCRE42 offers better spatial selectivity than TCRE50, regardless of the ECG wave. This
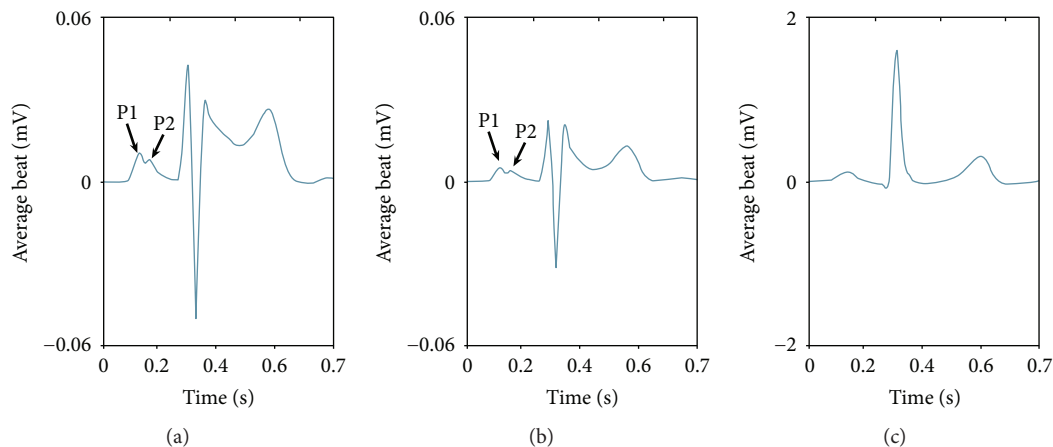
FIGURE 5: Average beats obtained from subject number 2. (a) Using TCRE50 in the OPA; (b) using TCRE42 in the OPA; (c) lead II.

TABLE 4: Mean and standard deviation of TCREs' average spatial selectivity for the different ECG waves.

	TCRE50	TCRE42
P	1.39 ± 0.27	1.74 ± 0.53
QRS	1.49 ± 0.32	1.84 ± 0.38
T	1.68 ± 0.47	1.91 ± 0.74

was as expected, since the bigger the electrode, the wider the recording area, thus the more the mutual information between adjacent recording points and the less the signal amplitude variability between them.

The results obtained suggested that the TCRE is suitable for high spatial resolution ECG long-term recordings in a comfortable manner. However, the study is not exempt from limitations; firstly, relatively few subjects were involved, which means the results should be further corroborated by a larger database. A study should also be carried out on TCRE biocompatibility, long-term wearability, reusability after cleaning, sensitivity to perspiration, motion artifact immunity, and cytotoxicity so as to adapt TCREs for mobile health-care applications [34].

Other limitation of the present study is that it has been performed exclusively in male volunteers. Results derived from the study could be different in the case of women. Gender-dependent differences in breast tissue and in electrical substrate of the human heart could provoke different results [35, 36]. Indeed, slight differences were found between healthy males and females in the limb-lead amplitudes (P, Q, R, S, and T). QRS and P-R duration was significantly shorter in women, and amplitudes (R, S, and T) in precordial leads were significantly smaller [37]. The BMI of the subjects could also affect the measurements [38], as well as the age [39, 40]. In the present study, ECG recordings were carried out in men volunteers with normal BMI and in a fairly narrow age range (young adults). In future works, we would deal to overcome this limitation (gender, BMI, and ECG) analyzing how ECG signals recorded with CRE are influenced by these issues and checking if the optimal area for P wave recording is modified.

4. Conclusions

This paper describes two new textile concentric ring electrodes (TCRE42 and TCRE50) and the results of tests on their ability to sense cardiac activity as compared to standard lead II. The proposed TCREs are easy to implement, can be produced at little cost, and potentially have the advantages of textile electrodes in terms of lightness, flexibility, adjustability, washability, and long life.

Similar signal detectability was obtained by both TCREs for different ECG waves. Based on P wave detectability in BC-ECG recordings, the optimal P wave recording area (OPA) was found to be on the right upper chest. Although the absolute signal amplitude of BC-ECG was smaller than that of lead II, BC-ECG presented a similar normalized T wave amplitude and even higher P wave amplitude in the OPA, allowing better analysis of its morphology. The right and left atrial depolarization waves (P1 and P2) could also be observed in more subjects in the TCRE recordings than in the standard lead II ECG signals. The smaller electrode (TCRE42) yielded slightly better detectability results, normalized amplitude, and spatial selectivity than the TCRE50 in the OPA.

The authors consider that the proposed TCRE could be used in the near future in ubiquitous mobile health care systems, especially for atrial activity monitoring and diagnosis.

Data Availability

The data used to support the findings of this study are available on request from the corresponding author.

Conflicts of Interest

The authors declare that there is no conflict of interest regarding the publication of this paper.

Acknowledgments

References

[1] J. Malmivuo and R. Plonsey, "The basis of ECG diagnosis," in *Bioelectromagnetism: Principles and Applications of Bioelectric and Biomagnetic Fields*, pp. 320–335, Oxford University Press, 1995.

[2] A. Cömert, M. Honkala, and J. Hyttinen, "Effect of pressure and padding on motion artifact of textile electrodes," *Biomedical Engineering Online*, vol. 12, no. 1, p. 26, 2013.

[3] A. Searle and L. Kirkup, "A direct comparison of wet, dry and insulating bioelectric recording electrodes," *Physiological Measurement*, vol. 21, no. 2, pp. 271–283, 2000.

[4] J. G. Webster and J. W. Clark, *Medical Instrumentation : Application and Design*, John Wiley & Sons, 2010.

[5] E. Nemati, M. Deen, and T. Mondal, "A wireless wearable ECG sensor for long-term applications," *IEEE Communications Magazine*, vol. 50, no. 1, pp. 36–43, 2012.

[6] W. Zeng, L. Shu, Q. Li, S. Chen, F. Wang, and X.-M. Tao, "Fiber-based wearable electronics: a review of materials, fabrication, devices, and applications," *Advanced Materials*, vol. 26, no. 31, pp. 5310–5336, 2014.

[7] R. Paradiso, G. Loriga, and N. Taccini, "A wearable health care system based on knitted integrated sensors," *IEEE Transactions on Information Technology in Biomedicine*, vol. 9, no. 3, pp. 337–344, 2005.

[8] M. Catrysse, R. Puers, C. Hertleer, L. Van Langenhove, H. van Egmond, and D. Matthys, "Towards the integration of textile sensors in a wireless monitoring suit," *Sensors and Actuators A: Physical*, vol. 114, no. 2-3, pp. 302–311, 2004.

[9] A. Vehkaoja, J. Verho, A. Cömert, M. Honkala, and J. Lekkala, *Wearable System for EKG Monitoring - Evaluation of Night-Time Performance*, Springer, Berlin, Heidelberg, 2012.

[10] Y. Wang, P. S. Cuculich, J. Zhang et al., "Noninvasive electroanatomic mapping of human ventricular arrhythmias with electrocardiographic imaging," *Science Translational Medicine*, vol. 3, no. 98, p. 98ra84, 2011.

[11] O. Makeyev and W. Besio, "Improving the accuracy of Laplacian estimation with novel variable inter-ring distances concentric ring electrodes," *Sensors*, vol. 16, no. 6, p. 858, 2016.

[12] W. Besio and T. Chen, "Tripolar Laplacian electrocardiogram and moment of activation isochronal mapping," *Physiological Measurement*, vol. 28, no. 5, pp. 515–529, 2007.

[13] B. He and R. J. Cohen, "Body surface Laplacian ECG mapping," *IEEE Transactions on Biomedical Engineering*, vol. 39, no. 11, pp. 1179–1191, 1992.

[14] G. Prats-Boluda, Y. Ye-Lin, J. M. Bueno-Barrachina, R. Rodriguez De Sanabria, and J. Garcia-Casado, "Towards the clinical use of concentric electrodes in ECG recordings: influence of ring dimensions and electrode position," *Measurement Science and Technology*, vol. 27, no. 2, article 025705, 2016.

[15] Y. Ye-Lin, J. M. Bueno-Barrachina, G. Prats-boluda, R. Rodriguez de Sanabria, and J. Garcia-Casado, "Wireless sensor node for non-invasive high precision electrocardiographic signal acquisition based on a multi-ring electrode," *Measurement*, vol. 97, pp. 195–202, 2017.

[16] V. Zena-Giménez, J. Garcia-Casado, Y. Ye-Lin, E. Garcia-Breijo, and G. Prats-Boluda, "A flexible multiring concentric electrode for non-invasive identification of intestinal slow waves," *Sensors*, vol. 18, no. 2, p. 396, 2018.

[17] Y. Ye-Lin, J. Alberola-Rubio, G. Prats-boluda, A. Perales, D. Desantes, and J. Garcia-Casado, "Feasibility and analysis of bipolar concentric recording of electrohysterogram with flexible active electrode," *Annals of Biomedical Engineering*, vol. 43, no. 4, pp. 968–976, 2015.

[18] M. Rodrigo, A. M. Climent, A. Liberos et al., "Minimal configuration of body surface potential mapping for discrimination of left versus right dominant frequencies during atrial fibrillation," *Pacing and Clinical Electrophysiology*, vol. 40, no. 8, pp. 940–946, 2017.

[19] S. Mittal, C. Movsowitz, and J. S. Steinberg, "Ambulatory external electrocardiographic monitoring," *Journal of the American College of Cardiology*, vol. 58, no. 17, pp. 1741–1749, 2011.

[20] C. C. Lu and P. P. Tarjan, "An ultra-high common-mode rejection ratio (CMRR) AC instrumentation amplifier for Laplacian electrocardiographic measurement," *Biomedical Instrumentation & Technology*, vol. 33, no. 1, pp. 76–83, 1999.

[21] G. Prats-Boluda, J. Garcia-Casado, J. L. Martinez-de-Juan, and Y. Ye-Lin, "Active concentric ring electrode for non-invasive detection of intestinal myoelectric signals," *Medical Engineering & Physics*, vol. 33, no. 4, pp. 446–455, 2011.

[22] K. Wang, U. Parekh, T. Pailla, H. Garudadri, V. Gilja, and T. N. Ng, "Stretchable dry electrodes with concentric ring geometry for enhancing spatial resolution in electrophysiology," *Advanced HealthCare Materials*, vol. 6, no. 19, 2017.

[23] J. Lidón-Roger, G. Prats-Boluda, Y. Ye-Lin, J. Garcia-Casado, and E. Garcia-Breijo, "Textile concentric ring electrodes for ECG recording based on screen-printing technology," *Sensors*, vol. 18, no. 1, p. 300, 2018.

[24] M. P. Aleksandrova, G. H. Dobrikov, and G. D. Kolev, "Electrical characterization of PEDOT:PSS based flexible organic optoelectronic devices," *International Journal on "Technical and Physical Problems of Engineering"*, vol. 8, no. 26, pp. 71–76, 2016.

[25] B. Taji, S. Shirmohammadi, V. Groza, and I. Batkin, "Impact of skin–electrode interface on electrocardiogram measurements using conductive textile electrodes," *IEEE Transactions on Instrumentation and Measurement*, vol. 63, no. 6, pp. 1412–1422, 2014.

[26] E. Garcia-Breijo, G. Prats-Boluda, J. V. Lidon-Roger, Y. Ye-Lin, and J. Garcia-Casado, "A comparative analysis of printing techniques by using an active concentric ring electrode for bioelectrical recording," *MicroElectronics International*, vol. 32, no. 2, pp. 103–107, 2015.

[27] J. Pan and W. J. Tompkins, "A real-time QRS detection algorithm," *IEEE Transactions on Biomedical Engineering*, vol. BME-32, no. 3, pp. 230–236, 1985.

[28] S. Sovilj, A. Van Oosterom, G. Rajsman, and R. Magjarevic, "ECG-based prediction of atrial fibrillation development following coronary artery bypass grafting," *Physiological Measurement*, vol. 31, no. 5, pp. 663–677, 2010.

[29] A. Fratini, M. Sansone, P. Bifulco, and M. Cesarelli, "Individual identification via electrocardiogram analysis," *Biomedical Engineering Online*, vol. 14, no. 1, p. 78, 2015.

[30] C. C. Lu and P. P. Tarjan, "Pasteless, active, concentric ring sensors for directly obtained Laplacian cardiac electrograms,"

Journal of Medical and Biological Engineering, vol. 22, pp. 199–203, 2002.

[31] A. Ankhili, X. Tao, C. Cochrane, D. Coulon, and V. Koncar, "Washable and reliable textile electrodes embedded into underwear fabric for electrocardiography (ECG) monitoring," *Materials*, vol. 11, no. 2, p. 256, 2018.

[32] B. Taji, A. D. C. Chan, and S. Shirmohammadi, "Effect of pressure on skin-electrode impedance in wearable biomedical measurement devices," *IEEE Transactions on Instrumentation and Measurement*, pp. 1–13, 2018.

[33] N. Meziane, S. Yang, M. Shokoueinejad, J. G. Webster, M. Attari, and H. Eren, "Simultaneous comparison of 1 gel with 4 dry electrode types for electrocardiography," *Physiological Measurement*, vol. 36, no. 3, pp. 513–529, 2015.

[34] H.-C. Jung, J.-H. Moon, D.-H. Baek et al., "CNT/PDMS composite flexible dry electrodesfor long-term ECG monitoring," *IEEE Transactions on Biomedical Engineering*, vol. 59, no. 5, pp. 1472–1479, 2012.

[35] G. Salama and G. C. L. Bett, "Sex differences in the mechanisms underlying long QT syndrome," *American Journal of Physiology-Heart and Circulatory Physiology*, vol. 307, no. 5, pp. H640–H648, 2014.

[36] A. J. Moss, "Gender differences in ECG parameters and their clinical implications," *Annals of Noninvasive Electrocardiology*, vol. 15, no. 1, pp. 1-2, 2010.

[37] E. Simonson, H. Blackburn, T. C. Puchner, P. Eisenberg, F. Ribeiro, and M. Meja, "Sex differences in the electrocardiogram," *Circulation*, vol. 22, no. 4, pp. 598–601, 1960.

[38] S. Kurisu, H. Ikenaga, N. Watanabe et al., "Electrocardiographic characteristics in the underweight and obese in accordance with the World Health Organization classification," *IJC Metabolic & Endocrine*, vol. 9, pp. 61–65, 2015.

[39] J. Vicente, L. Johannesen, L. Galeotti, and D. G. Strauss, "Mechanisms of sex and age differences in ventricular repolarization in humans," *American Heart Journal*, vol. 168, no. 5, pp. 749–756.e3, 2014.

[40] J. Xue and R. M. Farrell, "How can computerized interpretation algorithms adapt to gender/age differences in ECG measurements?," *Journal of Electrocardiology*, vol. 47, no. 6, pp. 849–855, 2014.